UNIVERSITEIT GENT

FACULTEIT WETENSCHAPPEN

MODELING QUASI-FREE NEUTRINO-NUCLEUS REACTIONS FOR ACCELERATOR-BASED EXPERIMENTS

CHRISTOPHE PRAET

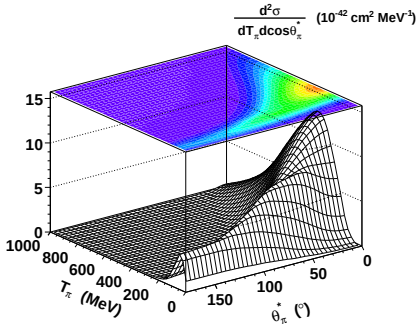

Promotor: Prof. dr. Jan Ryckebusch
Co-promotor: Prof. dr. Natalie Jachowicz

Proefschrift ingediend tot het behalen van de academische graad van
Doctor in de wetenschappen: fysica

Universiteit Gent
Faculteit Wetenschappen
Vakgroep Subatomaire en Stralingsfysica
Academiejaar 2008-2009

Understanding is a three-edged sword.

Kosh Naranek

Vooraf

Het einde van een doctoraat heeft vaak iets frustrerends. Op het moment dat je een goed overzicht hebt van de materie in jouw vakgebied en meer en meer ideeën concrete vormen beginnen aan te nemen, word je ertoe verplicht te rapporteren over de periode die daaraan voorafgaat. Achteraf bekeken ziet er dat niet altijd even fraai uit: je hebt je door de literatuur geworsteld, een welbepaald fysisch proces onder de loep genomen, een computercode ontwikkeld en gedebugd (*zucht*), en enkele eerste resultaten geboekt. Een doctoraatsthesis raakt dus nooit echt "af": altijd had je wel wat meer willen doen. Dat is tenminste hoe ik op dit moment tegen mijn thesis aankijk.

Gelukkig zijn er mensen die voor een iet of wat "vliegende start" hebben gezorgd: Natalie en Jan, bedankt om me op weg te helpen in het onderzoeksleven. Jullie ervaring heeft steeds voor de nodige focus gezorgd in de loop van mijn doctoraat. Wie denkt dat doctoreren een eenzame activiteit is, heeft het -toch voor ongeveer 90%- goed mis. Bij de oude garde, onder wie ik met veel respect Tim en Pascal reken, kon ik steeds terecht met mijn eerste vragen over "de Glauber" en fysica in het algemeen. Om me niet helemaal klein te voelen, kon ik jullie gelukkig af en toe nog eens goed "afdrogen" bij het woensdagmiddagvoetbal. Bart en Annelies, oud-collega's, jullie roepen alleen maar fijne herinneringen bij me op. Klaas en Wim, bureaugenoten van weleer, schrijfmakkers, sommige verhalen zal ik werkelijk nooit vergeten. Thank you, Olga, for the nice collaboration during your stay in Ghent. The many discussions we had on pion production have come to form an invaluable contribution to this thesis. Die unieke groepssfeer zou ongetwijfeld niet dezelfde zijn geweest zonder Pieter, mijn favoriete thesisstudent wiens klare kijk op al wat met fysica te maken heeft de rollen meer dan eens omkeerde, Lesley, waar vind ik in de toekomst nog zo'n concentratie BSG fans?, en Simon, die schijnbaar moeiteloos verbanden legt tussen fysica en economie. Voor alle gezellige koffiepauzes op het INW en UZ-lunches (Nancy! chocola!): merci Brecht, Matthias, Diederik, Arne en de collega's van het eerste verdiep.

Een mens leeft natuurlijk niet van fysica alleen. Vandaar dat het belangrijk is zich omringd te weten door vrienden en familie: dank jullie wel voor de nodige afleiding

tussendoor en om het belang van mijn onderzoek (“werk”) nu en dan wat te helpen relativeren. Merci, mama en papa, om mij te laten studeren tot ik er genoeg van had. Dankzij jullie ben ik bij dit doctoraat aanbeland. Dankzij dit doctoraat heb ik jou leren kennen, lieve Tamara, met jou kon het zowiezo al niet meer stuk...

Contents

1 Introduction

At present, the Standard Model (SM) of elementary particle physics is generally recognized as mankind's most successful attempt to devise a *theory of everything*. In its current form, the SM provides a unified, gauge-theoretical description of strong interactions, called quantum chromodynamics (QCD), and the theory of electroweak interactions, as developed by Glashow, Weinberg and Salam [1, 2]. For their work towards a unification of the electromagnetic and weak forces, the latter received the Nobel Prize in Physics, in 1979. Applying the ideas of spontaneous symmetry breaking to the electroweak gauge symmetry [3, 4] explains why one observes the electromagnetic and weak forces as two different entities in nature. Indeed, the weak vector bosons acquire mass through the Higgs mechanism, thus limiting the range of the weak force. In 2008, the theorists Nambu, Kobayashi and Maskawa were awarded the Nobel Prize in Physics for their contributions to the understanding of spontaneous symmetry breaking in subatomic physics.

Neutrinos in and beyond the Standard Model

In spite of its enormous success in describing the available experimental data with high accuracy, the SM is not deemed to be the last step in unification. The fact that the SM fails to provide predictions for many parameters, including quark masses and electroweak coupling constants, is often seen as a serious shortcoming of the theory. Moreover, the discovery of neutrino oscillations enforces an extension of the SM,

which predicted the neutrino masses to be zero. Any theory that goes beyond the SM should incorporate (or, preferably, predict) a set of additional parameters to relate the neutrino flavour eigenstates to the neutrino mass eigenstates. On the other hand, the SM predicts the existence of the Higgs boson, which has not been discovered yet. At this very moment, searches are taking place at the Tevatron facility in Fermilab, using the same accelerator that led to the discovery of the top quark. Expectations are also running high for the brand new Large Hadron Collider (LHC) at CERN. There are many indications for a SM Higgs particle with a mass between 100 and 200 GeV [5, 6], with the most recent combined analysis of Tevatron CDF and D0 data putting a lower limit of 170 GeV at the 95% confidence level [7]. Therefore, most experts agree that the *god particle* has a more than good chance of being discovered at LHC, which has a discovery potential of up to 1 TeV. If the Higgs boson remains undetected, however, then some other symmetry-breaking scheme must be at work. As a matter of fact, there exist many alternatives to the Higgs mechanism for electroweak symmetry breaking (e.g. technicolor models). Either way, physicists have high hopes that observations made at these facilities will lead to new insights about the SM and, more importantly, about the road to further unification schemes in the form of supersymmetric and grand-unified theories.

The establishment of a non-vanishing neutrino mass in neutrino-oscillation experiments is without any doubt one of the major recent achievements in particle physics. It shows that the picture of neutrinos in the SM is in need of a drastic review. Before the discovery of neutrino oscillations, neutrinos had been observed as purely lefthanded weakly interacting particles. As such, they remained massless, because the then known particle content did not require the introduction of a righthanded singlet state ν_R. In order to explain flavor oscillations, however, it is clear that the weak eigenstates ν_e, ν_μ and ν_τ must be seen as quantum-mechanical superpositions of the mass eigenstates ν_1, ν_2 and ν_3, which evolve in time. Just like in the quark sector, with the Cabibbo-Kobayashi-Maskawa matrix, there is a mass-mixing matrix that relates the flavor and mass eigenstates of neutrinos in terms of three mixing angles and a CP-violating phase. In addition to these parameters, neutrino-oscillation experiments are also sensitive to the mass differences $\Delta m^2_{ij} = m^2_i - m^2_j$ between any two mass eigenstates.

The exciting results of the first oscillation experiments, together with the possibility of discovering new beyond-the-SM physics, have triggered many studies related to the physics of massive neutrinos. Ongoing and planned research activities try to find an answer to the following central questions:

- What are the values of the mixing angles θ_{12}, θ_{13} and θ_{23}?
- What are the values (and signs) of Δm^2_{12} and Δm^2_{23}?
- What is the absolute neutrino mass scale?

- Is the neutrino a Dirac or Majorana particle?
- Is there CP violation for neutrinos?

To address these issues, the efforts are not restricted to oscillation experiments, whose main goal is a precise determination of the mixing parameters and the mass hierarchy. A considerable amount of work is also directed towards direct neutrino-mass searches, using the kinematics of nuclear β decay to determine m_{ν_e} [8]. If the neutrino is a Majorana particle, meaning that it cannot be distinguished from its own antiparticle, it is possible to observe neutrinoless double beta decay [9]. Next to addressing a fundamental question about neutrinos, a half-life measurement of this process is sensitive to the effective Majorana mass $\langle m_{\nu_e} \rangle = |\sum_i U_{ei}^2 m_i|$, with U_{ei} the mixing matrix elements. Furthermore, bounds on neutrino masses are studied in the context of cosmological models [10]. Current data indicate an upper limit $\sum m_\nu < 0.7 - 2.2$ eV for the three generations of neutrinos [5]. Another important line of research deals with the role played by massive neutrinos in the observed matter-antimatter asymmetry in the universe. Scenarios considering the generation of a lepton asymmetry, by decaying heavy Majorana neutrinos, which can be converted into a baryon asymmetry at the energy scale of the electroweak phase transition ($\sim$ 200 GeV) are actively investigated [11, 12]. Many more topics related to massive neutrinos can be found in Ref. [5], where an extensive overview of neutrino experiments in nuclear and particle physics, astrophysics and cosmology is presented.

Neutrinos as probes of weak physics

Besides sharpening our knowledge of particle physics, the ongoing and planned neutrino experiments offer great opportunities for the hadronic- and nuclear-physics community. Neutrinos are peculiar, in the sense that they only interact with matter through weak interactions. In doing so, they violate parity in a maximal way, giving rise to the pure V−A structure of weak lepton and quark currents. Hence, neutrinos present themselves as unique probes for exploring the axial sector in weak interactions.

Of course, one can not just cleanly scatter neutrinos from single quarks. Quarks are confined in nucleons, which are bound inside the nuclei that compose the target material in neutrino detectors. Given that neutrino events are very rare, these detectors often take the shape of kiloton-sized tanks filled with mineral oil, or, of meters long steel plates. A specific kind of oscillation experiments, called long-baseline experiments, study the oscillations of accelerator ν_μ neutrinos by observing their interactions at a *near* detector, close to the neutrino source, and a *far* detector, separated by a distance L. Some examples are summarized in Table 1.1. The MiniBooNE experiment is listed separately, because its main goal is to check the anomalous LSND result, which hints at $\overline{\nu}_\mu \to \overline{\nu}_e$ oscillations at the $\Delta m^2 \sim 1\,\text{eV}^2$ scale. So far, MiniBooNE has not observed

Table 1.1: Long-baseline accelerator experiments, organized by name, baseline length L, mean energy of the neutrino beam $\langle E_\nu \rangle$ and years of running. More details can be found on the websites.

Name	*url*	$L\,(km)$	$\langle E_\nu \rangle\,(GeV)$	*Year*
K2K	http://neutrino.kek.jp/	250	1.3	1999-2004
MINOS	http://www-numi.fnal.gov/Minos/	735	~ 4	2005-...
T2K	http://jnusrv01.kek.jp/public/t2k/	295	0.65	2009-...
NOνA	http://www-nova.fnal.gov/	810	~ 2	2014-...
MiniBooNE	http://www-boone.fnal.gov/	0.5	0.8	2002-...

oscillations at such a mass scale [13], indicating that the introduction of a fourth, sterile neutrino state may not be necessary after all [6]. Contrary to reactor-based experiments, where neutrino energies are of the few-MeV order, it is important to note that all accelerator experiments in Table 1.1 involve few-GeV neutrinos. Indeed, a necessary condition to observe oscillations is given by $L/E_\nu \gtrsim 1/\Delta m^2$. Hence, for a typical baseline length of $\sim$ 100 km, one needs $\sim$ 1 GeV muon neutrinos to enhance the sensitivity to oscillations at the atmospheric mass scale, $\Delta m^2_{atm} \sim$ few $\times\, 10^{-3}$eV^2. As a consequence, a good understanding of neutrino-nucleus interactions in the few-GeV energy range forms an essential ingredient in the analysis of long-baseline neutrino experiments. This holds even more true for the next-generation Superbeams [14], which are higher-intensity versions of the presently-running neutrino beams. Superbeams used in the T2K and NOνA experiments will greatly improve the statistics, to the extent that statistical uncertainties become negligible compared to systematic ones. Next to the important issues of understanding the neutrino flux and detector efficiency, a major source of systematic errors is the neutrino-interaction model. Indeed, in their Monte-Carlo simulations, neutrino experiments rely on these models to distinguish between different types of events and to reconstruct the neutrino energy. Thus, in order to extract the physical information, a realistic description of all relevant processes forms an essential input in experimental analyses.

In return, millions of neutrino events will be gathered in the next coming years, providing an excellent testing ground for various models dealing with weak hadronic and nuclear physics. More specifically, the Minerνa [15] and SciBooNE [16] experiments focus on cross-section physics. Whereas the former will cover a broad range of energies, up to tens of GeV, its proposal makes special mention of studying nuclear effects in weak interactions at medium neutrino energies. The SciBooNE experiment has been using MiniBooNE's Booster beamline to study neutrino- and antineutrino-carbon interactions at 1-GeV neutrino energies. Results of their analysis are expected soon.

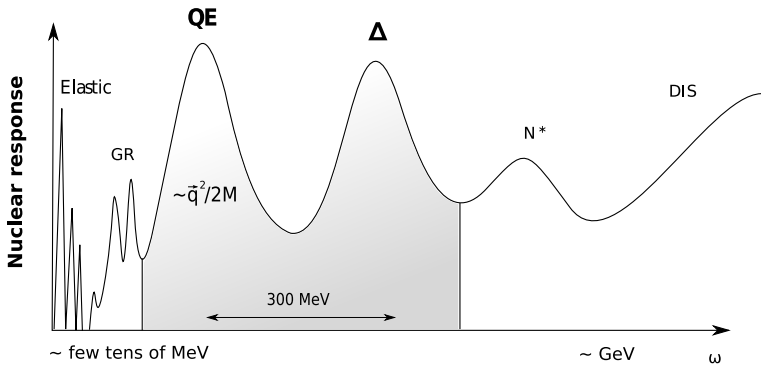

Figure 1.1: Schematic overview of the nuclear response to a weak probe as a function of ω. We consider situations of moderate four-momentum transfers q^2.

Neutrino-nucleus interactions at medium energies

To see what processes contribute to the reaction strength at few-GeV incoming-neutrino energies, we consider Fig. 1.1. There, the response of the nucleus is displayed as a function of the energy ω which is transferred to the system. Small energy transfers result in the elastic peak, followed by inelastic scattering where the nucleus is excited into discrete states. Just above the particle-emission threshold lies the giant-resonance region (GR).
The focus of this work will be on the energy region beyond the nucleon-emission threshold, up to $\sim$ 1 GeV energy transfers, and moderate values of $q^2 = q_\mu q^\mu$, with $q^\mu = (\omega, \vec{q})$ the transferred four-momentum. There, one first distinguishes a broad peak that is centered about $\omega \sim |\vec{q}\,|^2/2M$, where M represents the nucleon mass. This peak corresponds to the quasi-elastic (QE) nucleon-knockout process. A similar structure appears when an extra energy of 300 MeV is added to the nuclear system. In that case, the transferred energy is sufficient to excite a single nucleon to a Δ particle, resulting in the observed Δ peak. One refers to the region between the QE and Δ peaks as the dip region. Although no dominant reaction mechanism has been identified so far, two-body mechanisms like meson-exchange and isobar currents are recognized to play an important role there. At even higher energy transfers, it becomes possible to excite higher-lying nucleon isobars. Eventually, for $\omega \sim 1$ GeV, one enters the deep-inelastic scattering (DIS) regime, where the impinging neutrinos start probing quark degrees of freedom. In this thesis, we concentrate on a description of neutrino-nucleus interactions in the QE and Δ regions.
The QE and Δ peaks have in common that they are dominated by one-body mechanisms. In these regions, processes whereby a single bound nucleon absorbs the

entire four-momentum of the weak vector boson account for the major fraction of the strength. This observation is reflected in the frequently-used impulse approximation (IA), which states that the many-body operator describing the transition between final and initial nuclear states can be replaced by a sum of one-body current operators, which are free from medium effects. Hence, employing the IA, the modeling of neutrino-nucleus processes decouples into two main problems:

- How to describe the elementary (one-body) weak process?
- How to include nuclear effects?

The phenomenological form-factor approach

At energy transfers $\omega \leq 1$ GeV, the elementary process is most naturally described in terms of hadronic degrees of freedom. Then, to lowest order, the invariant matrix element for a semileptonic weak process is proportional to the contraction of a lepton and a hadron current, $M_{fi} \sim l_\alpha h^\alpha$. Whereas the $V-A$ nature of weak interactions fully determines the lepton current, the hadron current will generally assume a more complex form. Instead of computing the hadron couplings from first principles in quark models, one usually resorts to a more phenomenological point of view by introducing a set of vector and axial-vector form factors. These form factors account for the finite size of hadrons by playing the role of *running* electroweak coupling constants. Often, form factors can be parameterized as dipole functions of $Q^2 = -q^2$. As a consequence, each form factor introduces at least two parameters, namely a cutoff mass that acts as a size parameter and the value at $Q^2 = 0$, that determines the strength of the coupling. These parameters need to be constrained by physical principles and experimental data. In addition, the form factors can be tested against predictions of nucleon models. Within this context, it is worth mentioning that one of the major goals of neutrino experiments like SciBooNE and Minerνa is providing better constraints for the poorly-known axial mass M_A.
One must realize, however, that the mentioned experiments use a variety of target nuclei, including He, C, Fe and Pb. It is therefore crucial to understand the role of nuclear effects when extracting form-factor information.

Nuclear effects

The impinging neutrino interacts with a nucleon, moving inside a nucleus. Traditionally, the effects of Fermi motion, Pauli blocking and nuclear binding are accommodated within a relativistic Fermi-gas (RFG) description [17] of the nucleus. More advanced and realistic descriptions of nuclear structure include the relativistic shell model [18–21] and spectral-function approaches [22, 23], which extend beyond the mean-field picture. In this work, we adopt an independent-particle model (IPM) for

the nucleus, where the single-particle wave functions are obtained in the Hartree approximation to the σ-ω Walecka model [19, 24]. Assuming fully occupied shell-model orbitals, we do not take into account the effect of short-range nucleon-nucleon correlations, which contribute to the high-energy and high-momentum part of the spectral function. Other studies include long-range correlations by performing (Continuum) Random-Phase Approximation ((C)RPA) calculations [25–28]. At small Q^2, when the nucleus is probed with lower spatial resolution, multi-nucleon processes may indeed become important. In that case, the IA is no longer justifiable and RPA correlations produce sizeable effects. Throughout this text, however, we assume the IA to be a valid approximation in the energy region dominated by the QE and Δ peaks.

Another nuclear effect stems from the fact that the particles, produced in the primary weak interaction, are subject to final-state interactions (FSI) with the remaining nucleons on their way out of the nucleus. With respect to the QE process, one should compute the attenuation of the escaping nucleon. For Δ production, the effect is twofold. First, the Δ mass and width are modified in a medium. Second, once the Δ particle has decayed, the decay products (mostly a pion and a nucleon, sometimes only a nucleon) undergo FSI. Δ medium modifications can be estimated by calculating the in-medium self-energy in a microscopic many-body framework [29]. The resulting shift in the mass and collisional broadening of the width are necessary to account for photo-induced two-nucleon knockout data in an energy regime that is dominated by Δ creation [30]. For nucleon-knockout reactions, the attenuation of the outgoing nucleon is usually computed in optical-potential models within the relativistic distorted-wave IA (RDWIA) [18, 19, 31–35], or in Glauber models [19, 36, 37], which are multiple-scattering extensions of the eikonal approximation. In exclusive and semi-exclusive electron-scattering studies, where the single-particle strength can be well isolated, both of these approaches provide a fair, quantum-mechanical description of the $(e, e'N)$ data [38]. The Glauber model developed in Gent [37], which has been dubbed the relativistic multiple-scattering Glauber approximation (RMSGA), has subsequently been applied to QE neutrino-nucleus reactions [19] and will serve to compute FSI effects in this work. Other techniques to describe the propagation of pions and nucleons through nuclei include Monte-Carlo simulation methods [25, 39, 40] and semi-classical transport models [41, 42]. At the cost of giving up a fully quantum-mechanical description, the transport models improve on the RMSGA by including inelasticities and coupled-channel effects. Whereas the Glauber model predicts the amount of flux loss in a specific channel, the transport model additionally predicts the cross-feeding into other channels.

At present, the incorporation of nuclear effects in neutrino-event generators is being actively addressed by collaborations of experimentators and nuclear physicists. As a matter of fact, the recent analysis of MiniBooNE's QE result in terms of a Fermi-gas model [43] has undeniably shown the timeliness of such an effort. Now that neutrino

experiments enter the precision phase, it is our task to cross-check different nuclear models, and to distill a framework that can serve as a dependable platform for future event selections and analyses.

Outline

This thesis has been organized in two major parts, covering the processes of neutrino-induced QE nucleon knockout and Δ-mediated one-pion production respectively.

- Chapter 2 deals with QE neutrino-nucleus reactions. We discuss the kinematics and cross section of the process. Introducing the IA and the IPM, the basic ingredient in the formalism is the hadronic current matrix element between a bound-state and scattering wave function. We derive a form-factor parameterization for the hadronic current operator, and cover in detail how the form factors are constrained by theoretical principles and experimental data. As for the nuclear model, we use bound-state wave functions derived in the σ-ω Walecka model. It is shown how the cross section can be presented in a relatively simple, closed form by introducing the notion of a bound-state propagator. To account for FSI effects, we use a scattering wave function obtained within the RMSGA. Results are presented for various electron- and neutrino-induced distributions and for different target nuclei. We study several applications of QE neutrino scattering, including strangeness studies and the use of the Paschos-Wolfenstein relation as a tool to determine the Weinberg angle at medium energies. In an attempt to put our work into a more general perspective, we conclude with a comparison to other QE approaches.

- In Chapter 3, we study the process of Δ-mediated one-pion production. Elementary couplings, notably the N-Δ transition form factors and Δ-decay vertex, are discussed in detail. Results for the free process are compared to available neutrino data. For the reactions involving finite nuclei, a great deal of the nuclear-structure input is identical to what is used in Chapter 2. The impact of nuclear effects, including Δ medium modifications, on the cross section is illustrated for various target nuclei. We consider the process of coherent pion production, computing the attenuation of the pion within the RMSGA.

In the concluding chapter, we summarize our findings. A brief outlook is presented, indicating future directions of research that are meant to help developing a reliable model for medium-energy neutrino-nucleus interactions.

2

Quasi-elastic nucleon knockout

In this chapter we focus on quasi-elastic (QE) neutrino-nucleus interactions. The term *quasi-elastic* refers to those processes where a bound nucleon is knocked straight out of the nucleus, leaving the residual nuclear system with an excitation energy that does not exceed a few tens of MeV. Section 2.1 provides a general introduction to nucleon-knockout reactions. First, we discuss the kinematics of the process and derive the cross-section formula. The Rosenbluth-separation form of the cross section is worked out. In section 2.2, we show how the building blocks of the nuclear responses, namely the nuclear-current matrix elements, can be reduced to one-body expressions. The further development of the framework boils down to determining appropriate expressions for the one-body hadron current, for which a form-factor parameterization is developed in section 2.3. Theoretical and experimental constraints on all weak elastic form factors are discussed there. In section 2.4, it is explained how we account for nuclear effects such as the motion of the struck nucleon inside the nucleus and final-state interactions undergone by the ejectile on its way out of the nucleus. Section 2.5 presents our results for QE nucleon-knockout cross sections. Both electron- and neutrino-induced reactions are considered, comparing the former to inclusive and semi-inclusive scattering data. As an application of QE neutrino scattering, we consider a study of the Paschos-Wolfenstein relation in section 2.6, to test its potential as an electroweak precision tool at medium energies. Section 2.7 is devoted to the role played by strange quarks in QE studies. Finally, in section 2.8, we compare our work to other QE neutrino-scattering approaches.

2.1 Neutrino-induced nucleon-knockout cross sections

2.1.1 Kinematics and cross section

A semi-leptonic interaction between a neutrino and a nucleus occurs through the exchange of a weak vector boson. We distinguish neutral-current (NC) processes, mediated by a Z^0 particle, and charged-current (CC) processes, where a W^+ or W^- is exchanged between the lepton and hadron current. The neutrino-induced QE nucleon-knockout reactions can be written as

$$\begin{aligned} \nu + A &\xrightarrow{\text{NC}} \nu + (A-1) + N, \\ \nu + A &\xrightarrow{\text{CC}} l^- + (A-1) + p. \end{aligned} \tag{2.1}$$

Similarly, for an incoming antineutrino one has

$$\begin{aligned} \overline{\nu} + A &\xrightarrow{\text{NC}} \overline{\nu} + (A-1) + N, \\ \overline{\nu} + A &\xrightarrow{\text{CC}} l^+ + (A-1) + n. \end{aligned} \tag{2.2}$$

Here, the target nucleus is represented by its mass number A. The outgoing charged lepton and the emitted nucleon are denoted by l and N. For CC processes, the charge exchange at the vertex determines the nature of the emitted nucleon (proton p or neutron n).
To derive an expression for the QE cross sections, we start from the general formula [44]

$$\begin{aligned} d^9\sigma = \frac{1}{\beta}\frac{m_\nu}{E_\nu}\frac{m_l}{E_l}\frac{d^3\vec{k}_l}{(2\pi)^3}\frac{m_N}{E_N}\frac{d^3\vec{k}_N}{(2\pi)^3}\frac{m_{A-1}}{E_{A-1}}\frac{d^3\vec{k}_{A-1}}{(2\pi)^3} \\ \times\overline{\sum}_{fi}\left|M_{fi}^{(QE)}\right|^2(2\pi)^4\delta^{(4)}(k_\nu + k_A - k_l - k_N - k_{A-1}). \end{aligned} \tag{2.3}$$

For the Dirac spinors, we adopt the Bjorken & Drell convention $\overline{u}u = 1$. In appendix A, a review of notations and conventions is provided. Equation (2.3) is usually evaluated in the laboratory frame of reference, where the target nucleus has four-momentum $k_A^\mu = (m_A, \vec{0})$ with m_A its rest mass. Fig. 2.1 clarifies our choice of reference frame and summarizes the notations for the four-momenta of all participating particles. We write $k_\nu^\mu = (E_\nu, \vec{k}_\nu)$ for the incoming (anti)neutrino and $k_l^\mu = (E_l, \vec{k}_l)$ for the outgoing lepton. A four-momentum $q^\mu = k_\nu^\mu - k_l^\mu = (\omega, \vec{q})$ is absorbed by the nucleus, which subsequently emits a nucleon with four-momentum $k_N^\mu = (E_N, \vec{k}_N)$. The recoiling nucleus has $k_{A-1}^\mu = (E_{A-1}, \vec{k}_{A-1})$. The xyz coordinate system is chosen such that the z axis lies along the momentum transfer $\vec{q}$, the y axis along $\vec{k}_\nu \times \vec{k}_l$, and the x axis in

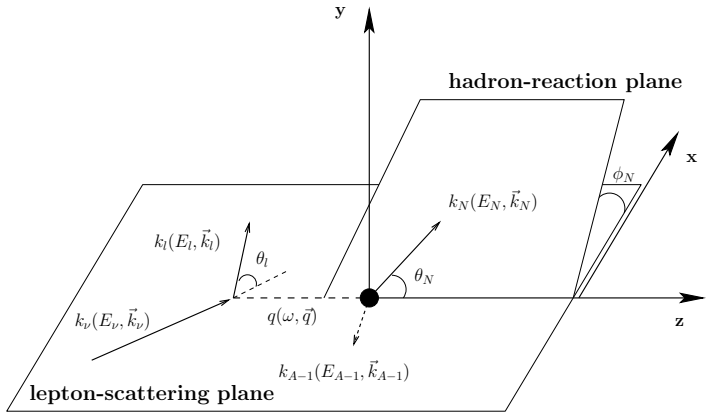

Figure 2.1: Kinematics for the quasi-elastic nucleon-knockout process

the lepton-scattering plane.
In Eq. (2.3), the impinging neutrino's relative velocity $\beta = |\vec{k}_\nu|/E_\nu$ is 1. The δ-function expresses energy-momentum conservation and $\overline{\sum}_{fi}|M_{fi}^{(QE)}|^2$ denotes the squared invariant matrix element, which is appropriately averaged over initial spins and summed over final spins. The invariant matrix element $M_{fi}^{(QE)}$ is the Lorentz scalar that contains all the physics of the QE reaction mechanism. To proceed, the δ-function is exploited to integrate over the three-momentum of the residual nucleus and the magnitude of the nucleon momentum. One arrives at the fivefold cross section

$$\frac{d^5\sigma}{dE_l d^2\Omega_l d^2\Omega_N} = \frac{m_\nu m_l m_N m_{A-1} k_l k_N}{E_\nu (2\pi)^5 m_A} f_{rec}^{-1} \overline{\sum_{if}} \left| M_{fi}^{(QE)} \right|^2, \tag{2.4}$$

which depends on the solid angles Ω_l and Ω_N, determining the direction of the scattered lepton and ejectile respectively. In Eq. (2.4), the hadronic recoil factor f_{rec} is given by

$$f_{rec} = \frac{E_{A-1}}{m_A} \left| 1 + \frac{E_N}{E_{A-1}} (1 - \frac{\vec{q} \cdot \vec{k}_N}{k_N^2}) \right|. \tag{2.5}$$

2.1.2 General structure of the QE cross section

The invariant matrix element for the QE process can be constructed by applying the Feynman rules in momentum space. To this end, Fig. 2.2 recapitulates the necessary coupling strengths. Because of the small value of the weak coupling constant $g = e/\sin\theta_W$, it is safe to work in the one-boson-exchange approximation. Compared to

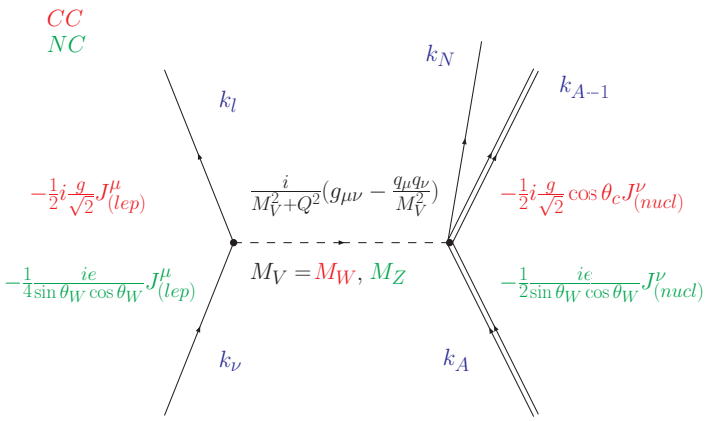

Figure 2.2: Diagram for tree-level neutrino-induced QE nucleon-knockout calculations.

the boson masses $M_Z, M_W \sim 80$ GeV, the transferred energies and momenta that are typical for QE scattering ($\lesssim 1$ GeV) can be considered negligible. Hence, the boson propagator can be written as

$$\frac{i}{M_V^2+Q^2}(g_{\mu\nu}-\frac{q_\mu q_\nu}{M_V^2}) \approx \frac{ig_{\mu\nu}}{M_V^2+Q^2}, \tag{2.6}$$

where $Q^2 = -q_\rho q^\rho$ is the momentum transfer squared. With the couplings in Fig. 2.2, one can easily construct the matrix element for a NC process

$$M_{fi}^{(QE)} = i\frac{G_F}{\sqrt{2}}\langle J^{\mu(QE)}_{nucl}\rangle S_{W,\mu\nu}\langle J^{\nu}_{lep}\rangle. \tag{2.7}$$

Here, G_F is the Fermi constant, for which $G_F/\sqrt{2} = g^2/8M_W^2$. Further on, the vertex functions $J^{\mu(QE)}_{nucl}$ and J^{ν}_{lep} are placed between brackets to indicate that they are evaluated between final and initial states. With

$$S_{W,\mu\nu} = \frac{g_{\mu\nu}M_Z^2}{Q^2+M_Z^2}, \tag{2.8}$$

the squared invariant matrix element can be cast in the form

$$\overline{\sum_{fi}}\left|M_{fi}^{(QE)}\right|^2 = \frac{G_F^2 M_Z^4}{2(M_Z^2+Q^2)^2}H^{\mu\nu}_{(QE)}L_{\mu\nu}. \tag{2.9}$$

The corresponding expression for the CC process is found by replacing M_Z by M_W and multiplying Eq. (2.9) with $\cos^2\theta_C$, the Cabibbo angle squared.
Combining Eqs. (2.9) and (2.4), the cross section is seen to be proportional to the contraction of the hadron tensor $H^{\mu\nu}_{(QE)}$ and the lepton tensor $L_{\mu\nu}$. The latter is given by

$$L_{\mu\nu} = \overline{\sum_{s_\nu, s_l}} \langle J_{\mu,lep}\rangle^\dagger \langle J_{\nu,lep}\rangle. \tag{2.10}$$

Introducing the Dirac spinors $u(k_\nu, s_\nu)$ and $u(k_l, s_l)$ for the incoming neutrino and scattered lepton, the lepton-current matrix element can be written as

$$\langle J_{\mu,lep}\rangle = \overline{u}(k_l, s_l)\gamma_\mu(1 + h\gamma_5)u(k_\nu, s_\nu), \tag{2.11}$$

where h denotes the helicity of the incoming particle ($h = -1$ for neutrinos, $h = +1$ for antineutrinos). The $V - A$ ($V + A$) structure of the lepton current in Eq. (2.11) reflects the maximally parity-violating character of (anti)neutrino interactions. Using Eq. (2.11) in Eq. (2.10), the lepton tensor is found to be

$$L_{\mu\nu} = \frac{2}{m_\nu m_l}(k_{\nu,\mu}k_{l,\nu} + k_{\nu,\nu}k_{l,\mu} - k_\nu \cdot k_l g_{\mu\nu} + h\, i\epsilon_{\alpha\mu\beta\nu}k_\nu^\alpha k_l^\beta), \tag{2.12}$$

with the definition $\epsilon_{0123} = +1$.
The hadron tensor is written in a similar way as an expression that is bilinear in the nuclear-current matrix elements

$$H^{\mu\nu}_{(QE)} = \overline{\sum_{fi}} \langle J^{\mu(QE)}_{nucl}\rangle^\dagger \langle J^{\nu(QE)}_{nucl}\rangle. \tag{2.13}$$

The nuclear-current matrix element $\langle J^{\mu(QE)}_{nucl}\rangle$ is much harder to write down than the lepton-current one, as it involves the evaluation of many-body operators between final and initial nuclear states. However, for the purpose of studying some general features of the QE cross section, the expression Eq. (2.13) is fine. An in-depth discussion of the nuclear-current matrix element is postponed to the next section.
Let us now consider the contraction of the lepton and the hadron tensor. To do so, we closely follow the method outlined in Ref. [45]. Next to the lepton tensor of Eq. (2.12), the hadron tensor can be constructed as a second-rank Lorentz tensor

$$H^{\mu\nu} = H^{\mu\nu}_{VV} + H^{\mu\nu}_{VA} + H^{\mu\nu}_{AA}, \tag{2.14}$$

where V refers to a vector and A to an axial nuclear current. The different terms in Eq. (2.14) are built from the four-momenta of the participating particles, namely q, k_A and k_N. Each term of the hadron tensor in Eq. (2.14) has a corresponding response function, which can only depend on the Lorentz scalars derived from the above four-momenta. Choosing the frame of reference as in Fig. 2.1, it is immediately seen that

the response functions are independent of ϕ_N, the ejected nucleon's azimuthal angle. For the NC cross sections, the contraction of the lepton and hadron tensors leads to

$$\frac{d^5\sigma}{dE_l d^2\Omega_l d^2\Omega_N} = \frac{m_N m_{A-1} k_N}{(2\pi)^3} f_{rec}^{-1} \sigma^Z \left[v_L R_L + v_T R_T + v_{TT} R_{TT} \cos 2\phi_N + v_{TL} R_{TL} \cos\phi_N \right. \\ \left. + h(v'_T R'_T + v'_{TL} R'_{TL} \cos\phi_N) \right]. \tag{2.15}$$

In Eq. (2.15), we used

$$\sigma^Z = \left(\frac{G_F \cos(\theta_l/2) E_l M_Z^2}{\sqrt{2}\pi(Q^2 + M_Z^2)} \right)^2, \tag{2.16}$$

and the definitions of Table 2.1. Equation (2.15) provides a way to access the longitudinal (L), transverse (T) and interference (TL) nuclear responses, by measuring the ejected nucleon in coincidence with the scattered lepton. In this sense, the Rosenbluth formula in Eq. (2.15) has been an important tool for nuclear-structure studies using various exclusive and semi-exclusive channels in electron-scattering experiments [32, 38, 46, 47]. The primed contributions stem from contractions with the antisymmetric part of the lepton tensor. Consequently, they acquire a different sign depending on the nature of the incident particles (neutrino or antineutrino). Due to the non-vanishing mass of the outgoing lepton, CC processes imply expressions that are slightly more involved. The expressions for the kinematic factors and response functions are listed in the lower part of Table 2.1. Furthermore, σ^Z has to be replaced by $\sigma^{W^\pm}$ where

$$\sigma^{W^\pm} = \left(\frac{G_F \cos(\theta_c) E_l M_W^2}{2\pi(Q^2 + M_W^2)} \right)^2 \zeta, \quad \zeta = \sqrt{1 - \frac{m_l^2}{E_l^2}}. \tag{2.17}$$

2.2 Nuclear-current matrix element

In the previous section, we derived a useful expression for neutrino-induced nucleon-knockout cross sections. The basic quantities that emerged from this discussion are the nuclear-current matrix elements $\langle J^{\mu(QE)}_{nucl} \rangle$; they are the building blocks of the electroweak nuclear responses we wish to study. Moreover, all the information about the elementary reaction mechanism and the nuclear dynamics is contained in these objects. As a consequence, the nuclear-current matrix elements will be at the center of our modeling efforts.
In general, one can write

$$\left\langle J^{\mu(QE)}_{nucl} \right\rangle = \left\langle (A-1)(J_R M_R), k_N m_s \left| \hat{J}^{\mu(QE)}_{nucl} \right| A(0^+, g.s.) \right\rangle, \tag{2.18}$$

Table 2.1: Kinematic factors and response functions for NC and CC (anti)neutrino-nucleus scattering. Hadronic matrix elements are expressed in the spherical basis $\vec{e}_z$, $\vec{e}_{\pm1} = \mp\frac{1}{\sqrt{2}}(\vec{e}_x \pm i\vec{e}_y)$, $\mathscr{J}^\mu = (\mathscr{J}^0, \vec{\mathscr{J}})$ with $\vec{\mathscr{J}} = -\mathscr{J}^{-1}\vec{e}_{+1} - \mathscr{J}^{+1}\vec{e}_{-1} + \mathscr{J}^z\vec{e}_z$. For the CC case, we only list those expressions that differ from the NC ones.

Kinematic factors			**Response functions**		
Neutral current					
v_L	$=$	1	R_L	$=$	$\left\lvert\mathscr{J}^0 - \frac{\omega}{q}\mathscr{J}^z\right\rvert^2$
v_T	$=$	$\tan^2\frac{\theta_l}{2} + \frac{Q^2}{2q^2}$	R_T	$=$	$\left\lvert\mathscr{J}^{+1}\right\rvert^2 + \left\lvert\mathscr{J}^{-1}\right\rvert^2$
v_{TT}	$=$	$-\frac{Q^2}{2q^2}$	$R_{TT}\cos 2\phi$	$=$	$2\Re\left((\mathscr{J}^{+1})^\dagger\mathscr{J}^{-1}\right)$
v_{TL}	$=$	$-\frac{1}{\sqrt{2}}\sqrt{\tan^2\frac{\theta_l}{2} + \frac{Q^2}{q^2}}$	$R_{TL}\cos\phi$	$=$	$-2\Re\left(\mathscr{J}^0 - \frac{\omega}{q}\mathscr{J}^z\right)(\mathscr{J}^{+1} - \mathscr{J}^{-1})^\dagger$
v'_T	$=$	$\tan\frac{\theta_l}{2}\sqrt{\tan^2\frac{\theta_l}{2} + \frac{Q^2}{q^2}}$	R'_T	$=$	$\left\lvert\mathscr{J}^{+1}\right\rvert^2 - \left\lvert\mathscr{J}^{-1}\right\rvert^2$
v'_{TL}	$=$	$\frac{1}{\sqrt{2}}\tan\frac{\theta_l}{2}$	$R'_{TL}\cos\phi$	$=$	$-2\Re\left(\mathscr{J}^0 - \frac{\omega}{q}\mathscr{J}^z\right)(\mathscr{J}^{+1} + \mathscr{J}^{-1})^\dagger$
Charged current					
$v_L R_L$	$=$	$\left(1+\zeta\cos\theta_l\right)\lvert\mathscr{J}^0\rvert^2 + \left(1+\zeta\cos\theta_l - \frac{2E_\nu E_l}{q^2}\zeta^2\sin^2\theta_l\right)\lvert\mathscr{J}^z\rvert^2$ $- \left(\frac{\omega}{q}\left(1+\zeta\cos\theta_l\right) + \frac{m_l^2}{E_l q}\right)2\Re(\mathscr{J}^0(\mathscr{J}^z)^\dagger)$			
v_T	$=$	$1 - \zeta\cos\theta_l + \frac{E_\nu E_l}{q^2}\zeta^2\sin^2\theta_l$			
v_{TT}	$=$	$-\frac{E_\nu E_l}{q^2}\zeta^2\sin^2\theta_l$			
$v_{TL}R_{TL}\cos\phi$	$=$	$\frac{\sin\theta_l}{\sqrt{2}q}(E_\nu + E_l)\left(2\Re\left(\left(\mathscr{J}^0 - \frac{\omega}{q}\mathscr{J}^z\right)(\mathscr{J}^{+1} - \mathscr{J}^{-1})^\dagger - \frac{m_l^2}{q}\mathscr{J}^z(\mathscr{J}^{+1} - \mathscr{J}^{-1})^\dagger\right)\right)$			
v'_T	$=$	$\frac{E_\nu + E_l}{q}\left(1 - \zeta\cos\theta_l\right) - \frac{m_l^2}{E_l q}$			
v'_{TL}	$=$	$-\frac{\sin\theta_l}{\sqrt{2}}\zeta$			

where $|A(0^+, g.s.)\rangle$ and $\langle (A-1)(J_R M_R)|$ denote the wave functions of the nuclear ground state and the single-hole state of the residual system, respectively.

2.2.1 Impulse approximation

To simplify the calculation of Eq. (2.18), it is a common practice in medium-energy applications to introduce a number of approximations. First of all, one should understand that the QE reaction mechanism involves the direct emission of a nucleon. In other words, the detected nucleon comes straight from the vertex where it absorbed an energy ω and a momentum $\vec{q}$. It is assumed that the major fraction of the transferred energy is carried by the ejectile, leaving the residual nucleus with an excitation energy not exceeding a few tens of MeV. Indeed, higher excitation energies point towards other reaction mechanisms starting to play a role, such as two- and multi-nucleon knockout processes. The reaction strength there can be at least partially understood in terms of two-body meson-exchange currents [48, 49]. In this thesis, however, we will not consider processes that involve several target nucleons. Under these conditions, it is natural to invoke the impulse approximation (IA), which states the replacement of the nuclear many-body current operator by a sum of one-body current operators

$$\hat{J}^{\mu(QE)}_{nucl} \longrightarrow \sum_{k=1}^{A} \hat{J}^{\mu(QE)}(\vec{r}_k). \tag{2.19}$$

The operators in Eq. (2.19) are assumed to be exempted from medium effects, reflecting the quasi-free nature of the QE process. In particular, we adopt the philosophy that the in-medium vertex function $J^{\mu(QE)}$ has the same Lorentz structure as the free-nucleon one. Possible medium modifications to the free-nucleon's form factors will be ignored, as searches in $A(e, e'p)$ studies have only led to small effects [50, 51]. For neutrino-induced nucleon knockout, the $\hat{J}^{\mu(QE)}$ represent weak one-nucleon currents between an initial, bound nucleon and a final, scattered nucleon. Employing an independent-particle model (IPM), the nuclear wave functions are obtained by fully anti-symmetrizing the product of single-nucleon wave functions. It can be shown that each term of Eq. (2.19) yields the same contribution to the matrix element of Eq. (2.18), given by

$$\left\langle J^{\mu(QE)} \right\rangle = \int d\vec{r}\, \overline{\phi}_F(\vec{r}) \hat{J}^{\mu(QE)}(\vec{r}) e^{i\vec{q}\cdot\vec{r}} \phi_B(\vec{r}). \tag{2.20}$$

In Eq. (2.20), the ϕ_B and ϕ_F represent relativistic bound-state and scattering wave functions.

2.2.2 Nucleon-knockout dynamics

Working in the impulse approximation, it is instructive to review some kinematical and dynamical aspects of the QE process. Within the IA, the scattering from a nucleus is described as an incoherent sum of one-body contributions. For a bound nucleon with four-momentum $k^\mu = (E, \vec{p})$, the energy-momentum relations become

$$\omega + E = E_N, \quad \vec{q} + \vec{p} = \vec{k}_N. \tag{2.21}$$

Combined with the general expression

$$q(\omega, \vec{q}) + k_A(m_A, \vec{0}) = k_N(E_N, \vec{k}_N) + k_{A-1}(E_{A-1}, \vec{k}_{A-1}), \tag{2.22}$$

one obtains $\vec{p} = -\vec{k}_{A-1}$. We define $\vec{p}_m \equiv \vec{p}$ as the missing momentum. The residual nucleus recoils with kinetic energy $T_{A-1} \approx p_m^2/2m_{A-1}$. Similarly, the missing energy is defined as

$$E_m = \omega - T_N - T_{A-1}, \tag{2.23}$$

where $T_N = E_N - m_N$. Equation (2.23) can be interpreted as the separation energy for a particular hole state of the (A−1) system. Its relation to the excitation energy of the residual nucleus is given by $E_{exc} = E_m - E_s$, where E_s is the nucleon separation energy.

2.3 Weak one-nucleon current operator

2.3.1 Form-factor parameterization

We now wish to obtain an expression for the weak one-nucleon current operator $\hat{J}^{\mu(QE)}(\vec{r})$. For on-mass shell nucleons, the matrix element in Eq. (2.20) is written in terms of the Dirac spinors as [6]

$$\left\langle J^{\mu(QE)} \right\rangle = \overline{u}(k_f, s_f)\hat{J}^\mu(k_f, k_i)u(k_i, s_i). \tag{2.24}$$

Generally speaking, we wish to construct an operator $\hat{J}^\mu$ that transforms like a four-vector and obeys some general physical principles and symmetries. Lorentz covariance is automatically imposed by manifestly working with tensors. The most basic procedure then consists of collecting all possible four-vectors to parameterize $\hat{J}^\mu$. Using Dirac algebra and Gordon-like identities to remove equivalent terms amongst the available four-momenta, γ matrices and other possible combinations, one arrives at the following expression [52]

$$\begin{aligned}\hat{J}^\mu =& \hat{J}^\mu_V + \hat{J}^\mu_A \\ =& f_1(Q^2)q^\mu + f_2(Q^2)\gamma^\mu + f_3(Q^2)\sigma^{\mu\nu}q_\nu \\ &+ f_4(Q^2)q^\mu\gamma_5 + f_5(Q^2)\gamma^\mu\gamma_5 + f_6(Q^2)\epsilon^{\mu\nu\alpha\beta}\sigma_{\alpha\beta}q_\nu.\end{aligned} \tag{2.25}$$

Because the nucleons have a finite extension, we have to allow a *running* of the couplings to the different terms in Eq. (2.25). To this end, we introduce six form factors ($f_i, \quad i = 1..6$), which are Lorentz-scalar functions of the squared momentum transfer Q^2. The parity-violating nature of weak interactions enforces the presence of both vector (f_1, f_2 and f_3) and axial-vector (f_4, f_5 and f_6) contributions. Yet, not all terms are equally important. The term proportional to f_6, for example, is odd under the time-reversal transformation. Physical processes that violate this symmetry are very scarce [6], so f_6 is usually put to 0. Indeed, one of the most sensitive ways to look for T violation is the search for an electric dipole moment of the neutron or the electron, for which no non-zero value has been reported yet [53]. The vector terms of Eq. (2.25) can be further constrained by recognizing that the weak vector current and the isovector part of the electromagnetic current are components of the same isospin current. As a consequence, the weak vector current is also a conserved quantity. This is called the conserved vector current (CVC) hypothesis [54], which is invoked in momentum space by putting $q_\mu \hat{J}^\mu_V = 0$. Applying CVC to Eq. (2.25) entails $f_1 = 0$ for each Q^2. Furthermore, the remaining form factors are ensured to be real by imposing that the weak current is hermitian. Adopting the widely-used notations for the terms that are left, one arrives at the following expression for the weak one-nucleon current operator

$$\hat{J}^\mu = F_1(Q^2)\gamma^\mu + \frac{i}{2m_N}F_2(Q^2)\sigma^{\mu\nu}q_\nu + G_A(Q^2)\gamma^\mu\gamma_5 + G_P(Q^2)q^\mu\gamma_5. \tag{2.26}$$

The vector part is described by the weak Dirac and Pauli form factors F_1 and F_2, whereas the axial part is parameterized as a function of the axial form factor G_A and pseudoscalar form factor G_P. In literature, one refers to Eq. (2.26) as the $cc2$ form of the current operator. Through the Gordon identity, the $\hat{J}^\mu$ for a free nucleon can assume a large number of equivalent forms, including [55, 56]

$$\begin{aligned}
\hat{J}^\mu_{cc1} &= G_M(Q^2)\gamma^\mu - \frac{1}{2m_N}F_2(Q^2)(k_i^\mu + k_N^\mu) + G_A(Q^2)\gamma^\mu\gamma_5 + G_P(Q^2)q^\mu\gamma_5, \\
\hat{J}^\mu_{cc3} &= \frac{1}{2m_N}F_1(Q^2)(k_i^\mu + k_N^\mu) + \frac{i}{2m_N}G_M(Q^2)\sigma^{\mu\nu}q_\nu + G_A(Q^2)\gamma^\mu\gamma_5 + G_P(Q^2)q^\mu\gamma_5.
\end{aligned} \tag{2.27}$$

When applying these vertex functions in connection to bound nucleons, as is the case in Eq. (2.20), they will generally not produce identical results. Thus, for the description of nuclear reactions, the various expressions for $\hat{J}^\mu$ give rise to model dependences, better known as off-shell ambiguities. For neutrino-induced reactions, however, the effect is rather modest owing to the dominant axial coupling.

2.3.2 Weak vector and axial form factors

Weak vector form factors

The form factors F_1 and F_2 are connected to the electric and magnetic Sachs form factors G_E and G_M through the relations $G_E = F_1 - \tau F_2$ and $G_M = F_1 + F_2$, with $\tau = Q^2/4m_N^2$. A functional form for the weak vector form factors can be derived from the CVC hypothesis, which relates them to the electromagnetic isovector $F_i^{EM,V} = F_{i,p}^{EM} - F_{i,n}^{EM}$ and isoscalar $F_i^{EM,S} = F_{i,p}^{EM} + F_{i,n}^{EM}$ ones. This leads to

$$F_i = \begin{cases} (\frac{1}{2} - \sin^2\theta_W)F_i^{EM,V}\tau_3 - \sin^2\theta_W F_i^{EM,S} - \frac{1}{2}F_i^s & \text{NC} \\ \\ F_i^{EM,V}\tau_\pm & \text{CC,} \end{cases} \tag{2.28}$$

where $i = 1, 2$. In Eq. (2.28), the electroweak mixing angle $\sin^2\theta_W = 0.2224$ [57] is introduced. The operators $\tau_\pm$ and τ_3 work in isospin space and are defined as

$$\begin{aligned} \tau_3|p\rangle &= +|p\rangle, \quad \tau_3|n\rangle = -|n\rangle, \\ \tau_+|n\rangle &= +|p\rangle, \quad \tau_+|p\rangle = 0, \\ \tau_-|p\rangle &= -|n\rangle, \quad \tau_-|n\rangle = 0. \end{aligned} \tag{2.29}$$

NC processes receive contributions from both isovector and isoscalar currents. Assuming that strange sea quarks play a similar role in protons and neutrons, part of the latter consists of the strangeness form factors F_1^s and F_2^s. Because of the isovector character of CC reactions, there is no strangeness sensitivity there.
The electromagnetic nucleon form factors $G_{E,n}, G_{M,n}, G_{E,p}$ and $G_{M,n}$ can be determined from elastic *eN* scattering data. Early measurements using the Rosenbluth-separation technique could be well accommodated with a dipole parameterization [32]

$$G_D(Q^2) = \frac{1}{(1 + \frac{Q^2}{M_V^2})^2}, \quad M_V = 843 \text{ MeV}. \tag{2.30}$$

At $Q^2 = 0$, the electric and magnetic Sachs form factors should reproduce the electric charge (in units of e) and anomalous magnetic moment, respectively. Therefore,

$$G_{Ep} = G_D, \quad G_{Mp} = \mu_p G_D, \quad G_{Mn} = \mu_n G_D, \tag{2.31}$$

with $\mu_p = 2.793$ and $\mu_n = -1.913$ (in units of the nuclear magneton $\mu_B = e\hbar/2m_p$). In general, the proton form factors can be well constrained from electron scattering off hydrogen. To the contrary, most of the information on the neutron form factors comes from elastic scattering from a deuterium target. Because of difficulties in modeling nuclear effects and experimental limits in neutron efficiency, the form factors $G_{Mn}(Q^2)$

Table 2.2: Fit parameters for the BBBA05 parameterization of Eq. (2.33), as taken from Ref. [62]. The a_0 impose the correct low-Q^2 behavior and were not adjusted during the fit.

Form factor	a_0	a_1	a_2	b_1	b_2	b_3	b_4
G_{Ep}	1	−0.0578	0.00	11.1	13.6	33.0	0.00
G_{Mp}	1	0.150	0.00	11.1	19.6	7.54	0.00
G_{En}	0	1.25	1.30	−9.86	305	−758	802
G_{Mn}	1	1.81	0.00	14.1	20.7	68.7	0.00

and $G_{En}(Q^2)$ are less well-known than their proton counterparts. For the neutron electric form factor, one usually adopts the Galster parameterization [58]

$$G_{En}(Q^2) = -\frac{\tau}{1+5.6\tau} G_{Mn}(Q^2), \tag{2.32}$$

which gives a fair description of elastic electron-deuteron scattering data. Owing to the successful description of low-Q^2 data, the parameterizations of Eqs. (2.31) and (2.32) have been the preferred ones in QE-scattering studies. Nevertheless, recent recoil-polarization measurements at JLab [59] have modified this simple picture. These data for the ratio $\mu_p G_{Ep}/G_{Mp}$ drop off linearly with Q^2, rather than staying approximately one, as one would expect from Eq. (2.31). To understand the discrepancy between the electromagnetic form factors obtained with the two techniques, most work has focused on two-photon exchange contributions to elastic electron-nucleon scattering [60]. It has now been theoretically established [60] that hard two-photon corrections, while hardly affecting the polarization-transfer results, do correct the slope of the Rosenbluth plots at larger Q^2, in a way that would reconcile both experimental techniques. As the polarization method is believed to be systematically more solid than the Rosenbluth-separation technique, the JLab result has spurred new efforts to find parameterizations that can also account for the new data at $Q^2 > 1$ GeV^2 [61–65]. In Ref. [62], a new fit is suggested based on a single functional form for all four elastic form factors

$$G(Q^2) = \frac{\sum_{k=0}^{2} a_k \tau^k}{1+\sum_{k=1}^{4} b_k \tau^k}. \tag{2.33}$$

The fit parameters for this so-called BBBA05 parameterization are summarized in Table 2.2. In Fig. 2.3, the difference between the BBBA05 and dipole parameterizations is shown for the proton form factors. For moderate Q^2 values, the BBBA05 fit agrees with the dipole behavior at the level of a few percent. Beyond $Q^2 > 1$ GeV^2, however, the BBBA05 parameterization starts to exhibit large deviations from the dipole one.

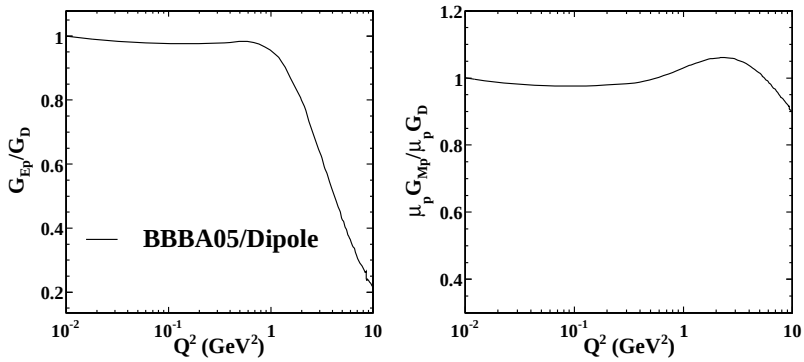

Figure 2.3: Ratio of BBBA05 to dipole functional form for the proton electric and magnetic form factors.

Vector strangeness form factors

To study the role of strange sea quarks in weak vector currents, we have introduced the strangeness form factors F_1^s and F_2^s in Eq. (2.28). A dispersion analysis using a three-pole ansatz results in the frequently used Forkel parameterization [66]

$$F_1^s = \frac{1}{6}\frac{-r_s^2 Q^2}{(1+\frac{Q^2}{M_1^2})^2}, \quad F_2^s = \frac{\mu_s}{(1+\frac{Q^2}{M_2^2})^2}, \tag{2.34}$$

where $M_1 = 1.3$ GeV and $M_2 = 1.26$ GeV. The strangeness contribution to the nucleon's charge and anomalous magnetic moment can be interpreted in terms of the corresponding Sachs form factors

$$G_E^s = F_1^s - \tau F_2^s, \quad G_M^s = F_1^s + F_2^s. \tag{2.35}$$

Since the nucleon's net strangeness charge is zero, one has $G_E^s(0) = 0$. An attractive tool to extract strangeness form-factor information is provided by parity-violating electron-scattering (PVES) [67, 68]. As we have seen, purely electromagnetic scattering provides access to the Sachs form factors $G_{E,M}$, which include the strangeness contributions in Eq. (2.35). The proton electric form factor, for example, can be decomposed in its quark terms as

$$G_{E,p}^{\gamma} = \frac{2}{3}G_E^u - \frac{1}{3}G_E^d - \frac{1}{3}G_E^s. \tag{2.36}$$

On the other hand, the neutral weak vector form factor reads

$$G_{E,p}^{Z} = \left(\frac{1}{4} - \frac{2}{3}\sin^2\theta_W\right) G_E^u + \left(-\frac{1}{4} + \frac{1}{3}\sin^2\theta_W\right)(G_E^d + G_E^s). \tag{2.37}$$

By measuring the asymmetry $A = (\sigma_R - \sigma_L)/(\sigma_R + \sigma_L)$, where $\sigma_{R(L)}$ refers to right (left) handed longitudinally polarized electrons, PVES experiments are sensitive to both of the combinations in Eqs. (2.36) and (2.37), making it possible to access the strangeness contributions.
In literature, detailed overviews of recent experimental efforts are available [69–71]. Different collaborations, such as HAPPEX (p, ^{4}He; $Q^2 \sim 0.1$ GeV^2) [72, 73], SAMPLE (p; $Q^2 = 0.1$ GeV^2) [74], A4 (p; $Q^2 = 0.108$ and 0.230 GeV^2) [75, 76] and G0 (p; $0.12 < Q^2 < 1.00$ GeV^2) [77], have measured the asymmetry A for various Q^2 and for hydrogen and helium targets. The contributions of G_E^s and G_M^s to A can be disentangled by combining results at forward and backward electron scattering angles. Forward scattering data are most sensitive to G_E^s, somewhat less sensitive to G_M^s, and almost completely insensitive to the axial form factors which are suppressed by $(1-4\sin^2\theta_W)$ and a kinematical factor that becomes 0 at forward angles [70]. A measurement at backward angles is dominated by the term containing G_M^s. On the other hand, it is also sensitive to the axial term, which is prone to electroweak radiative corrections. Information on this contribution can be extracted from a measurement of A from a deuterium target [74, 78], so that a combined analysis with backward scattering data yields a value for G_M^s. The PVES results, however, do not yet allow any definite statements about the vector strangeness content of the nucleon. As a matter of fact, all data are still compatible with $G_E^s = 0$. This is not fully unexpected, as the strange sea quarks do not contribute to the nucleon's total charge. On the other hand, some measurements [73, 74] point to small, positive values for the magnetic form factor G_M^s. Recent combined analyses of PVES data at $Q^2 = 0.1$ GeV^2 [69] and of PVES and neutrino-scattering data in the range $0.45 < Q^2 < 1.0$ GeV^2 [70] seem to confirm this picture.
Values for the strangeness radius r_s^2 and magnetic moment μ_s are also predicted in nucleon models. Overviews of hadron-model estimates for the strangeness vector form factors can be found in Refs. [71, 79, 80]. Here, we restrict ourselves to the selection of predictions presented in Table 2.3. Table 2.3 demonstrates the broad range of computed values, especially for F_1^s. Recognizing that sea-quark effects arise from a subtle interplay of quantum effects in QCD, it is no surprise that the listed nucleon models experience difficulties in quantifying them. Quite strikingly, most model predictions in Table 2.3 tend towards negative μ_s values, contrary to what is suggested by the PVES data. Moreover, some recent lattice QCD calculations do not resolve this discrepancy, yielding values of $\mu_s = -0.046 \pm 0.019$ [85] and $G_M^s(Q^2 = 0.23\ \text{GeV}^2) = -0.034 \pm 0.021$ [86].

Table 2.3: Predictions for the strangeness parameters r_s^2 and μ_s in various hadron-structure models.

Model	Ref.	$r_s^2(fm^2)$	$\mu_s(\mu_N)$
VMD	[81]	0.16	-0.31
$K\Lambda$	[82]	-0.007	-0.35
NJL	[83]	-0.17	-0.45
χQS(K)	[84]	-0.095	0.115

Axial form factors

Whereas the weak vector form factors can be pretty well determined by relating them to the electromagnetic ones through CVC, the situation for the axial form factors is much less clear. Yet, assuming pion-pole dominance for the pseudoscalar form factor, the partially conserved axial current hypothesis (PCAC) yields the relation

$$G_P(Q^2) = \frac{2m_N}{Q^2 + m_\pi^2} G_A(Q^2), \tag{2.38}$$

with m_π the pion mass. Besides, the contribution of G_P to the cross section is proportional to the scattered lepton's mass, and can be safely ignored for NC reactions. At $Q^2 = 0$, the form-factor values are given by

$$G_A = \begin{cases} \frac{-g_A\tau_3 + g_A^s}{2} & \text{NC} \\ g_A\tau_\pm & \text{CC} \end{cases} \tag{2.39}$$

where $g_A = 1.26$ is the axial coupling constant, as determined from neutron decay [54]. The Q^2 dependence of G_A is often parameterized in terms of a dipole

$$G_A(Q^2) = \frac{G_A(0)}{(1 + \frac{Q^2}{M_A^2})^2}. \tag{2.40}$$

The axial mass M_A can be extracted from neutrino QE scattering data. We adopt the value $M_A = 1.032$ GeV, in close agreement with the world-average values reported in Refs. [87, 88]. A recent analysis of QE (anti)neutrino total and differential cross sections for a variety of target nuclei resulted in the value [88]

$$M_A = 0.999 \pm 0.011. \tag{2.41}$$

Hereby, the authors employed the recent BBBA(07) vector form-factor parameterization [63] and a relativistic Fermi-gas (RFG) model. On the other hand, a value of

$M_A \approx 1$ GeV is not in line with the recent results of the high-statistics K2K [89] and MiniBooNE [43] experiments

$$M_A = \begin{cases} 1.20 \pm 0.12 & \text{K2K} \\ 1.25 \pm 0.12 & \text{MiniBooNE} \end{cases} \tag{2.42}$$

Both of these experiments performed their analysis with an RFG model. In the MiniBooNE case, an additional *Pauli-blocking* parameter κ is introduced, enabling a better description of the low-Q^2 data. The M_A value shown in Eq. (2.42) was extracted from a fit to the Q^2 shape beyond $Q^2 = 0.25$ GeV^2, where variations of κ have very little effect. The discrepancy between the axial-mass values in Eqs. (2.41) and (2.42) is one of the major topics to be addressed by future neutrino-scattering experiments.

Axial strangeness form factor

The experimental information on the axial strangeness parameter g_A^s emanates from polarized deep-inelastic scattering (DIS) experiments and neutrino-scattering data [90]. The former determine the strangeness contribution to the nucleon's spin, either directly in a semi-inclusive measurement (by flavor-tagging) [91, 92], or indirectly by measuring the quark flavor-summed structure function and assuming $SU(3)_f$ symmetry to access the strangeness contribution [93–95]. Unfortunately, both methods suffer from large uncertainties related to the extrapolation of the spin structure functions to vanishing Bjorken x [90]. Nevertheless, most results hint at a non-vanishing contribution of strange sea quarks to the nucleon spin, $-0.20 < \Delta s < 0$ [96, 97]. As an alternative, neutrino-nucleon scattering studies offer some advantages over the lepton DIS methods. Theoretical uncertainties are smaller and the sensitivity to $G_A(Q^2)$ is large. In fact, the strangeness contribution to the nucleon spin is related to the axial strangeness form factor by $\Delta s = G_A(Q^2 = 0) = g_A^s$. The BNL E734 experiment took data for the νp and $\overline{\nu} p$ elastic processes to extract a g_A^s value from the ratio of NC to CC cross sections [98]. Analyses of these data [99–101] have revealed large correlations of g_A^s with M_A and $G_{E,M}^s$. For example, varying M_A from 1.032 GeV to 1.086 GeV allows for fitted g_A^s values that range from -0.21 to 0 [99]. Note that both axial-mass values are still well within range of what is extracted from QE neutrino scattering data (see Eqs. (2.41) and (2.42)). The large experimental uncertainties of the E734 data led the authors of Ref. [101] to conclude that no new strangeness information can be extracted from this experiment alone. Therefore, some studies [70, 100] have combined the available PVES data with the neutrino BNL data to extract a value for G_E^s, G_M^s and G_A^s simultaneously. Assuming $M_A = 1.026$ GeV in Ref. [100], one finds $G_E^s = 0.02 \pm 0.09$, $G_M^s = 0.00 \pm 0.21$ and $G_A^s = -0.09 \pm 0.05$ at $Q^2 = 0.5$ GeV^2. More recently, strange vector and axial form factors were derived from a combined analysis of G0 and HAPPEX PVES data and neutrino BNL data [70],

in the range $0.45 < Q^2 < 1.0$ GeV^2. Their best fit involves a G_A^s that becomes negative with decreasing Q^2, hence supporting evidence for a negative Δs value. From this kind of studies, it has become evident that the most clear-cut way to pin down all strangeness form factors requires a combination of dedicated, high-statistics neutrino experiments and PVES experiments [90]. The axial strangeness form factor $G_A^s(Q^2)$ has also been the subject of theoretical studies [70]. As can be appreciated from Fig. 2.4, the strangeness form factors of the chiral quark-soliton model ($\chi QS(K)$) provide a fair description of the PVES and BNL data [84, 102–104].

2.4 Modeling nuclear effects

In Section 2.2, we have explained how the specific dynamics of the nucleon-knockout process makes the impulse approximation the preferred framework to compute QE cross sections in. When, in addition, the nuclear wave functions are constructed in an independent-particle model, it is possible to write the involved nuclear-current matrix elements in terms of the one-body expressions in Eq. (2.20). Under these *quasi-free* conditions, one adopts a one-body operator that is free from medium effects. Its form-factor parameterization was discussed in detail in Section 2.3.
The current section focuses on the inclusion of nuclear effects. First, we briefly outline the model that was used to compute the single-nucleon wave functions, and we derive an explicit expression for the bound-state spinors. The second part deals with our treatment of final-state interactions. Some basic features of the multiple-scattering Glauber approximation will be indicated, and an expression for the wave function of the outgoing nucleon is presented.

2.4.1 Relativistic bound-state wave functions

To describe the nuclear ground state, we turn to the relativistic, quantum field-theoretical framework developed by Walecka [105]. The well-known σ-ω model starts from the assumption that nucleons in nuclei interact by exchanging mesons of the scalar ($\sim \sigma$) and vector ($\sim \omega$) type. Replacing the meson field operators with their expectation values at high densities, a set of exactly-solvable mean-field equations can be distilled [105]. Efforts to extend the σ-ω Walecka model include the interaction with pions and ρ mesons, as well as the coupling to the photon field [106, 107]. Moreover, applying a relativistic Hartree approximation to derive the corresponding equations of motion, one arrives at a set of coupled field equations that carry the same content as Walecka's mean-field theory [107]. Imposing the condition that the nuclear ground state is spherically symmetric and a parity eigenstate, the general solutions of the Dirac equation can be written in a two-component representation

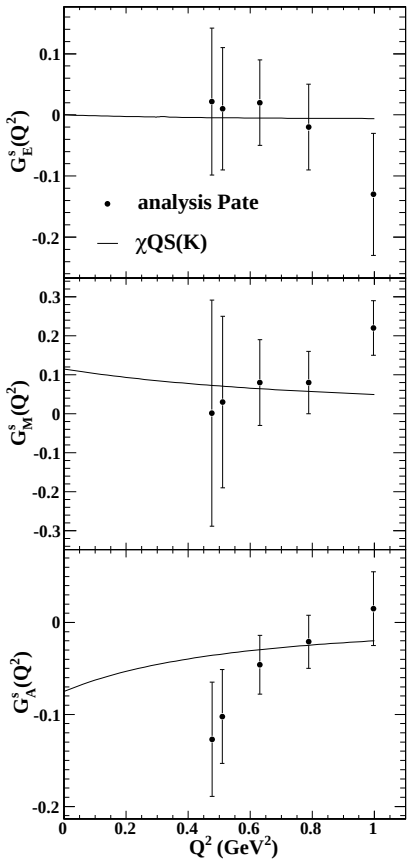

Figure 2.4: Comparison of a combined analysis of G0 and E734 data (closed circles) [70] with predictions from the chiral quark soliton model (full line) for the strangeness form factors G_E^s, G_M^s and G_A^s. Values for r_s^2 and μ_s are taken from Table 2.7, while $g_A^s = -0.075$ [104].

as

$$\Psi_{\alpha,m}(\vec{r}) = \begin{pmatrix} i\frac{G_\alpha(r)}{r}\mathscr{Y}_{+\kappa,m}(\hat{\vec{r}}) \\ -\frac{F_\alpha(r)}{r}\mathscr{Y}_{-\kappa,m}(\hat{\vec{r}}) \end{pmatrix}, \tag{2.43}$$

where m is the magnetic quantum number and α stands for all other quantum numbers that specify a single-particle orbital. The functions G_α and F_α denote the radial wave functions, which are computed using the $W1$ parameterization for the different field strengths [24]. This parameter set produces charge densities and average binding-energies per nucleon that compare well with the available data on spherically-symmetric nuclei [24, 80]. Furthermore, in the definition of the spherical two-spinors, we have introduced a generalized angular momentum, defined as $|\kappa| = j + 1/2$.

When considering neutrino-nucleus scattering processes, the relativistic bound-state wave functions in Eq. (2.43) are to be used in the one-body current expression of Eq. (2.20). From a computational point of view, however, it is more rewarding to consider the hadronic current in momentum space. So, alternatively, we write

$$\left\langle J^{\mu(QE)} \right\rangle = \overline{u}(k_f, s_f)\hat{J}^\mu \mathscr{U}_{\alpha,m}(\vec{p}), \tag{2.44}$$

where the free Dirac spinor $u(k_f, s_f)$ represents the outgoing nucleon. The bound-state spinor $\mathscr{U}_{\alpha,m}(\vec{p})$ can be calculated as the Fourier transform of the bound-state wave functions in Eq. (2.43)

$$\mathscr{U}_{\alpha,m}(\vec{p}) = \frac{1}{(2\pi)^{3/2}} \int \Psi_{\alpha,m}(\vec{r}) e^{-i\vec{p}\cdot\vec{r}} d\vec{r}. \tag{2.45}$$

The result is

$$\mathscr{U}_{\alpha,m}(\vec{p}) = i^{(1-l)} \sqrt{\frac{2}{\pi}} \frac{1}{p} \begin{pmatrix} g_\alpha(p)\mathscr{Y}_{+\kappa,m}(\hat{\vec{p}}) \\ -f_\alpha(p)\mathscr{Y}_{-\kappa,m}(\hat{\vec{p}}) \end{pmatrix}, \tag{2.46}$$

with

$$g_\alpha(p) = \int_0^\infty G_\alpha(r)\hat{j}_l(pr)dr, \tag{2.47}$$

and

$$f_\alpha(p) = \mathrm{sgn}(\kappa) \int_0^\infty F_\alpha(r)\hat{j}_{\overline{l}}(pr)dr, \quad \overline{l} = \begin{pmatrix} l+1, & \kappa < 0 \\ l-1, & \kappa > 0 \end{pmatrix}. \tag{2.48}$$

In (2.47) and (2.48), $\hat{j}_l(x) = x\, j_l(x)$ are the Ricatti-Bessel functions. With the hadronic current in Eq. (2.44), we can derive an explicit expression for the hadronic tensor in the impulse approximation

$$H^{\mu\nu}_{(QE)} = \frac{1}{2j+1} \overline{\sum}_{m;s_f} \langle J^{\mu(QE)} \rangle^\dagger \langle J^{\nu(QE)} \rangle. \tag{2.49}$$

Considering nucleon knockout from a specific shell, one can average over the number of bound nucleons in that shell. When computing unpolarized cross sections, one can sum over the spin s_f of the outgoing nucleons. After some straightforward manipulations, we find

$$H^{\mu\nu}_{(QE)} = \frac{1}{2m_N}\mathrm{Tr}\left(S_\alpha \tilde{\mathcal{O}}^\mu (\not{k}_N + m_N)\mathcal{O}^\nu\right), \tag{2.50}$$

where $\mathcal{O}^\mu = \hat{J}^\mu$ and $\tilde{\mathcal{O}}^\mu = \gamma_0(\mathcal{O}^\mu)^\dagger\gamma_0$. In Eq. (2.50), we have introduced the short notation

$$S_\alpha(\vec{p}) = \frac{1}{2j+1}\sum_m \mathcal{U}_{\alpha,m}(\vec{p})\overline{\mathcal{U}}_{\alpha,m}(\vec{p}). \tag{2.51}$$

This expression, referred to as the bound-state propagator, can be cast in a form which is similar to the free-nucleon projection operator [108]. Indeed, one finds

$$S_\alpha(\vec{p}) = (\not{k}_\alpha + M_\alpha), \tag{2.52}$$

with the definitions

$$\begin{aligned} M_\alpha &= \frac{1}{(2\pi)^3}\frac{\pi}{p^2}\left(g^2_\alpha(p) - f^2_\alpha(p)\right), \\ E_\alpha &= \frac{1}{(2\pi)^3}\frac{\pi}{p^2}\left(g^2_\alpha(p) + f^2_\alpha(p)\right), \\ \vec{k}_\alpha &= \frac{1}{(2\pi)^3}\frac{\pi}{p^2}\left(2g_\alpha(p)f_\alpha(p)\hat{\vec{p}}\right). \end{aligned} \tag{2.53}$$

It goes without saying that the algebraic tric in Eq. (2.52) provides an elegant solution for the numerical implementation of the QE process. What is more, working in spinor notation has yielded the compact *trace* expression of Eq. (2.50), in contrast to the more cumbersome integral expression of Eq. (2.20). Figure 2.5 shows the momentum wave functions for a proton belonging to a specified carbon shell. Owing to the small contribution of the lower wave-function component, the quantities M_α and E_α are almost equal.

2.4.2 Final-state interactions

In the previous section, we have set forth a realistic description of the nuclear ground-state in terms of the relativistic bound-state wave functions in Eq. (2.43). As a next step, the scattering wave function $\phi_F(\vec{r})$ figuring in Eq. (2.20) needs to be modeled to account for the final-state interactions (FSI) undergone by the ejectile. At this point, it is worth repeating that the QE strength is dominated by *direct* one-nucleon knockout processes. Hence, the detected nucleon comes straight from the vertex and carries all

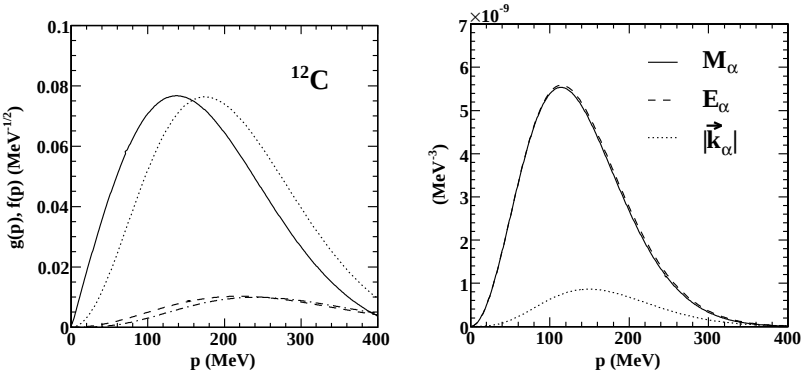

Figure 2.5: The left panel shows the momentum wave functions for the carbon nucleus. The full (dashed) line corresponds to $g(p)$ ($f(p)$) for a $1s_{1/2}$ proton, the dotted (dash-dotted) line represents $g(p)$ ($f(p)$) for a $1p_{3/2}$ proton. In the right panel, the quantities defined in Eq. (2.53) are shown for a $1p_{3/2}$-shell ^{12}C proton.

the information about the elementary weak-boson couplings, such as the axial form factor $G_A(Q^2)$. A prerequisite to disentangle this information, however, is the ability to compute the attenuation of the ejectile's wave function due to FSI mechanisms. The relativistic multiple-scattering Glauber approximation (RMSGA) provides such a framework. As a matter of fact, under some specific conditions explained below, the RMSGA allows to determine the exact number of nucleons that exit the residual system undisturbed.

The Glauber model is a multiple-scattering extension of the eikonal approximation [36]. As such, it describes the emission of a *fast* nucleon from a composite system of $A-1$ temporarily *frozen* nucleons, acting as scattering centers. The framework is valid under circumstances where the de Broglie wavelength λ of the ejectile satisfies $\lambda < r_s < R$, with r_s the typical interaction range between the energetic particle and the spectator nucleons, and R the range of the medium. Assuming $r_s \sim 1$ fm, the Glauber approach is believed to be valid down to $T_N \approx 300$ MeV. A detailed formulation of the RMSGA can be found in Ref. [37]. In this approach, the relativistic scattering wave function adopts the form

$$\phi_F(\vec{r}) = \mathcal{G}(\vec{b}, z)\ \phi_{k_N, s_N}(\vec{r}), \tag{2.54}$$

where ϕ_{k_N,s_N} is a relativistic plane wave and $\mathcal{G}(\vec{b},z)$ represents the scalar Dirac-Glauber phase, which accounts for the impact of FSI mechanisms on the scattering wave function. Postulating linear trajectories so that every point scatterer in the for-

ward path of the outgoing nucleon adds a phase to its wave function, one gets

$$\mathcal{G}(\vec{b},z)=\prod_{\alpha\neq B}\left[1-\int d\vec{r}\,'|\phi_\alpha(\vec{r}\,')|^2\theta(z'-z)\Gamma(\vec{b}'-\vec{b})\right], \tag{2.55}$$

where the product over α extends over all occupied single-particle states in the target nucleus, excluding the one from which the nucleon is ejected. The $\vec{r}\,'(\vec{b}',z')$ are the coordinates of the residual nucleons and $\vec{r}(\vec{b},z)$ specifies the interaction point with the weak vector boson. In Eq. (2.55), the z axis lies along the path of the ejected nucleon, and $\vec{b}$ is perpendicular to this path. Reflecting the diffractive nature of the nucleon-nucleon collisions at intermediate energies, the profile function is parameterized as

$$\Gamma(\vec{b})=\frac{\sigma_{NN}^{tot}(1-i\epsilon_{NN})}{4\pi\beta_{NN}^2}\exp\left(\frac{-b^2}{2\beta_{NN}^2}\right). \tag{2.56}$$

The parameters σ_{NN}^{tot} (total cross section), β_{NN} (slope parameter) and ϵ_{NN} (ratio of the real and imaginary part of the scattering amplitude) depend on the ejectile's energy. They are obtained through interpolation of the pp and pn data available from the Particle Data Group data base [53, 109]. In the limit of vanishing FSI, $\mathcal{G}(\vec{b},z)$ is put equal to 1, which corresponds to the relativistic plane-wave impulse approximation (RPWIA).

2.5 Cross-section results

To study QE cross sections and their sensitivities to model parameters and assumptions, we have implemented the formalism presented above into a computer code. Baseline results are derived in the RPWIA, using the $cc2$ form of Eq. (2.26) for the one-body current operator. As standard input for the form factors, we take the dipole parameterizations of Eqs. (2.30), (2.32) and (2.40) with the values $M_V = 843$ MeV, $M_A = 1032$ MeV and $g_A = 1.262$. For the time being, we put $G_E^s = G_M^s = G_A^s = 0$. A discussion of the nucleon's strangeness content in relation to QE cross sections is postponed to Section 2.7. Parameters used in the computations of BSWF and Glauber phases are kept fixed throughout this work.

2.5.1 Inclusive eA scattering

An important test for any nuclear model is the comparison with inclusive electron-nucleus scattering data. Indeed, putting our model to the test by contrasting its predictions with inclusive QE data can yield valuable information about the reaction mechanisms that are at work in this energy region. In inclusive processes, only the outgoing lepton is observed. Recognizing that the Glauber approach takes away all

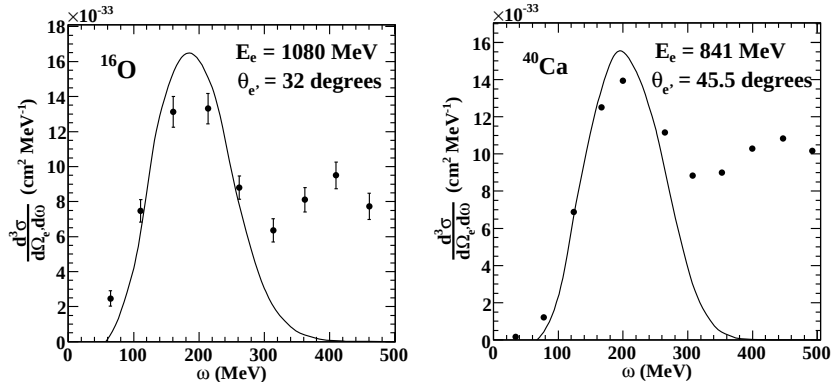

Figure 2.6: RPWIA cross sections for the process $e^- + A \rightarrow e^- + X$, at specified incoming-electron energies E_e and electron scattering angles $\theta_{e'}$. In the left (right) panel, data are taken from Ref. [110] ([111]). At the peak, $Q^2 = 0.295$ GeV^2 ($= 0.316$ GeV^2) in the left (right) panel. For the reader's convenience: 10^{-33} cm^2 = 1nbarn.

strength due to inelastic scatterings of the outgoing nucleon, we choose to neglect FSI effects in order to retain all possible nucleon-knockout contributions to the inclusive *eA* data. In Figs. 2.6, 2.7 and 2.8, we present RPWIA cross sections for electron-induced one-nucleon knockout from different target nuclei.

As can be appreciated from these results, the RPWIA computations succeed well in describing the QE peak region. At the peak, they mostly overestimate the strength, whereas, towards lower energy transfers, they fall short in fully explaining the data. The good agreement, both in size and shape, between our calculations and the electron data provides sound evidence that single-nucleon knockout is the dominant mechanism in this energy region. In Fig. 2.7, we compare the RPWIA results computed within our model to the ones obtained in a simple RFG model. The latter sees the nucleus as a collection of nucleons, belonging to a Fermi sea with Fermi momentum k_F. Thus, each nucleon has an energy $E = (k^2 + M_N^2)^{1/2} - E_b$, where $k < k_F$ and E_b is a binding-energy correction which is put in by hand. Despite its naiveness, the RFG model reproduces the QE peak reasonably well. Indeed, the data are not extremely sensitive to the nucleon momentum distribution. Compared to a more realistic treatment of the nucleus, however, there are some notable, qualitative differences. The peak strength predicted by the Fermi-gas model is slightly larger than the RPWIA one. Moreover, the latter gives a better account of the tails in the ω distribution.

The fact that both models underestimate the data for low energy transfers and in the dip region is to be understood as a failure of the impulse approximation itself. It is

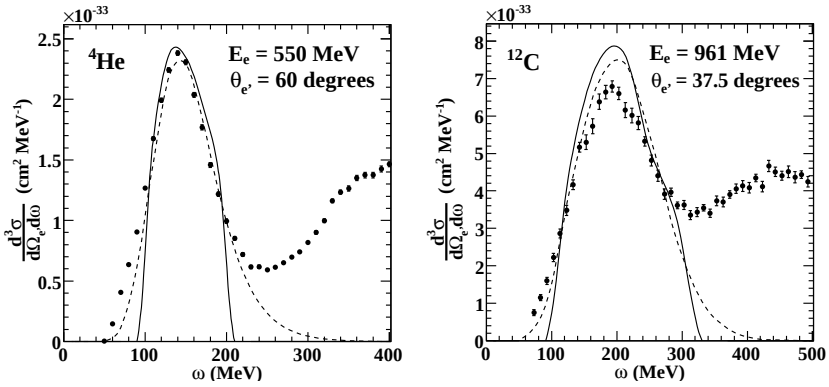

Figure 2.7: Comparison of RPWIA (dashed line) and RFG (full line) calculations for the process $e^- + A \to e^- + X$. For the helium (carbon) nucleus, $k_F = 169$ MeV and $E_b = 17$ MeV ($k_F = 221$ MeV and $E_b = 25$ MeV) are chosen. Helium data are taken from Ref. [112], carbon data from Ref. [113]. At the peak, $Q^2 = 0.226$ GeV^2 ($= 0.310$ GeV^2) in the left (right) panel.

well-known, for example, that the dip region is prone to two-body kinematics [48]. A description in terms of meson-exchange and isobar currents is mandatory in this energy region. The inclusion of short-range nucleon-nucleon correlations in our nuclear model could also improve the agreement with data [114, 115]. Multi-nucleon processes also play a non-negligible role in the low-ω region of the QE peak and for small momentum transfers. In Ref. [23], a growing disagreement between IA calculations and electron-scattering data is observed for decreasing Q^2, leading the authors to the conclusion that the IA can only be justified for momentum transfers $|\vec{q}\,| \gtrsim 400$ MeV. In QE kinematics, $\omega \sim |\vec{q}|^2/2m_N$, this translates in the breakdown of the IA at $Q^2 \sim 0.15$ GeV^2. Scanning the nucleus with lower spatial resolution makes the contributions from collective, multi-nucleon excitations more important. In this region of the $(\omega, |\vec{q}\,|)$ plane, the inclusion of long-range random-phase approximation (RPA) corrections becomes indispensable. Figure 2.8 illustrates the breaking down of the IA by comparing predictions that differ only in the direction of the observed electron. The Q^2 values at the peak position are 0.1 GeV^2 and 0.224 GeV^2 for the left and right panel respectively. Clearly, the RPWIA calculations are in closer agreement with data in the latter case.

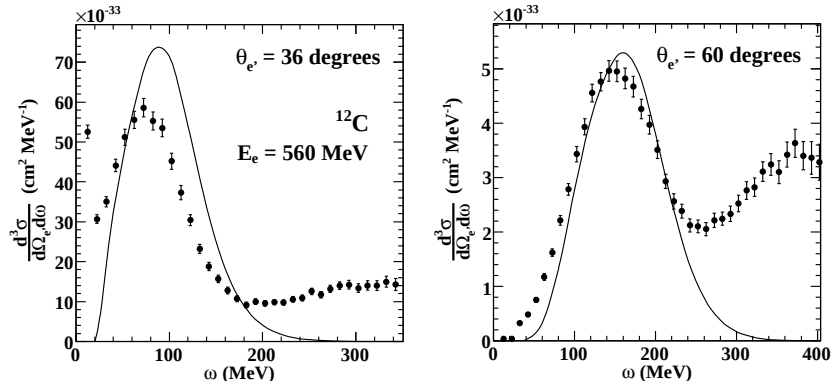

Figure 2.8: RPWIA results for $e^- + A \rightarrow e^- + X$ for scattering from a carbon target at $E_e = 560$ MeV and different scattering angles. Data taken from Ref. [116]. At the peak, $Q^2 = 0.1$ GeV^2 ($= 0.224$ GeV^2) in the left (right) panel.

2.5.2 Semi-inclusive observables and nuclear transparencies

When detecting an emitted nucleon in coincidence with the scattered lepton, the modeling of FSI mechanisms becomes essential when comparing with data. A frequently-used quantity to estimate the overall effect of FSI in nucleon-emission processes is the nuclear transparency: it provides a measure for the probability that a nucleon of a certain energy can escape from the nucleus without being subject to any further interactions. Experimentally, it is extracted from the ratio of the measured $A(e,e'p)$ yield to the calculated one using the PWIA, according to [117]

$$T_{exp}(Q^2) = \frac{\int_{\Delta^3 p_m} d\vec{p}_m \int_{\Delta E_m} dE_m Y_{exp}(\vec{p}_m, E_m, \vec{k}_N)}{c_A \int_{\Delta^3 p_m} d\vec{p}_m \int_{\Delta E_m} dE_m Y_{PWIA}(\vec{p}_m, E_m)}. \tag{2.57}$$

In Eq. (3.59), the quantities $\Delta^3 p_m$ and ΔE_m specify the phase-space volume in the missing momentum and energy. To guarantee that the electro-induced proton-emission process is predominantly quasi-elastic, one places the kinematics cuts $|\vec{p}_m| \leqslant 300$ MeV and $E_m \leqslant 80$ MeV in combination with the requirement that the Bjorken variable $x \approx 1$ [47, 117]. Furthermore, the factor c_A in the denominator of Eq. (3.59) has been introduced to correct in a phenomenological way for short-range mechanisms. It accounts for the fact that short-range correlations move a fraction of the single-particle strength to higher missing energies and momenta and, hence, beyond the ranges covered in the integrations of Eq. (3.59). In a similar way, theoretical predictions for the nuclear transparency can be obtained from the ratio of RMSGA calculations to RPWIA

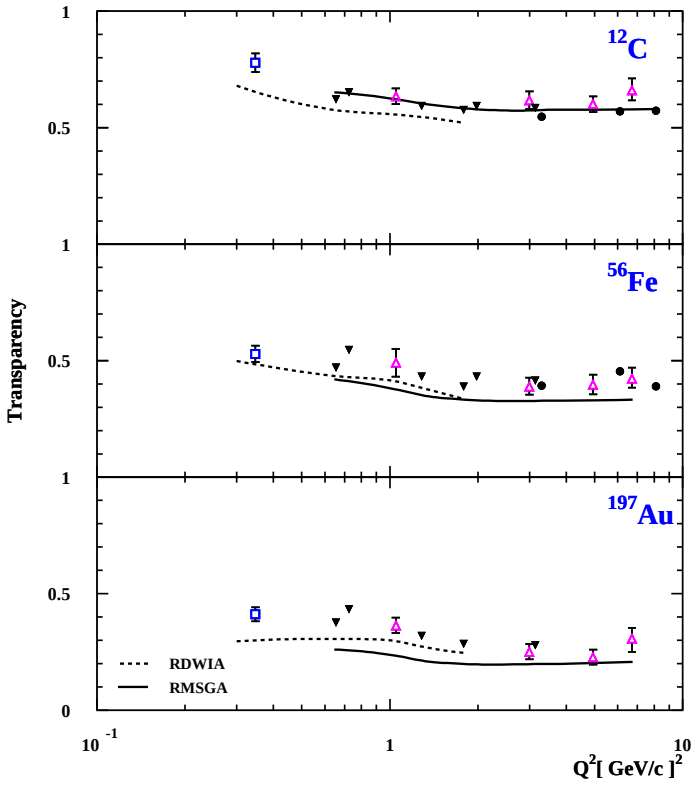

Figure 2.9: Nuclear transparencies versus Q^2 for $A(e,e'p)$ reactions in quasi-elastic kinematics, as taken from Ref. [117]. RMSGA (full line) and RDWIA (dashed line) calculations are compared to $A(e,e'p)$ data.

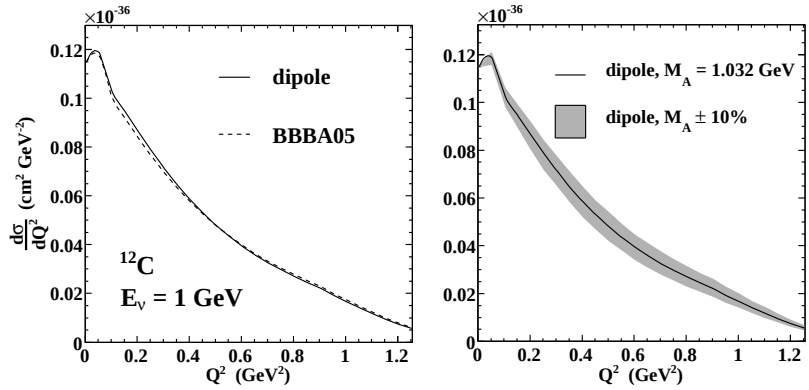

Figure 2.10: RPWIA cross sections for ^{12}C(ν_μ, μ^-) and an incoming energy of 1 GeV. In the left panel, the full (dashed) line corresponds to the dipole (BBBA05) parameterization for the vector form factors. The shaded region in the right panel corresponds to a 10% variation in the axial mass.

ones. Figure 2.9 displays the transparencies computed within the RMSGA and RDWIA models as a function of Q^2, together with the world data. Here, the ^{197}Au data are compared to ^{208}Pb calculations, and c_A values of 0.9 (^{12}C), 0.82 (^{56}Fe) and 0.77 (^{208}Pb) are adopted [117]. As can be appreciated from Fig. 2.9, apart from some tendency to underestimate the data for heavier nuclei, the RMSGA predicts the measured $A(e,e'p)$ transparencies well. In addition, in Ref. [19], it has been shown that the neutrino transparencies computed from $A(\nu,\nu'p)$ reactions agree quite well with their electron counterparts. It is therefore suggested that one could use RPWIA results to predict the *elastic* single-nucleon knockout contribution to inclusive neutrino cross sections by rescaling them with a transparency factor extracted from $A(e,e'p)$ data.

2.5.3 QE neutrino-nucleus cross sections

Reaching a satisfying level of agreement with both inclusive and semi-inclusive electron scattering data lends confidence that our QE nucleon-knockout framework will suit neutrino applications as well. Accordingly, in the Figs. 2.10 to 2.13, we present QE neutrino-nucleus cross sections for different incoming neutrino energies and a choice of representative target nuclei employed by current and planned neutrino experiments.

Figure 2.10 explores the sensitivity of CC νA cross sections to uncertainties in the form factors. It appears that ambiguities related to different vector form-factor parameterizations are well under control. For typical $Q^2 \lesssim 1$ GeV^2 in QE reactions,

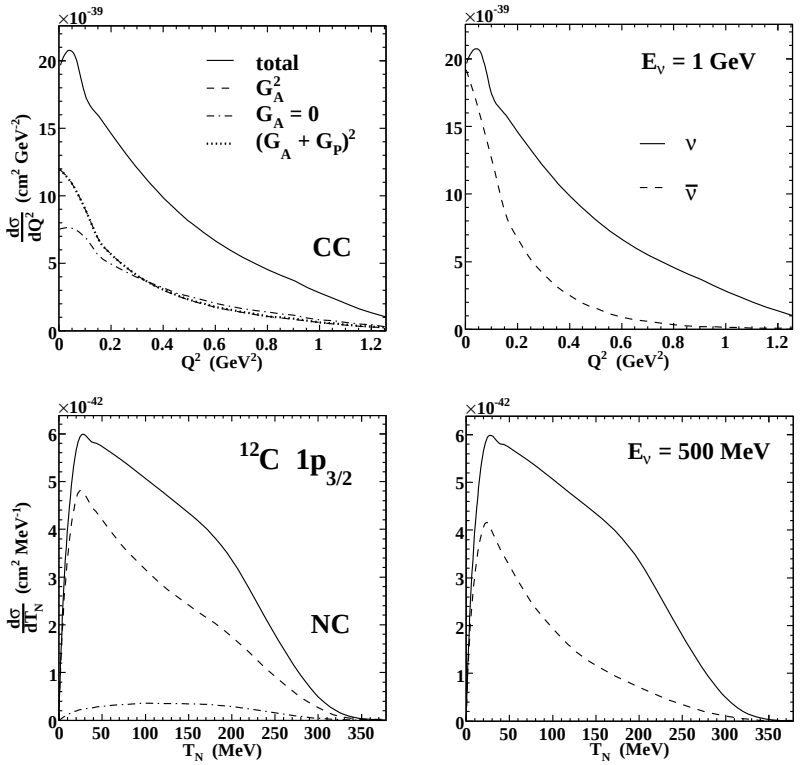

Figure 2.11: Study of vector and axial-vector form-factor contributions to the RPWIA cross sections for the knockout of a $1p_{3/2}$ proton from carbon. The upper (lower) panels show CC (NC) distributions against Q^2 (the ejectile's kinetic energy T_N) for $E_{\nu_\mu} = 1$ GeV (500 MeV). In the right-hand panels, neutrino- and antineutrino-induced cross sections are compared.

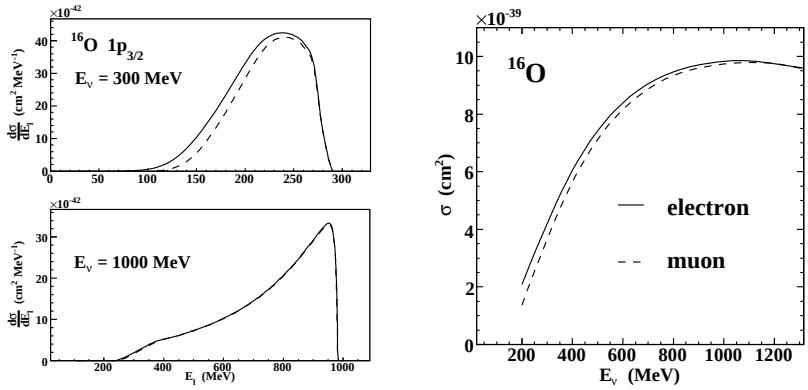

Figure 2.12: Comparison of electron- (full line) and muon-neutrino (dashed line) CC QE cross sections. The left panels display RPWIA predictions for the knockout of a $1p_{3/2}$ proton from an oxygen nucleus as a function of the outgoing lepton energy. The right panel compares total cross sections for an oxygen target.

the BBBA05 parameterization yields no appreciable differences with respect to the standard dipole one. As a consequence, the vector part in the one-body current of Eq. (2.26) appears solid and well-tested against electron data. To the contrary, the axial sector remains largely unknown, as the axial mass M_A needs to be extracted from neutrino-scattering data. The effect of the uncertainty on M_A is assessed in Fig. 2.10. Clearly, increasing (decreasing) its value by 10% leads to an increase (decrease) of the CC νA cross section by about the same amount.

Figure 2.11 displays NC and CC cross sections together with the separate contributions they receive from vector and axial-vector form factors. The pseudoscalar form factor G_P gives rise to terms that are proportional to the outgoing lepton's mass and, hence, does not enter into the NC cross-section result. Nor does it play a role in the CC case, as can be appreciated by comparing the axial contributions there. For NC cross sections, the term proportional to G_A^2 accounts for the bulk of the total strength. Suppressed by the weak mixing angle, the F_1 and F_2 contributions to the NC responses are small. On the other hand, the CC cross sections receive comparable shares from the vector and axial terms. In both cases, the remainder of the strength is mainly due to the interference contribution $G_A F_2$ [19], which dominates the transverse response function R'_T in Eq. (2.15). Thus, a difference of $\sim 2G_A F_2$ is what distinguishes the neutrino- and antineutrino-induced cross sections in Fig. 2.11.

All neutrino results presented so far relate to ν_μ (or $\overline{\nu}_\mu$) scattering. As the majority of neutrino experiments is based on neutrino beams from pion decays, muon neutrinos are indeed the most frequently-used ones. Of course, the produced muon neutrinos

undergo flavor oscillations, provoking a certain number of ν_e events in the far detectors. Recently, it has been shown [118] that uncertainties related to the ratio of ν_e to ν_μ QE cross sections have a non-negligible impact on the sensitivity of future superbeam facilities to measuring CP violation. Figure 2.12 compares RPWIA cross sections for ν_μ and ν_e probes as a function of the incoming neutrino energy. At low energies, it is seen how the larger phase space available for producing electrons results in larger cross sections for electron neutrinos. As the incoming neutrino energy approaches 1 GeV, however, this effect soon dwindles to a mere 1% level. For energies beyond 1 GeV, no appreciable differences can be observed between the RPWIA cross sections induced by ν_μ and ν_e.

In Fig. 2.13, we study the effect of FSI on QE nucleon-knockout cross sections. To this end, two types of calculations are presented. First, we have computed cross sections within the RMSGA framework, where the ejectile's FSI are incorporated in an unfactorized way. As a second approach, we have estimated the effect of FSI mechanisms by scaling the RPWIA cross sections with a constant factor that is taken as a representative value for the $A(e,e'p)$ transparency. Correcting the measured transparencies from Fig. 2.9 with the factor c_A, we take $T = 0.52$ ($= 0.34$) for ^{12}C (^{56}Fe). In the region where the RMSGA produces reliable results, i.e. for $T_p > 200$ MeV [19], a good to very good agreement is observed between the rescaled RPWIA and the fully unfactorized RMSGA results. Again, this finding supports the idea that a simple scaling of the RPWIA results allows one to reliably estimate the FSI effects for the QE contribution to the inclusive neutrino cross section. It is important to stress, however, that a cut in E_m is needed in order to isolate this elastic nucleon-knockout channel.

2.6 Paschos-Wolfenstein relation in a hadronic picture

Lately, neutrinos have been regarded as interesting candidates for electroweak tests aiming at a precision measurement of the Weinberg angle θ_W [119–121]. One of the most fundamental parameters in the Standard Model (SM), the weak mixing angle has been at the center of research activities, involving both theoretical SM calculations [122, 123] and experimental efforts to determine its value. While all $\sin^2\theta_W$ measurements near the Z^0 pole [124, 125] and for low Q^2 values [126, 127] are in good agreement with the SM prediction, an experiment by the NuTeV collaboration at $Q^2 = 20$ GeV^2 does not seem to corroborate the calculated running of the Weinberg angle [119]. Indeed, the NuTeV result $\sin^2\theta_W = 0.22773 \pm 0.00135$ (stat) ± 0.00093 (syst) lies 3σ above the standard model prediction of 0.2227 ± 0.0004. Explanations for this anomalous result range from quantum chromodynamics (QCD) uncertainties [128, 129], to nuclear effects [130, 131] and even interpretations involving new physics [132, 133]. Whether the surprising NuTeV outcome can be resolved through a further analysis of the data or indeed hints at new physics beyond the SM, is up to this day an unresolved issue [134].

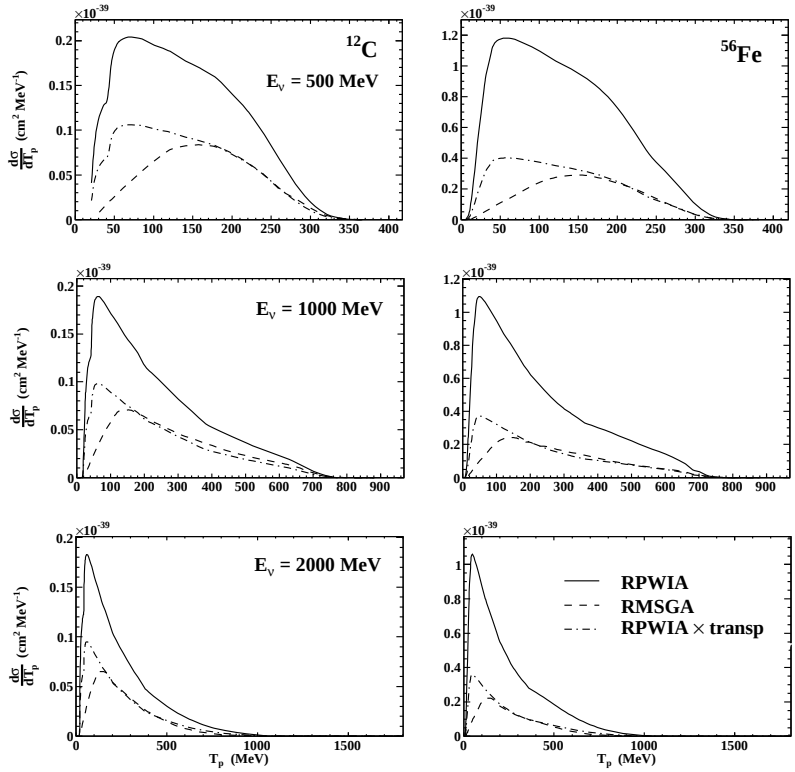

Figure 2.13: CC ^{12}C(ν_μ, μ^-) (left panels) and ^{56}Fe(ν_μ, μ^-) (right panels) cross sections as a function of the outgoing proton's kinetic energy at different incoming energies. The dashed (full) lines represent the unfactorized RMSGA (RPWIA) calculations. The dash-dotted lines show the RPWIA results, scaled with a transparency factor $T(^{12}\mathrm{C}) = 0.52$ and $T(^{56}\mathrm{Fe}) = 0.34$.

In NuTeV's analysis, the Paschos-Wolfenstein (PW) relation [135] plays an essential role in relating the weak mixing angle to measured ratios of NC to CC deep-inelastic scattering neutrino cross sections. This relation is traditionally defined as the following ratio of NC to CC (anti)neutrino-nucleon cross sections

$$\mathrm{PW} = \frac{\sigma^{\mathrm{NC}}(\nu N) - \sigma^{\mathrm{NC}}(\overline{\nu} N)}{\sigma^{\mathrm{CC}}(\nu N) - \sigma^{\mathrm{CC}}(\overline{\nu} N)}. \tag{2.58}$$

Adopting the nucleon's quark-parton structure, the PW relation can be computed starting from the quark currents

$$\begin{aligned} \hat{j}_\mu^{(Z)} &= \sum_{q=u,d} g_{q,L}\overline{q}\gamma_\mu(1-\gamma_5)q + g_{q,R}\overline{q}\gamma_\mu(1+\gamma_5)q \quad \text{NC}, \\ \hat{j}_\mu^{(+)} &= \frac{1}{2}\overline{u}\gamma_\mu(1-\gamma_5)d, \quad \hat{j}_\mu^{(-)} = \frac{1}{2}\overline{d}\gamma_\mu(1-\gamma_5)u \quad \text{CC}, \end{aligned} \tag{2.59}$$

with the quark coupling strengths

$$\begin{aligned} g_{u,L} &= \frac{1}{2} - \frac{2}{3}\sin^2\theta_W, \quad g_{u,R} = -\frac{2}{3}\sin^2\theta_W, \\ g_{d,L} &= -\frac{1}{2} + \frac{1}{3}\sin^2\theta_W, \quad g_{d,R} = \frac{1}{3}\sin^2\theta_W. \end{aligned} \tag{2.60}$$

Using these expressions, one immediately derives [136]

$$\mathrm{PW} = \left(\frac{1}{\cos^2\theta_c}\right)\left(\frac{1}{2} - \sin^2\theta_W\right). \tag{2.61}$$

Equation (2.61) is valid for isoscalar targets, containing an equal number of u and d quarks, and neglecting the role of s quarks.

Although the PW relation has been tested very well in the DIS regime with respect to genuine QCD mechanisms, little effort has been put in the intermediate-energy regime, where an adequate description in terms of hadronic rather than partonic degrees of freedom is needed. Therefore, in this section, we will explore what physics could be probed by future measurements of the Paschos-Wolfenstein relation at medium energies. Adopting our model for neutrino-induced nucleon knockout, we conduct a study of the PW relation in the QE regime [137], assessing its sensitivity to various model parameters and model dependencies. Knowing at what level nuclear uncertainties affect the PW relation, one can put theoretical constraints on the accuracy with which variables can be determined from it. In earlier work by Donnelly and Musolf [138], for example, nuclear uncertainties were estimated too large to allow a $\sin^2\theta_W$ determination in parity-violating electron scattering (PVES) with a precision similar to other types of measurements. With the advent of high-precision neutrino-scattering experiments such as MINERνA [139, 140], it is important to check whether the PW relation at medium energies provides a powerful tool for a Weinberg-angle extraction.

2.6.1 Paschos-Wolfenstein relation in neutrino-nucleus scattering

The cross sections in Eq. (2.15) constitute the ingredients for our study of the PW relation with hadronic degrees of freedom:

$$\mathrm{PW} = \frac{\sigma^{NC}(\nu A) - \sigma^{NC}(\overline{\nu} A)}{\sigma^{CC}(\nu A) - \sigma^{CC}(\overline{\nu} A)}. \tag{2.62}$$

A numerical calculation of the PW relation according to Eq. (2.62) allows to investigate the deviations from the prediction in Eq. (2.61) and to estimate the role of nuclear effects. Before doing so, however, it is interesting to investigate whether the $\sin^2\theta_W$ dependence of Eq. (2.61) can be retrieved within a hadronic picture. First, integrating over all angles Ω_l, Ω_N in Eq. (2.15) nullifies the ϕ-dependent terms. Moreover, ignoring the small differences between proton and neutron wave functions when evaluating the difference of ν- and $\overline{\nu}$-induced cross sections, we retain only the contribution from the transverse R'_T response. Obviously, for NC processes, this contribution has to be considered for protons and neutrons separately, whereas in the denominator, the charge-exchange feature of the interaction forces neutrinos to interact with neutrons and antineutrinos with protons. Expressing the differential cross sections in terms of the outgoing nucleon's kinetic energy T_N, we obtain for an isoscalar nucleus

$$\frac{\frac{d\sigma^{NC}(\nu A)}{dT_N} - \frac{d\sigma^{NC}(\overline{\nu} A)}{dT_N}}{\frac{d\sigma^{CC}(\nu A)}{dT_N} - \frac{d\sigma^{CC}(\overline{\nu} A)}{dT_N}} \approx \left(\frac{1}{\cos^2\theta_c}\right) \times \frac{\sum_{\tau_3=\pm1}\sum_\alpha \int_0^\pi \sin\theta_l \sin^2\frac{\theta_l}{2} d\theta_l \int_0^\pi \sin\theta_N d\theta_N \; k_N \; f_{rec}^{-1} \; \frac{dT_N}{dE_l} \; \frac{E_l^2 M_Z^4}{(4E_\nu E_l \sin^2\frac{\theta_l}{2} + M_Z^2)^2} \; \frac{E_\nu + E_l}{q} (R'_T)^{NC}}{\sum_\alpha \int_0^\pi \sin\theta_l \sin^2\frac{\theta_l}{2} d\theta_l \int_0^\pi \sin\theta_N d\theta_N \; k_N \; f_{rec}^{-1} \; \frac{dT_N}{dE_l} \; \frac{E_l^2 M_W^4}{(4E_\nu E_l \sin^2\frac{\theta_l}{2} + M_W^2)^2} \; \frac{E_\nu + E_l}{q} (R'_T)^{CC}}, \tag{2.63}$$

where the summation over α extends over all bound proton single-particle levels in the target nucleus. Furthermore, the mass of the outgoing lepton has been neglected in Eq. (2.63). Clearly, the main difference between numerator and denominator lies in the value of the remaining transverse response function R'_T, which is proportional to $G_A(Q^2)G_M(Q^2)$. Assuming that $Q^2 \ll M_Z^2, M_W^2$ and disregarding differences in the contributions of different shells, the expressions in numerator and denominator can-

cel to a large extent. In other words, the PW relation is approximately given by

$$\frac{\frac{d\sigma^{NC}(\nu A)}{dT_N} - \frac{d\sigma^{NC}(\overline{\nu} A)}{dT_N}}{\frac{d\sigma^{CC}(\nu A)}{dT_N} - \frac{d\sigma^{CC}(\overline{\nu} A)}{dT_N}} \approx \left(\frac{1}{\cos^2\theta_c}\right) \frac{\sum_{\tau_3=\pm 1} G_A^{NC}(0) G_M^{NC}(0)}{G_A^{CC}(0) G_M^{CC}(0)}$$
$$= \left(\frac{1}{\cos^2\theta_c}\right)\left((\frac{1}{2} - \sin^2\theta_W) + \frac{g_A^s}{g_A}\left(\frac{\sin^2\theta_W(\mu_p+\mu_n)+\frac{1}{2}\mu_s}{(\mu_p-\mu_n)}\right)\right). \tag{2.64}$$

Apart from the standard value figuring in Eq. (2.61), an additional strangeness term appears. In (2.64), $\mu_p = F_{2,p}^{EM}(0)$ ($\mu_n = F_{2,n}^{EM}(0)$) denotes the proton (neutron) magnetic moment and $\mu_s = F_2^s(0)$ is the strangeness magnetic moment. We wish to stress that the left-hand side of Eq. (2.64) is T_N independent.

2.6.2 Results and discussion

In the analytic derivation described above, the DIS expression of the PW relation was regained by making various approximations to our hadronic picture. Next, we will evaluate numerically to what extent the nuclear medium affects this *standard value* of the PW relation. To this end, the nuclear effects are gradually included and the resulting PW curves are compared with the expression (2.64). In a first series of calculations, we neglect the strangeness content of the nucleon, putting $g_A^s = 0$ and $\mu_s = 0$. A discussion of the strangeness sensitivity of the PW relation is postponed to the end of this section. Results will be presented for ν_e ($\overline{\nu}_e$) scattering off both an isoscalar nucleus, $^{16}_{8}$O, and a heavier one, $^{56}_{26}$Fe, with neutron excess. For sufficiently high neutrino energies, $E_\nu \lesssim 1$ GeV, Fig. 2.12 indicates that our findings are applicable to muon-neutrino scattering as well. As a general starting point, we use dipole vector and axial form factors, the *cc2* form for the one-nucleon current and an on-shell weak mixing angle $\sin^2\theta_W = 0.2224$.

Relativistic plane-wave impulse approximation

Figure 2.14 displays the PW relation against the outgoing nucleon's kinetic energy T_N for an incoming neutrino energy of 1 GeV and an $^{16}_{8}$O target nucleus. Clearly, the $1p_{1/2}$-shell contribution to the PW relation can not be distinguished from the total, shell-summed expression. Both curves show a remarkably constant behavior over a broad T_N interval and are in excellent agreement with the analytic value in Eq. (2.64). For an incoming neutrino energy of 1 GeV, nuclear binding effects do not seem to influence the PW relation considerably. As can be appreciated from Fig. 2.14, Eq. (2.64) provides a very good approximation under those circumstances. In Fig. 2.15, we studied the sensitivity to the adopted parameterization for the electroweak form factors.

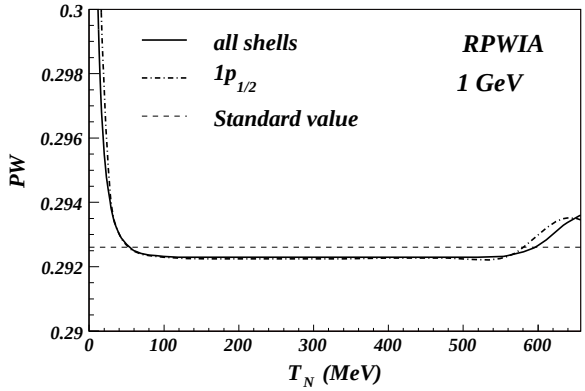

Figure 2.14: The RPWIA Paschos-Wolfenstein relation as a function of the outgoing nucleon's kinetic energy T_N for an incoming neutrino energy of 1 GeV and an ^{16}O target nucleus (full line). Also shown is the contribution of the $1p_{1/2}$ shell (dash-dotted). The dashed line represents Eq. (2.64), with $\sin^2\theta_W = 0.2224$ and $\cos\theta_c = 0.974$.

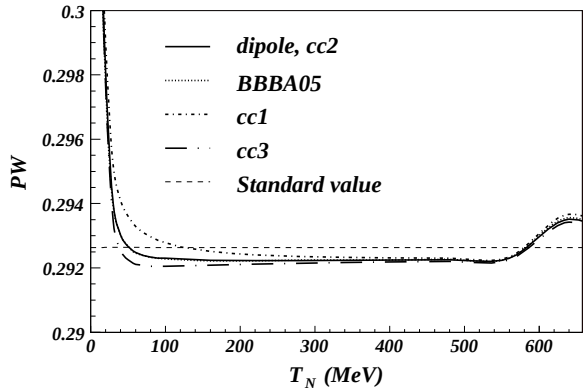

Figure 2.15: The RPWIA Paschos-Wolfenstein relation as a function of T_N for the ^{16}O $1p_{1/2}$ shell and an incoming neutrino energy of 1 GeV. The reference curve, with dipole vector form factors and the *cc2* prescription for the one-nucleon vertex function, is drawn as a full line. Using the BBBA05 parameterization results in the dotted curve. The (long) dash-dotted curve is obtained with the (*cc3*) *cc1* prescription. The dashed line represents the analytic value of Eq. (2.64).

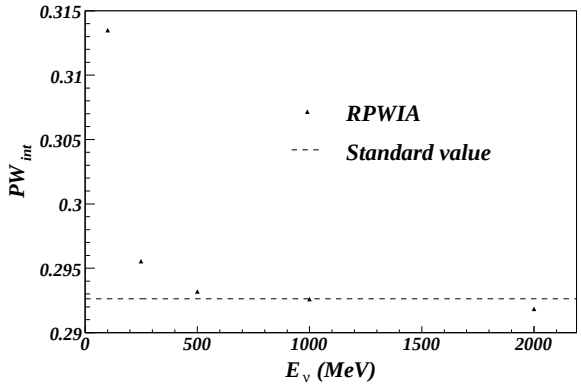

Figure 2.16: Paschos-Wolfenstein relation for total $\nu/\overline{\nu}-^{16}$O cross sections against incoming neutrino energy. The dashed line represents the standard value.

Employing the *updated* BBBA05 parameterization for the weak vector form factors apparently yields no difference with respect to the usual dipole form. Indeed, the fact that the results in Figs. 2.14 and 2.15 are relatively T_N independent indicates that the Q^2 dependence is largely cancelled out in the PW ratio. Accordingly, the sensitivity to the adopted Q^2 evolution of the form factors is minor. An interesting by-product of this feature is that the PW relation does not depend on the axial form factor's cut-off mass M_A, which constitutes a possible source of uncertainty in the determination of g_A^s from neutrino cross-section ratios [101, 141]. Similarly, Fig. 2.15 shows that the use of a different prescription for the weak one-nucleon current operator exercises only the smallest of influences on the PW relation.
Most neutrino experiments, however, do not possess the discriminative power to measure the ejectile's kinematics. In this case, a comparison with experimental results is facilitated by using total cross sections. Hence, it is useful to evaluate the integrated expression

$$\mathrm{PW}_{int} = \frac{\sigma^{NC}(\nu A) - \sigma^{NC}(\overline{\nu} A)}{\sigma^{CC}(\nu A) - \sigma^{CC}(\overline{\nu} A)}, \tag{2.65}$$

obtained by integrating $d\sigma/dT_N$ over T_N. Figure 2.16 displays PW_{int} for $\nu/\overline{\nu}$-^{16}O cross sections and various incoming neutrino energies ranging from 100 MeV to 2 GeV. From $E_\nu = 500$ MeV onwards, the calculated values agree with the standard value at the 0.5 percent level, illustrating once more the validity of the approximation of Eq. (2.64) in the RPWIA. However, large discrepancies are observed at lower incoming energies. There, binding effects play an important role in the relative magnitude of the individual shell contributions to the cross sections. As a result, the ex-

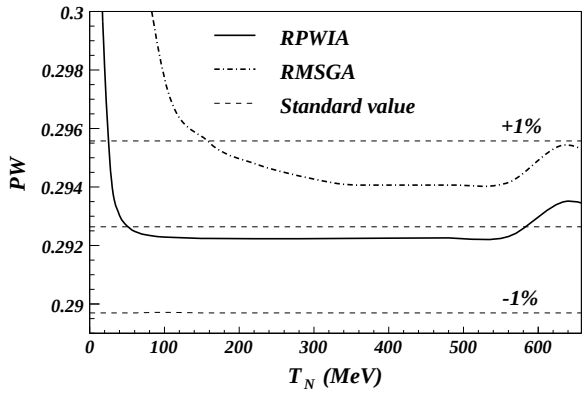

Figure 2.17: The Paschos-Wolfenstein relation as a function of T_N for the ^{16}O $1p_{1/2}$ shell. The full (dash-dotted) line shows the RPWIA (RMSGA) case. The dashed lines represent the standard PW value, with errors of 1%.

pressions in numerator and denominator of Eq. (2.63) do not cancel entirely, thereby shifting PW_{int} to larger values. With increasing incoming neutrino energies, differences between the contributions of different shells become of less importance and the numerically computed PW values take on the value for the free nucleon.

Final-state interactions

As a next step, we study the influence of FSI mechanisms on the PW relation. In the Glauber model, FSI roughly halve the cross sections for ^{16}O. Since the PW relation takes ratios of cross sections, FSI effects cancel to a large extent, which is shown in Fig. 2.17 for an incoming neutrino energy of 1 GeV. To better illustrate the influence of FSI mechanisms, a $\pm 1\%$ error on the standard PW value is shown. In the region where the RMSGA produces valid results, i.e. for $T_N \gtrsim 200$ MeV [19], FSI mechanisms increase the computed PW ratio by less than one percent.

Neutron excess

In the preceding discussion, the PW relation was investigated for a target with an equal number of protons and neutrons. Neutrino-scattering experiments often employ heavier target nuclei, with an excess amount of neutrons. The additional energy-dependent terms that are introduced in the PW formula will affect the predicted PW standard value (2.64), which required the perfect cancellation between proton and neutron contributions. Figure 2.18 shows the T_N dependence of the PW relation for

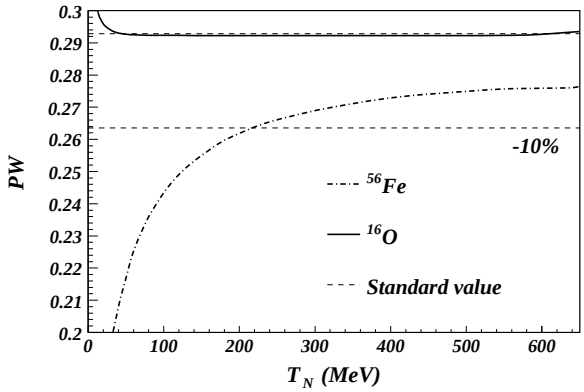

Figure 2.18: The RPWIA Paschos-Wolfenstein relation as a function of T_N for an iron target (dash-dotted). Other notations refer to Fig. 2.14. For reference purposes, a dashed-line denoting the 10%-reduced standard PW value is added.

^{56}Fe at an incoming neutrino energy of 1 GeV. The specific energy dependence of PW in the iron case is given shape by the extra ν-induced CC cross sections in the denominator. Thereby, low PW values correspond with the peak region and high values with the tail of the excess neutrons' contribution to $\sigma^{CC}(\nu A)$. In general, the neutron excess in the iron target lowers PW values by $\gtrsim 10\%$. Correspondingly, of all nuclear effects looked into here, the neutron-excess correction to the PW relation is the largest and most important one.

Model dependence and $\sin^2\theta_W$ determination

Of course, to be relevant for future neutrino-scattering experiments, the above predictions need to be discussed in terms of their model dependence. To this end, we follow the line of reasoning in Refs. [18, 141], where the difference between cross sections provided by a relativistic Fermi-gas model (RFG) and a relativistic shell model (RSM) is assumed to represent a reasonable measure for the theoretical model uncertainty itself. While sizeable for separate cross sections at lower incoming neutrino energies, nuclear-model dependences already seem to vanish at $E_\nu = 1$ GeV where the RSM curves coincide with the RFG ones [18]. A similar conclusion is reached in [19], where a comparison is made between RPWIA shell-model cross sections and RFG results. As the neutrino energy increases to 1 GeV, the RFG curves approach more and more the RPWIA predictions. In the same work, two methods to incorporate FSI mechanisms were compared: the Glauber approach applied here and the relativistic optical-potential approximation. At $E_\nu = 1$ GeV, both techniques were found to pro-

duce similar results down to remarkably low nucleon kinetic energies $T_N \sim 200$ MeV. Hence, as nuclear-model uncertainties seem to be negligible at $E_\nu = 1$ GeV for separate cross sections, we conclude that the PW relation, a superratio, mitigates these model dependences well below the level of all other nuclear effects studied in this work.
For isoscalar target nuclei and energetic neutrinos, the whole of nuclear-model uncertainties on the PW relation is seen to be well within percentage range. Evidently, this means that a PW measurement with percent-level accuracy can only resolve non-isoscalar nuclear effects. Notwithstanding the extreme stability with respect to theoretical uncertainties in nuclear modeling, a quick glance at the PW relation's Weinberg-angle sensitivity (from Eq. (2.61))

$$\frac{\Delta \mathrm{PW}}{\mathrm{PW}} = \frac{-\Delta \sin^2\theta_W}{\frac{1}{2} - \sin^2\theta_W}, \tag{2.66}$$

immediately qualifies any ambition to exploit the PW relation as an electroweak precision tool. From Eq. (2.66), a $\pm 1\%$ theoretical uncertainty on the PW relation would result in an equally large *nuclear-model error* on the Weinberg angle $\Delta_{nuc}(\sin^2\theta_W) = \mp 0.0028$. On the contrary, a 10% measurement error for the parity-violating asymmetry A_{PV} in $\vec{e}e$ Møller scattering at $Q^2 = 0.026$ GeV^2 translates in a 1% uncertainty on the corresponding Weinberg-angle value [127]. The newly proposed Qweak experiment at Jefferson Lab aims at a 4% measurement of the proton's weak charge Q_w^p, resulting in a 0.3% measurement of $\sin^2\theta_W$ [142]. In this type of experiments, the sensitivity to the weak mixing angle is substantially enhanced by the factor $1/4 - \sin^2\theta_W$ figuring in the A_{PV} expression. Obviously, the PW relation cannot compete with the level of sensitivity achievable in this sector and is therefore less suited as an electroweak precision test.

Strangeness

As a final point, we discuss the impact of the nucleon's strangeness content on the PW relation. For the strangeness parameter values, we adopt predictions from the chiral quark-soliton model (CQSM) with kaon asymptotics, namely $\mu_s = 0.115$ and $g_A^s = -0.075$ [84, 104]. It is important to stress that the available strangeness information still exhibits relatively large error flags. Moreover, as discussed in Section 2.1, there exist fundamental discrepancies between the experimentally favored positive μ_s and most hadron-model predictions. So, the values used here can be regarded as a model prediction for μ_s and g_A^s which is compatible with currently available data. Figure 2.19 illustrates the influence of non-zero strangeness parameters on the PW relation. As can be observed from the left panel, the inclusion of strangeness alters the PW relation for an isoscalar target by an amount of $\sim 1\%$. For ^{56}Fe, a nucleus with neutron excess, the effect is larger ($\sim 2\%$). Summing over an equal number of

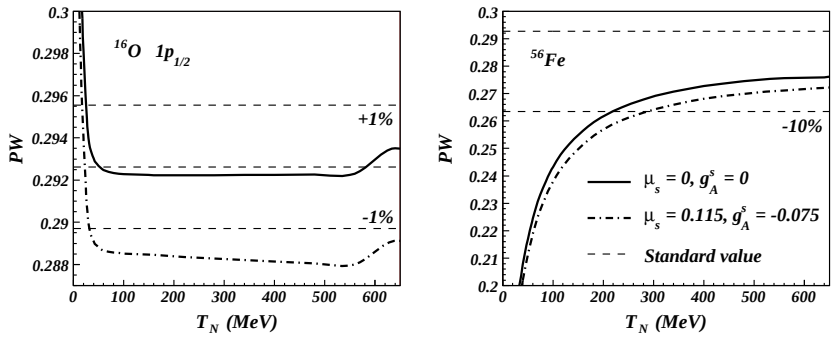

Figure 2.19: The left (right) panel shows the RPWIA Paschos-Wolfenstein relation for the ^{16}O $1p_{1/2}$ shell (an ^{56}Fe target nucleus) and a 1 GeV incoming neutrino energy. Full (dash-dotted) lines correspond to $g_A^s = \mu_s = 0$ ($g_A^s = -0.075, \mu_s = 0.115$). For comparison, the standard PW values without strangeness are included (dashed lines).

proton and neutron contributions effectively cancels all isovector-strangeness interference terms, thereby reducing the PW relation to the analytic estimate (2.64). On the contrary, the extra neutrons in ^{56}Fe skew this proton-neutron balance, producing a larger deviation from the PW relation without strangeness.

Clearly, strangeness adds a significant amount of uncertainty when attempting to determine $\sin^2\theta_W$ from the PW relation. A simple way of visualizing the mutual influence of the parameters entering the PW relation is by considering the correlation plots in Fig. 2.20. We took Eq. (2.64) with the baseline parameter values as a starting point to calculate the lines of constant PW. From the left panel of Fig. 2.20, one can infer that a 50% uncertainty on g_A^s translates in a 0.7% error on $\sin^2\theta_W$ if we assume that everything else is known. On the other hand, extracting $\sin^2\theta_W$ from the PW relation is visibly less sensitive to the value of μ_s, yielding only a +0.3% increase if μ_s is changed from 0.115 to 0. Again, it emerges that the limited information on g_A^s and μ_s presently at hand, does not allow one to exploit the PW relation to probe the Weinberg angle with the sensitivity achievable in PVES. Turning things around, however, a precisely known Weinberg-angle value may turn out valuable in trying to pin down g_A^s from a measurement of the QE PW relation. In Ref. [18], for example, the Paschos-Wolfenstein relation for proton knockout PW_p was seen to have a strong dependence on g_A^s. In addition, results presented here justify the optimism about a model-independent g_A^s determination [101] by measuring PW_p in the right circumstances, i.e. with an isoscalar target nucleus and an incoming neutrino energy of about 1 GeV. To study how the finite precision on $\sin^2\theta_W$ and μ_s influences the accuracy with which g_A^s can be extracted from PW_p, we consider the correlation plots in Fig. 2.21. The curves were again drawn from Eq. (2.64), now retaining only the pro-

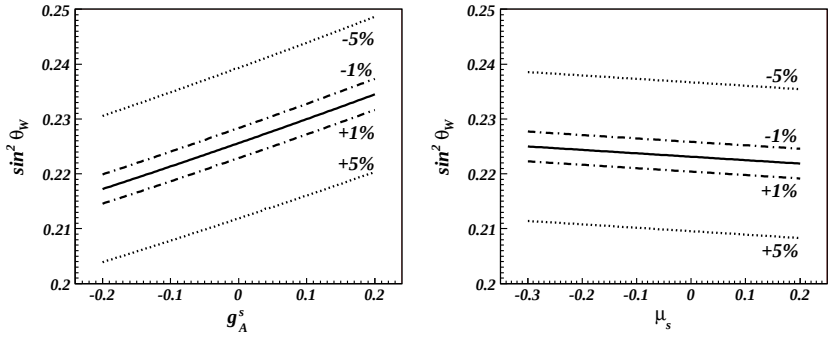

Figure 2.20: Plots showing how $\sin^2\theta_W$ and strangeness parameter values are correlated in the PW relation. The full line corresponds to values of the indicated parameters for which the PW relation is constant. The dash-dotted (dotted) lines have the same meaning, but with PW equal to ±1% (±5%) the full-line value.

ton contribution in the numerator ($\tau_3 = +1$) to obtain lines of constant PW_p. From this figure, we see that a 5% measurement of PW_p results in a ±0.067 determination of g_A^s. For comparison, the FINeSSE collaboration [143] aims at a 6% measurement of the NC/CC ratio down to $Q^2 = 0.2$ GeV^2, corresponding to a ±0.04 measurement of g_A^s. The left panel in Fig. 2.21 learns that a 1% uncertainty on $\sin^2\theta_W$ gives rise to a 20% uncertainty on g_A^s, assuming again that everything else is fixed. The inconclusive information on μ_s available at present has a far more severe effect on the value of g_A^s, as can be derived from the right panel. Shifting the strangeness magnetic moment from 0.115 to 0, g_A^s changes by ~ 0.07. We recall that nuclear-model uncertainties can be mitigated to the 1% level, corresponding to $\Delta_{nuc}(g_A^s) \sim 0.015$. This analysis stresses the importance of further experimental efforts to put more stringent limits on the strangeness form factors of the nucleon. As apparent from this PW_p case, experiments in the vector and axial-vector sector heavily depend on each other in the sense that both types of measurements need reliable input values for the other strangeness parameters.

2.7 Strangeness studies

Ratios of neutrino-induced cross sections are indeed considered as valuable tools for studying the strangeness content of the nucleon, and notably the strangeness contribution to the nucleon's spin g_A^s. Our study of the Paschos-Wolfenstein relation has made clear that nuclear-model uncertainties can be well controlled by choosing energetic neutrinos scattering off isoscalar target nuclei. Under these circumstances, ratios

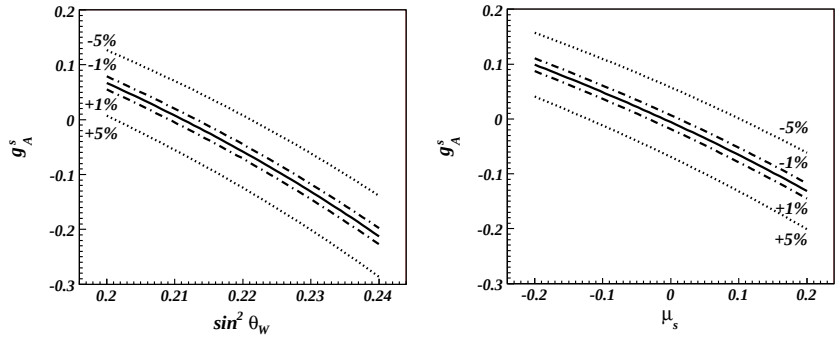

Figure 2.21: Correlation plots showing how the axial strangeness parameter g_A^s is intertwined with $\sin^2\theta_W$ (left) and μ_s (right) through the PW relation for proton knockout PW_p. The full line corresponds to values of the indicated parameters for which PW_p is constant. The dash-dotted (dotted) lines have the same meaning, but with PW_p equal to $\pm 1\%$ ($\pm 5\%$) the full-line value.

of cross sections provide theoretically clean probes for strangeness studies. Another advantage of cross-section ratios is that the sensitivity to strangeness parameters can be greatly enhanced if one opposes cross sections with different strangeness responses. For example, a well-considered ratio is the proton-to-neutron knockout ratio

$$\begin{aligned} R^{\nu}_{p/n} &= \frac{\sigma^{NC}(\nu p \to \nu p)}{\sigma^{NC}(\nu n \to \nu n)}, \\ R^{\overline{\nu}}_{p/n} &= \frac{\sigma^{NC}(\overline{\nu} p \to \overline{\nu} p)}{\sigma^{NC}(\overline{\nu} n \to \overline{\nu} n)}, \end{aligned} \tag{2.67}$$

which contrasts the opposite signs of strangeness-isovector interference contributions to proton- and neutron-knockout processes. To avoid difficulties inherent to neutron detection, the denominator in Eq. (2.67) can be replaced by a CC cross section, yielding

$$\begin{aligned} R^{\nu}_{NC/CC} &= \frac{\sigma^{NC}(\nu p \to \nu p)}{\sigma^{CC}(\nu n \to \mu^- p)}, \\ R^{\overline{\nu}}_{NC/CC} &= \frac{\sigma^{NC}(\overline{\nu} p \to \overline{\nu} p)}{\sigma^{CC}(\overline{\nu} p \to \mu^+ n)}. \end{aligned} \tag{2.68}$$

Since strange-quark contributions enter as isoscalar terms in the weak current, the purely isovector denominators in Eq. (2.68) are not sensitive to strangeness variations. Considering the ratio of NC to CC cross sections thus enhances the overall

sensitivity to strangeness terms in the numerator. Other ratios that have been proposed include the Paschos-Wolfenstein relation for proton (R^p_{PW}) and neutron (R^n_{PW}) knockout and the longitudinal polarization asymmetry A_l. The latter is defined as the difference between cross sections for nucleon ejectiles with opposite helicities, normalized to the total NC nucleon-knockout cross section,

$$\begin{aligned} A_l^{\nu} &= \frac{\sigma^{NC}(\nu p \to \nu p, h_p = +1) - \sigma^{NC}(\nu p \to \nu p, h_p = -1)}{\sigma^{NC}(\nu p \to \nu p, h_p = +1) + \sigma^{NC}(\nu p \to \nu p, h_p = -1)}, \\ A_l^{\overline{\nu}} &= \frac{\sigma^{NC}(\overline{\nu} p \to \overline{\nu} p, h_p = +1) - \sigma^{NC}(\overline{\nu} p \to \overline{\nu} p, h_p = -1)}{\sigma^{NC}(\overline{\nu} p \to \overline{\nu} p, h_p = +1) + \sigma^{NC}(\overline{\nu} p \to \overline{\nu} p, h_p = -1)}. \end{aligned} \tag{2.69}$$

Although a measurement would pose an immense experimental challenge, the quantities in Eq. (2.69) prove to be strongly subject to strange-quark contributions [144]. Recently, the ratios introduced above have been at the center of a considerable number of theoretical studies [18, 71, 141, 144–148]. Whereas most of these efforts focus on a scrutiny of the individual ratios with respect to their strangeness sensitivity, the work presented in Ref. [71] takes a more systematic approach. There, a measure for the strangeness sensitivity of a ratio R is defined as

$$\left| \frac{R(s=0) - R(s)}{R(s=0)} \right|. \tag{2.70}$$

Plotting the quantity in Eq. (2.70) for different ratios allows a direct comparison of their sensitivity to the strangeness parameters g_A^s, μ_s and r_s^2. This is shown in Fig. 2.22 for the case of 1-GeV (anti)neutrino scattering from ^{12}C. Clearly, the antineutrino helicity asymmetry $A_l^{\overline{\nu}}$ has no equal when it comes to probing strangeness effects. It is the sole quantity that is more sensitive to the vector than to the axial strangeness parameters. Nonetheless, only $R^{\overline{\nu}}_{p/n}$ can compete with $A_l^{\overline{\nu}}$ in its sensitivity to g_A^s. For most ratios, the antineutrino version exhibits a stronger strangeness sensitivity than the ratio constructed using neutrino-induced cross sections. The sensitivity of some ratios strongly depends on the sign of the strangeness parameters. $R^{\overline{\nu}}_{p/n}$ and $R^{\overline{\nu}}_{NC/CC}$ offer good perspectives in obtaining g_A^s information, and are not affected too much by the influence of r_s^2 and μ_s. The Paschos-Wolfenstein relation on the other hand, is most sensitive to the vector strange form factors while its sensitivity to g_A^s is rather marginal. It goes without saying that the information obtained in this way is of great value to neutrino-scattering experiments aiming at a precision measurement of g_A^s, such as FINeSSE [143]. In this respect, an important lesson to be drawn from Fig. 2.22 is the strong influence of strange vector form factors on the considered ratios. As already concluded in the case of the Paschos-Wolfenstein relation in Section 2.6, it takes a set of well-constrained vector parameters to extract new information on the axial ones.

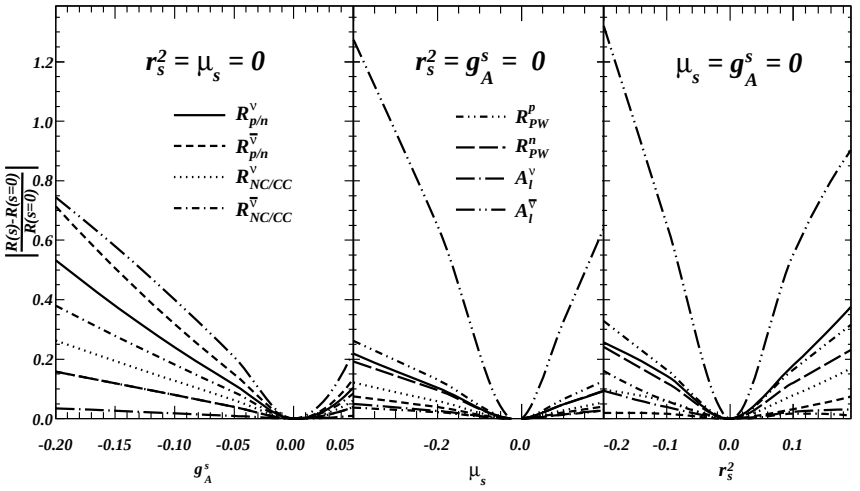

Figure 2.22: Comparison of the strangeness influence on various ratios of total cross sections in terms of the relative sensitivity $\left|\frac{R(s)-R(s=0)}{R(s=0)}\right|$. The presented results apply to 1-GeV neutrino scattering off a carbon target nucleus.

2.8 Comparison to other work

We conclude this chapter with comparing our QE neutrino-nucleus cross sections to other approaches. Generally speaking, one can make a distinction between two lines of research according to how the term *quasi-elastic scattering* is filled in exactly. A first category of QE studies, including our approach, adheres to the definition of a direct nucleon-knockout mechanism. In this case, one is solely interested in those nucleons that escape the nucleus without any further interaction. The recoiling $(A-1)$ system is left in a single-hole state, corresponding to an excitation energy that does not exceed a few tens of MeV. Experimentally, these direct processes are selected by means of a cut in the missing energy $E_m \leq 80$ MeV. To compute the attenuation of the scattering wave function, one makes use of complex optical potentials in RDWIA models [19, 33–35], or Glauber approaches [19] as applied in this thesis. The main motivation to pursue this line of work stems from the possibility of a fully quantum-mechanical treatment of the nucleon-knockout process. In addition, the RDWIA and RMSGA models have been tested extensively and with great success against a plethora of exclusive and semi-exclusive $(e, e'p)$ data [38].

Ongoing neutrino experiments, however, have limited means to identify the missing energy of the recoiling nucleus. Thus, as long as the final nuclear state remains unobserved, a more realistic viewpoint of QE scattering would be to consider

$$\nu + A \longrightarrow \nu'/l + N + X, \tag{2.71}$$

which still allows for all final nuclear configurations X. Efforts to model the process in Eq. (2.71) employ Monte-Carlo simulation methods [25] or semi-classical techniques, as in the Giessen coupled-channel transport model [41]. Whereas a quantum-mechanical description is beyond the reach of these models, they manage to provide a more *inclusive* description of QE reactions. Equation (2.71) indeed presupposes no cuts in E_m, hence including processes where several nucleons come off the nucleus, or where the final nucleus breaks apart.

To put our calculations for the single-nucleon knockout channel in a more general perspective, in Fig. 2.23 we present a comparison with results obtained by the Giessen group [149]. It should be noted that, in addition to QE interactions, the Giessen calculations also consider the initial excitation of resonances as a source of the total nucleon-knockout strength. For lower incoming neutrino energies, however, the contribution of Δ production is shown to be marginal [149]. Comparing our RPWIA calculations to the Giessen results without FSI in Fig. 2.23, one then notices a good agreement at $E_\nu = 500$ MeV. On the other hand, for $E_\nu = 1$ GeV, the Giessen strength is more than double compared to ours. At this energy, initial Δ excitation clearly leads to a significant contribution to nucleon knockout. Comparing results where FSI are taken into account reveals even bigger contrasts. Our RMSGA calculations describe the loss of flux due to inelastic interactions undergone by the ejectile, retaining only

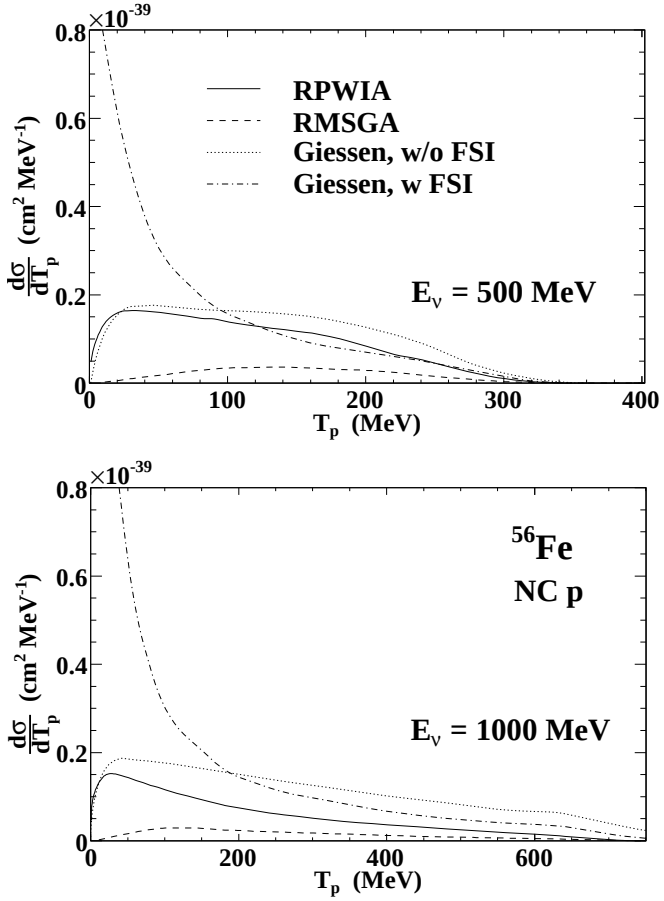

Figure 2.23: Comparison of RPWIA and RMSGA calculations performed by the Ghent group with results obtained in the Giessen coupled-channel transport model [149] for the NC proton knockout from iron.

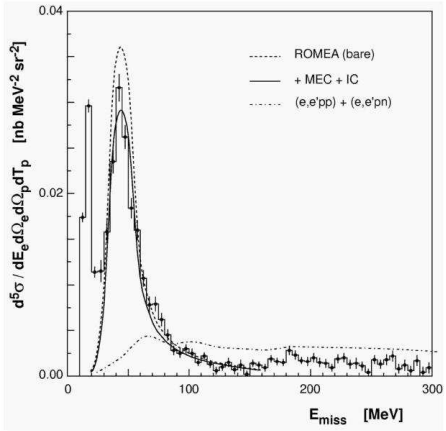

Figure 2.24: Missing-energy dependence of ^{16}O$(e,e'p)$ data compared with theoretical calculations by the Ghent group [38]. Figure taken from [38].

those nucleons that come straight from the vertex. To the contrary, when FSI are *turned on* in the Giessen model, the nucleons that are subject to secondary interactions are not just absorbed but -through rescattering- ejected with a different energy, angle, and/or charge. As shown in Fig. 2.23, this leads to a depletion of the high-T_p side of the spectrum, in favor of an increase of secondary nucleons at lower nucleon kinetic energies. As a matter of fact, rescatterings are seen to cause an enhancement of the total proton-knockout yield, with respect to the case where no FSI are included. Interestingly, the Giessen calculations seem to suggest that secondary processes and cross feeding make the proton-knockout cross section to peak at high missing energies. This is an intriguing result, as $(e,e'p)$ measurements probing high missing energies have provided a quite different picture. Figure 2.24, for example, illustrates the E_m dependence of ^{16}O$(e,e'p)$ data taken from Ref. [38]. The data are compared to a number of calculations performed by the Ghent theory group. The computations in the relativistic optical model eikonal approximation (ROMEA) make use of optical potentials to compute the scattering wave function. In addition, the effect of two-body meson-exchange (MEC) and isobar currents (IC) on the ROMEA calculations is investigated, and the contribution of two-nucleon knockout to the $(e,e'p)$ data is shown. Beyond the peaks corresponding to proton knockout from the $1s$ and $1p$ states of ^{16}O, the data indicate a smooth E_m dependence of the cross section for $E_m > 100$ MeV. Furthermore, compared to the single-particle contribution, the region of higher missing energies is seen to account for only a small portion of the proton-knockout cross section.

3

Delta-mediated pion production

As evidenced in the introductory chapter, at moderate Q^2, processes whereby a nucleon is excited to a Δ resonance account for the lion's share of the weak nuclear response in the energy region between the dip and DIS regimes. Moreover, a discussion of Δ production in this thesis seems all the more natural when considering the many similarities this process shares with the QE one. Indeed, both the QE and Δ peaks are especially prone to one-body kinematics. Because of the Δ mass, $M_\Delta = 1232$ MeV, one needs to transfer an extra $\omega \approx 300$ MeV to the nuclear system. Consequently, most of the approximations and tools introduced in the previous chapter can be equally well applied to the Δ-production case. We continue to work in the IA, for example, using the same nuclear-physics input as before. Of course, there are obvious differences. On the elementary level, one needs to discuss the weak and strong couplings of the Δ. For nuclear reactions, medium modifications of Δ properties should be accounted for. In addition, for pion production following Δ decay, we will need to compute FSI effects on the pion scattering wave function.

Accordingly, this chapter has been divided into three main parts. First, we investigate Δ production on a free nucleon, focusing mainly on the elementary Δ couplings. We introduce the weak $N-\Delta$ transition form factors and discuss their theoretical and experimental constraints. In relation to the decay vertex, special attention is paid to the notion of a *consistent* coupling, which couples solely to the physical, spin-3/2 part of the Δ propagator. We present results for the free process and compare them to bubble-chamber data. Next, turning to nuclear targets, we construct the eightfold differential

Table 3.1: Clebsch-Gordan coefficients $\langle 1\, I_1\, \frac{1}{2}\, I_2 | \frac{3}{2}\, I_3 \rangle$ [53] for composing an isospin $I = 3/2$ state from $I = 1$ and $I = 1/2$ states.

I_1 $I_2 \setminus I_3$	$+3/2$	$+1/2$	$-1/2$	$-3/2$
$+1$ $+1/2$	1			
$+1$ $-1/2$		$\sqrt{1/3}$		
0 $+1/2$		$\sqrt{2/3}$		
0 $-1/2$			$\sqrt{2/3}$	
-1 $+1/2$			$\sqrt{1/3}$	
-1 $-1/2$				1

cross section corresponding to Δ-mediated one-pion production in a nucleus. Using the bound-state propagator introduced in the previous chapter, and taking care of medium modifications to the mass and width of the Δ, we present numerical RPWIA calculations for a range of target nuclei and neutrino energies. A comparison with both inclusive electron-scattering data and alternative theoretical approaches is provided. Finally, in the last section, we concentrate on the process of coherent pion production off nuclei. Thereby, we go beyond the so-called *local* approximation that is commonly adopted in other theoretical works. The pion attenuation is computed in a Glauber approach. Results are presented for typical MiniBooNE and MINERνA conditions.

3.1 Pion production on a nucleon

3.1.1 Isospin considerations

When exciting a free nucleon to a Δ, it will always decay into a pion and a nucleon. Although non-resonant mechanisms also contribute to one-pion production [150, 151], in this thesis, we adhere to the Δ-dominance model. Figure 3.1 shows a number of pion-production calculations performed within the Sato-Lee model [150], which includes both resonant and non-resonant terms. Clearly, Δ-mediated pion production accounts for the major part of the cross section. Depending on the considered channel, non-resonant backgrounds stand for 10-30% of the total strength. The role of the background has also been quantified in Ref. [151, 152], yielding similar results at 1-GeV neutrino energies. As present uncertainties on neutrino pion-production data are of the same level, the Δ-dominance approximation seems a reasonable one. Hence, assuming that all produced pions originate from the decay of a Δ resonance,

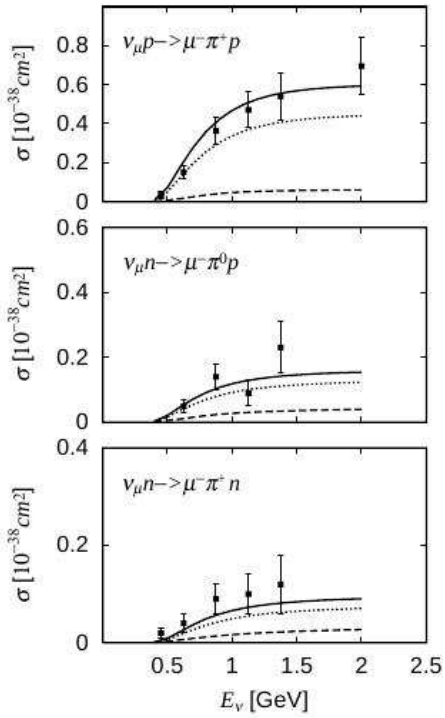

Figure 3.1: Total pion-production cross sections computed within the dynamical Sato-Lee model [150]. The solid (dotted) curves represent full calculations, with (without) pion-cloud effects on $N-\Delta$ transitions. The dashed curves are non-resonant background contributions. Figure taken from Ref. [150].

the neutrino-induced CC processes under study are

$$\nu + p \xrightarrow{\Delta^{++}} l^- + p + \pi^+, \tag{3.1}$$

for scattering from a free proton, and

$$\begin{aligned} \nu + n &\xrightarrow{\Delta^{+}} l^- + p + \pi^0, \\ \nu + n &\xrightarrow{\Delta^{+}} l^- + n + \pi^+, \end{aligned} \tag{3.2}$$

for scattering from a free neutron. Similarly, anti-neutrino CC scattering yields the reactions

$$\begin{aligned} \overline{\nu} + p &\overset{\Delta^0}{\rightarrow} l^+ + p + \pi^-, \\ \overline{\nu} + p &\overset{\Delta^0}{\rightarrow} l^+ + n + \pi^0, \end{aligned} \tag{3.3}$$

and

$$\overline{\nu} + n \overset{\Delta^-}{\rightarrow} l^+ + n + \pi^-. \tag{3.4}$$

The NC processes can be written concisely as

$$\begin{aligned} \nu + p &\rightarrow \nu + \Delta^+, \\ \nu + n &\rightarrow \nu + \Delta^0, \end{aligned} \tag{3.5}$$

with the same decay channels as in Eqs. (3.2) and (3.3). The strength of the above reactions can now be related by looking at Table 3.1. Writing in isospin notation, $|I, I_3\rangle$,

$$\Delta^{++} = |3/2, +3/2\rangle, \Delta^+ = |3/2, +1/2\rangle, \Delta^0 = |3/2, -1/2\rangle, \Delta^- = |3/2, -3/2\rangle, \tag{3.6}$$

and similarly for the pion ($I = 1$), nucleon ($I = 1/2$) and weak vector boson ($I = 1$) states, Table 3.1 provides the Clebsch-Gordan coefficients to derive the relative strength of the Δ production and decay channels. Thus, concerning the reactions in Eqs. (3.1) and (3.2) for example, the corresponding cross sections are related by the expressions

$$\sigma(W^+ p \overset{\Delta^{++}}{\rightarrow} p\pi^+) = 9\sigma(W^+ n \overset{\Delta^+}{\rightarrow} n\pi^+) = \frac{9}{2}\sigma(W^+ n \overset{\Delta^+}{\rightarrow} p\pi^0). \tag{3.7}$$

3.1.2 Kinematics and cross section

In a laboratory frame of reference, the free pion-production process is described by the following differential cross section [44]

$$\begin{aligned} d^9\sigma = \frac{1}{\beta}\frac{m_\nu}{E_\nu}\frac{m_l}{E_l}\frac{d^3\vec{k}_l}{(2\pi)^3}\frac{m_N}{E_N}\frac{d^3\vec{k}_N}{(2\pi)^3}\frac{d^3\vec{k}_\pi}{2E_\pi(2\pi)^3} \\ \times\overline{\sum}_{fi}\left|M_{fi}^{(free)}\right|^2(2\pi)^4\delta^{(4)}(k_\nu + k_{N,i} - k_l - k_\pi - k_N). \end{aligned} \tag{3.8}$$

Figure 3.2 defines our conventions for the kinematical variables. The different field normalizations follow the Bjorken & Drell conventions, listed in appendix A. In Eq. (3.8), the target nucleon has four-momentum $k^\mu_{N,i} = (m_N, \vec{0})$. We write $k^\mu_\nu =$

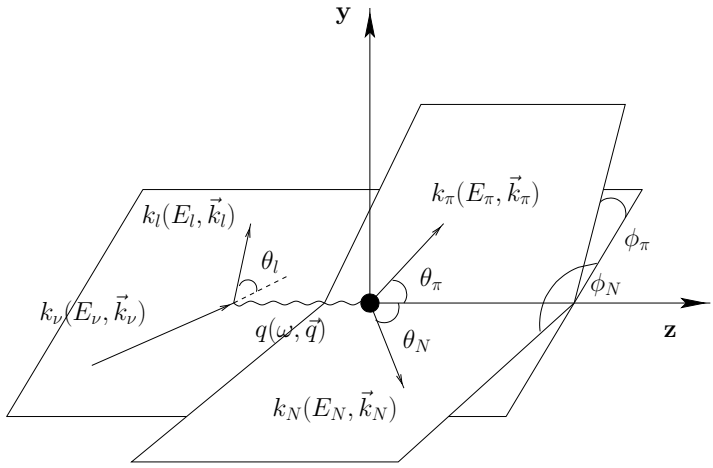

Figure 3.2: Kinematics for neutrino-induced one-pion production on the nucleon.

$(E_\nu, \vec{k}_\nu)$ for the incoming (anti)neutrino, $k_l^\mu = (E_l, \vec{k}_l)$ for the outgoing lepton, $k_\pi^\mu = (E_\pi, \vec{k}_\pi)$ for the outgoing pion and $k_N^\mu = (E_N, \vec{k}_N)$ for the outgoing nucleon. The xyz coordinate system is chosen such that the z axis lies along the momentum transfer $\vec{q}$, the y axis along $\vec{k}_\nu \times \vec{k}_l$, and the x axis in the lepton-scattering plane. In Eq. (3.8), the incoming neutrino's relative velocity $\beta = |\vec{k}_\nu|/E_\nu$ is 1. The neutrino mass m_ν will later cancel with the neutrino normalization factor appearing in the lepton tensor. The δ-function expresses energy-momentum conservation and $\overline{\sum}_{fi}|M_{fi}^{(free)}|^2$ denotes the squared invariant matrix element, appropriately averaged over initial spins and summed over final spins. Using the δ-function to integrate over the outgoing nucleon's three-momentum and the magnitude of the pion's momentum, one arrives at the fivefold cross section

$$\frac{d^5\sigma}{dE_l d\Omega_l d\Omega_\pi} = \frac{m_\nu m_l |\vec{k}_l| m_N |\vec{k}_\pi|}{2(2\pi)^5 E_\nu |E_N + E_\pi(|\vec{k}_\pi|^2 - \vec{q}\cdot\vec{k}_\pi)/|\vec{k}_\pi|^2|} \overline{\sum}_{fi} \left| M_{fi}^{(free)} \right|^2, \qquad (3.9)$$

where the solid angles Ω_l and Ω_π define the direction of the outgoing lepton and pion respectively.

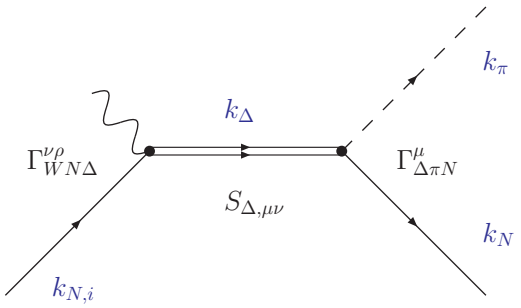

Figure 3.3: Feynman diagram for Δ-mediated one-pion production.

3.1.3 Matrix element for resonant one-pion production

Next to the kinematic phase-space factor, Eq. (3.9) contains the squared invariant matrix element

$$\overline{\sum}_{fi}\left|M_{fi}^{(free)}\right|^2 = \frac{1}{2}\sum_{\substack{s_\nu;s_l\\ s_{N,i};s_N}}\left[M_{fi}^{(free)}\right]^\dagger M_{fi}^{(free)}. \tag{3.10}$$

Here, the sum over final lepton and nucleon spins is taken. Averaging over the initial nucleon's spin $s_{N,i}$ leads to a factor $1/2$. An explicit expression for the invariant matrix element is obtained by applying the Feynman rules in momentum space. Working along the same lines as in section 2.1 for the QE case, one finds for the CC pion-production process

$$M_{fi}^{(free)} = i\frac{G_F\cos\theta_c}{\sqrt{2}}\langle J_{had}^{\mu(free)}\rangle S_{W,\mu\nu}\langle J_{lep}^{\nu}\rangle, \tag{3.11}$$

with G_F the Fermi constant and θ_c the Cabibbo angle. The lepton current is identical to the one in Eq. (2.11), and the weak boson propagator assumes the form of Eq. (2.8), but with M_Z replaced by M_W. The hadron current $J_{had}^{\mu(free)}$ contains all the information about the pion-production process. A Δ-dominance model translates itself in the diagram depicted in Fig. 3.3. Introducing the spinors $u(k_{N,i},s_{N,i})$ and $u(k_N,s_N)$ for the incoming and scattered nucleon, the hadron-current matrix element can be written as

$$\langle J_{had}^{\mu(free)}\rangle = \overline{u}(k_N,s_N)\Gamma^{\rho}_{\Delta\pi N}S_{\Delta,\rho\sigma}\Gamma^{\sigma\mu}_{WN\Delta}u(k_{N,i},s_{N,i}), \tag{3.12}$$

where $\Gamma^{\sigma\mu}_{WN\Delta}$ denotes the vertex function corresponding to the weak production of a Δ resonance. The Δ decay into a pion and a nucleon is described by $\Gamma^{\rho}_{\Delta\pi N}$, and $S_{\Delta,\rho\sigma}$ is the Δ propagator. Each of these couplings will be discussed in detail in the

following sections. Filling in the appropriate expressions in Eq. (3.11), and working out Eq. (3.10), the squared invariant matrix element can be cast into the form

$$\overline{\sum_{fi}}\left|M_{fi}^{(free)}\right|^2 = \frac{G_F^2\cos^2\theta_c M_W^4}{2(M_W^2+Q^2)^2}H^{\mu\nu}_{(free)}L_{\mu\nu}, \tag{3.13}$$

where the leptonic tensor is given by Eq. (2.12). Introducing the shorthand notation $\mathcal{O}^\nu = \Gamma^\rho_{\Delta\pi N}S_{\Delta,\rho\sigma}\Gamma^{\sigma\nu}_{WN\Delta}$, one arrives at the following expression for the hadronic tensor

$$H^{\mu\nu}_{(free)} = \frac{1}{8m_N^2}\mathrm{Tr}\Big((\not{k}_{N,i}+m_N)\widetilde{\mathcal{O}}^\mu(\not{k}_N+m_N)\mathcal{O}^\nu\Big), \tag{3.14}$$

where $\widetilde{\mathcal{O}}^\mu = \gamma_0(\mathcal{O}^\mu)^\dagger\gamma_0$. Clearly, the least-known physics is contained in the vertex functions of the matrix element of Eq. (3.12). Sections 3.1.4-3.1.6 provide an in-depth look at each of these Δ couplings.

3.1.4 $N-\Delta$ transition form factors

For the Δ-production vertex, we adopt the form [153]

$$\begin{aligned}\Gamma^{\sigma\mu}_{WN\Delta}(k_\Delta,q) = &\left[\frac{C_3^V(Q^2)}{m_N}(g^{\sigma\mu}\not{q}-q^\sigma\gamma^\mu)+\frac{C_4^V(Q^2)}{m_N^2}(g^{\sigma\mu}q\cdot k_\Delta - q^\sigma k_\Delta^\mu)\right.\\ &\left.+\frac{C_5^V(Q^2)}{m_N^2}(g^{\sigma\mu}q\cdot k_{N,i}-q^\sigma k_{N,i}^\mu)+g^{\sigma\mu}C_6^V(Q^2)\right]\gamma_5\\ &+\frac{C_3^A(Q^2)}{m_N}(g^{\sigma\mu}\not{q}-q^\sigma\gamma^\mu)+\frac{C_4^A(Q^2)}{m_N^2}(g^{\sigma\mu}q\cdot k_\Delta - q^\sigma k_\Delta^\mu)\\ &+C_5^A(Q^2)g^{\sigma\mu}+\frac{C_6^A(Q^2)}{m_N^2}q^\sigma q^\mu,\end{aligned} \tag{3.15}$$

which relates to the $n\to\Delta^+$ transition. The vector (C_i^V, $i=3..6$) and axial (C_i^A, $i=3..6$) form factors are to be constrained by physical principles and experimental data. Owing to the purely isovector $N-\Delta$ transition, the NC analogues of the transition form factors are readily given by

$$\begin{aligned}C_i^{V,NC} &= (1-2\sin^2\theta_W)C_i^V, \quad i=3..6,\\ C_i^{A,NC} &= C_i^A, \quad i=3..6.\end{aligned} \tag{3.16}$$

Imposing weak vector current conservation, $q_\mu\Gamma^{\sigma\mu}_{WN\Delta}=0$ leads to $C_6^V=0$. The PCAC hypothesis, together with the pion-pole dominance assumption, yields the following relation between C_5^A and the pseudoscalar form factor C_6^A

$$C_6^A = C_5^A\frac{m_N^2}{Q^2+m_\pi^2}. \tag{3.17}$$

At $Q^2 = 0$, the off-diagonal Goldberger-Treiman relation gives $C_5^A = 1.2$ [154]. Furthermore, CVC entails that the weak vector current and the isovector part of the electromagnetic current are components of the same isospin current. Consequently, after extracting the electromagnetic form factors from electroproduction data, the $C_i^V, i = 3,4,5$ follow immediately by applying the appropriate transformations in isospin space. To extract the vector form factors, it has been established that the magnetic-dipole (M1) dominance of the electromagnetic $N \to \Delta$ transition amplitude is a reasonable assumption [155]. Indeed, in a simple quark picture, the $N \to \Delta$ transition can be interpreted as a spin flip of a u quark induced by a $1/2^+ \to 3/2^+$ M1 multipole. This M1 dominance leads to the conditions [154, 156]

$$C_4^V = -C_3^V \frac{m_N}{W}, \quad C_5^V = 0, \tag{3.18}$$

where W is the invariant mass, defined as $W = \sqrt{k_\Delta^2}$. In other words, one is left with C_3^V, the other C_i^V being either 0 or related to it. For its Q^2 dependence, a modified-dipole parameterization is extracted [157, 158]

$$C_3^V = \frac{1.95 D_V}{1 + Q^2/4M_V^2}, \tag{3.19}$$

with $D_V = (1 + Q^2/M_V^2)^{-2}$ the dipole function and $M_V = 0.84$ GeV. Equation 3.19 results from a Δ-dominance fit [157] to the Brookhaven (BNL) Q^2 spectrum [159]. The faster-than-dipole fall-off reflects the fact that the Δ is a more extended object than a nucleon. More recently, a direct analysis of the electroproduction helicity amplitudes from JLab and Mainz experiments resulted in an alternative parameterization of the weak vector form factors [160]

$$C_3^V = \frac{2.13 D_V}{1 + Q^2/4M_V^2}, \quad C_4^V = \frac{-1.51}{2.13} C_3^V, \quad C_5^V = \frac{0.48 D_V}{1 + Q^2/0.776 M_V^2}, \tag{3.20}$$

attributing a non-zero strength to the weak vector form factor C_5^V. In the remainder of this work, we will refer to Eq. (3.20) as the Lalakulich fit of the vector form factors.

The axial form factors C_i^A are subject to much larger uncertainties, as they are constrained by bubble-chamber neutrino data from the seventies and eighties, which have large error bars. Just as in the QE case, the pseudoscalar form factor C_6^A appears in terms that are proportional to the outgoing lepton mass. Hence, its contribution can be safely neglected in NC channels and, as we concluded in section 2.5, even in ν_e- and ν_μ-induced CC reactions. A popular parameterization for the remaining axial form factors is given by [41, 157, 158]

$$C_5^A = \frac{1.2}{(1 + Q^2/M_A^2)^2} \frac{1}{1 + Q^2/3.0 M_A^2}, \quad C_4^A = -\frac{C_5^A}{4}, \quad C_3^A = 0, \tag{3.21}$$

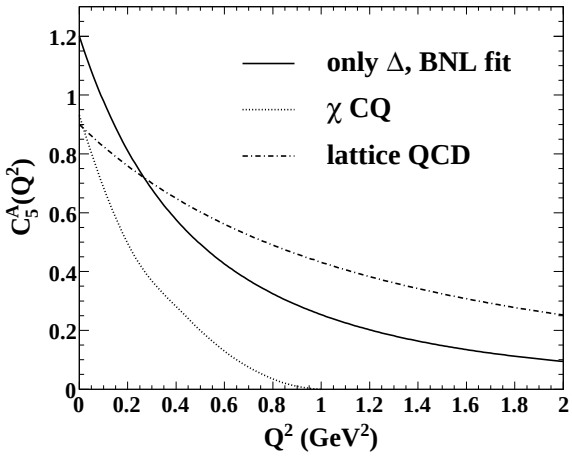

Figure 3.4: Results for the axial transition form factor $C_5^A(Q^2)$. The full line represents Eq. (3.21). The dash-dotted line shows a quenched lattice result, and is parameterized as $C_5^A(Q^2) = C_5^A(0)(1 + Q^2/\tilde{M}_A^2)^{-2}$, $C_5^A(0) = 0.9$ and $\tilde{M}_A = 1.5$ GeV [161]. The dotted line is the χCQ result from Ref. [162].

where $M_A = 1.05$ GeV. In Eq. (3.21), the Adler-model prescriptions [163] for C_3^A and C_4^A were used, which again leads to one independent form factor, C_5^A. The resulting Q^2 dependence for C_5^A was then found by a fit to BNL neutrino-scattering data. Fixing its value at $Q^2 = 0$ by PCAC, $C_5^A(0) = 1.2$, and keeping the axial mass at $M_A = 1.05$ GeV, a best fit to the BNL Q^2 distribution was found for the factor 3.0 appearing in the modified-dipole form of Eq. (3.21) [157]. One should realize, however, that there is still quite some arbitrariness in the axial $N-\Delta$ form factors. The extracted axial-mass value, for example, is heavily model-dependent [151, 164]. A re-analysis [151] of Argonne (ANL) bubble-chamber data [165] within a model that includes background contributions next to the Δ-pole mechanism reveals a $C_5^A(0)$ value that is lower than the one predicted by the Goldberger-Treiman relation. Various theoretical calculations of the most important axial form factor, $C_5^A(Q^2)$, also reveal highly different pictures [161, 162, 166–169]. Recent chiral constituent-quark (χCQ) results [162] and lattice QCD calculations [161, 166] seem to provide support for $C_5^A(0) < 1.2$. Figure 3.4 compares the two theoretical results with the phenomenological fit of Eq. (3.21). It can be clearly seen that all three approaches exhibit highly different Q^2 evolutions.

3.1.5 The Δ propagator

In the Rarita-Schwinger formalism for free spin-3/2 particles [170], a Δ is constructed as a field ψ_a^μ that transforms under a Lorentz transformation as a product of a four-vector and a Dirac spinor. As such, ψ_a^μ has one Lorentz index $\mu = 0..3$ and one Dirac spinor index $a = 0..3$, which together constitute an object with 16 degrees of freedom. In contrast, a free Δ has only 4 positive-energy and 4 negative-energy spin states, meaning that 8 restrictions have to be imposed on ψ_a^μ in order to enforce the elimination of unwanted spin-1/2 degrees of freedom. This leads to the Rarita-Schwinger equations [170]

$$\left(i\,\not{\partial} - M_\Delta\right)_{ab}\psi_b^\mu = 0, \quad \gamma_\mu\psi_a^\mu = 0, \quad \partial_\mu\psi_a^\mu = 0. \tag{3.22}$$

Within the Rarita-Schwinger theory, the free Δ propagator is given by [171]

$$S_{\Delta,\rho\sigma}(k_\Delta) = \frac{-(\not{k}_\Delta + M_\Delta)}{k_\Delta^2 - M_\Delta^2 + iM_\Delta\Gamma}\left(g_{\rho\sigma} - \frac{\gamma_\rho\gamma_\sigma}{3} - \frac{2k_{\Delta,\rho}k_{\Delta,\sigma}}{3M_\Delta^2} - \frac{\gamma_\rho k_{\Delta,\sigma} - \gamma_\sigma k_{\Delta,\rho}}{3M_\Delta}\right), \tag{3.23}$$

where Γ stands for the free decay width of the Δ resonance. In terms of the projection operators on the spin-3/2 and spin-1/2 sectors, the propagator in Eq. (3.23) can also be rewritten as [171]

$$S_{\Delta,\rho\sigma}(k_\Delta) \sim \left(\frac{1}{M_\Delta - \not{k}_\Delta}P_{\rho\sigma}^{3/2} + \frac{2(M_\Delta + \not{k}_\Delta)}{3M_\Delta^2}P_{22,\rho\sigma}^{1/2} - \frac{1}{\sqrt{3}M_\Delta}\left(P_{12,\rho\sigma}^{1/2} + P_{21,\rho\sigma}^{1/2}\right)\right), \tag{3.24}$$

where only the $P_{\rho\sigma}^{3/2}$ term projects spin-3/2 states. It is explicitly given by

$$P_{\rho\sigma}^{3/2} = g_{\rho\sigma} - \frac{1}{3}\gamma_\rho\gamma_\sigma - \frac{1}{3k_\Delta^2}\left(\not{k}_\Delta\gamma_\rho k_{\Delta,\sigma} + \gamma_\sigma k_{\Delta,\rho}\,\not{k}_\Delta\right). \tag{3.25}$$

We note that the Δ propagator in Eq. (3.23) is proportional to the pure spin-3/2 projection operator if and only if it satisfies the conditions in Eq. (3.22). Requiring that

$$\gamma^\rho S_{\Delta,\rho\sigma} = S_{\Delta,\rho\sigma}\gamma^\sigma = k_\Delta^\rho S_{\Delta,\rho\sigma} = S_{\Delta,\rho\sigma}k_\Delta^\sigma = 0, \tag{3.26}$$

it is seen that the restrictions are only met for an on-shell Δ, for which $W = M_\Delta$. Therefore, in Ref. [171], it is put forward that every interaction vertex involving a Δ propagator should automatically remove the spin-1/2 contributions. Δ interactions that couple to the correct number of degrees of freedom are called *consistent*. The question is then: how do we construct such interactions? Pascalutsa and collaborators [172] propose to start from an interaction Lagrangian $\mathscr{L}$ that is gauge invariant with respect to the Δ particle,

$$\mathscr{L} = \mathscr{O}^{\alpha\beta}G_{\alpha\beta} = \mathscr{O}^{\alpha\beta}(\partial_\alpha\psi_\beta - \partial_\beta\psi_\alpha), \tag{3.27}$$

where $\mathcal{O}^{\alpha\beta}$ contains other fields than spin-3/2 fields, derivatives of those fields and all kinds of γ-matrices. Applying the Feynman rules, the vertex function corresponding with the interaction (3.27) is given by

$$\begin{aligned}\Gamma_{\Delta\ldots}(k_\Delta,\ldots)^{\rho\cdots} &= \tilde{\mathcal{O}}^{\alpha\beta\cdots}\left(ik_{\Delta,\alpha}\delta^\rho_\beta - ik_{\Delta,\beta}\delta^\rho_\alpha\right),\\ &= i\left(\tilde{\mathcal{O}}^{\alpha\rho\cdots} - \tilde{\mathcal{O}}^{\rho\alpha\cdots}\right)k_{\Delta,\alpha},\end{aligned} \tag{3.28}$$

where the index ρ labels the spin-3/2 field. The function $\tilde{\mathcal{O}}$ differs from $\mathcal{O}$ in the sense that all the fields are removed and the derivatives are replaced by momenta; it may depend on all momenta and may have extra Lorentz indices for couplings to other particles. The following observation can now be made

$$k_{\Delta,\rho}\Gamma_{\Delta\ldots}(k_\Delta,\ldots)^{\rho\cdots} = i\left(\tilde{\mathcal{O}}^{\alpha\rho\cdots} - \tilde{\mathcal{O}}^{\rho\alpha\cdots}\right)k_{\Delta,\alpha}k_{\Delta,\rho} = 0, \tag{3.29}$$

due to the contraction of the antisymmetric part between brackets with the symmetric combination of momenta. In other words, the *transversality* condition in Eq. (3.29) is necessarily fulfilled for the Δ gauge-invariant interaction of Eq. (3.27). It is now immediately clear how such interactions accomplish that only the physical spin-3/2 part is coupled. Reconsidering the matrix element in Eq. (3.12), one observes that the Δ propagator $S_{\Delta,\rho\sigma}(k_\Delta)$ is sandwiched between two vertices

$$\Gamma^\rho_{\Delta\pi N}(\ldots,k_\Delta)S_{\Delta,\rho\sigma}(k_\Delta)\Gamma^{\sigma\mu}_{WN\Delta}(k_\Delta,\ldots). \tag{3.30}$$

Thus, starting from consistent interaction Lagrangians to build the vertices $\Gamma_{\Delta\pi N}$ and $\Gamma_{WN\Delta}$, one knows that the transversality condition is satisfied upon contraction with the Δ propagator. As a consequence, the momentum-dependent terms of the latter drop out and one gets

$$\Gamma^\rho_{\Delta\pi N}(\ldots,k_\Delta)\left(g_{\rho\sigma} - \frac{1}{3}\gamma_\rho\gamma_\sigma\right)\Gamma^{\sigma\mu}_{WN\Delta}(k_\Delta,\ldots), \tag{3.31}$$

which again is equivalent to

$$\Gamma^\rho_{\Delta\pi N}(\ldots,k_\Delta)P^{3/2}_{\rho\sigma}\Gamma^{\sigma\mu}_{WN\Delta}(k_\Delta,\ldots), \tag{3.32}$$

as the momentum-dependent part of the spin-3/2 projection operator in Eq. (3.25) vanishes anyway. This clearly shows that the gauge invariance of a Δ interaction takes care of the unwanted spin-1/2 parts in the Δ propagator.

With the transversality condition of Eq. (3.29) at hand, it can be easily checked that the Δ-production vertex of Eq. (3.15) is not a consistent interaction. Nevertheless, in this thesis, we will stick to the form-factor parameterization of the $WN\Delta$ coupling as it is presented in Eq. (3.15), arguing that the uncertainties in $C_i^A(Q^2)$ outweigh the spurious spin-1/2 contributions to the cross sections. In the next section, we will discuss a consistent alternative for the Δ decay coupling. By comparing couplings that do or do not decouple non-physical spin degrees of freedom, we will quantify the effect of unwanted spin-1/2 contributions in Section 3.1.7.

3.1.6 $\Delta\pi N$ coupling

A common way of describing the Δ decay is through the interaction Lagrangian [172]

$$\mathscr{L}_{\pi N\Delta} = \frac{f_{\pi N\Delta}}{m_\pi}\overline{\psi}_\rho \vec{T}^\dagger(\partial^\rho\vec{\phi})\psi + h.c.\ , \tag{3.33}$$

where ψ_ρ, $\vec{\phi}$ and ψ denote the spin-3/2 Rarita-Schwinger field, the pion field and the nucleon field respectively. The operator $\vec{T}$ is the isospin $1/2 \rightarrow 3/2$ transition operator. From (3.33), one derives the vertex function

$$\Gamma^\rho_{\Delta\pi N}(k_\pi) = \frac{f_{\pi N\Delta}}{m_\pi}k^\rho_\pi\ . \tag{3.34}$$

Clearly, the transversality condition of Eq. (3.29) is not fulfilled for this interaction, which will consequently couple to unwanted spin-1/2 parts of the Δ propagator. Therefore, as an alternative for the $\Delta\pi N$ interaction Lagrangian, Pascalutsa et al. [172] propose the form

$$\mathscr{L}^{(P)}_{\pi N\Delta} = \frac{f^*_{\pi N\Delta}}{m_\pi M_\Delta}\epsilon^{\alpha\beta\rho\sigma}\overline{G}_{\beta\alpha}\gamma_\rho\gamma_5\vec{T}^\dagger(\partial_\sigma\vec{\phi})\psi + h.c.\ . \tag{3.35}$$

The inclusion of $G_{\beta\alpha} = \partial_\beta\psi_\alpha - \partial_\alpha\psi_\beta$ makes $\mathscr{L}^{(P)}_{\pi N\Delta}$ manifestly gauge invariant with respect to the Δ particle. From the previous section, it follows that $\mathscr{L}^{(P)}_{\pi N\Delta}$ is consistent because it solely couples to the physical spin-3/2 degrees of freedom of the Δ. The corresponding vertex function becomes

$$\Gamma^{\rho(P)}_{\Delta\pi N}(k_\pi, k_\Delta) = \frac{f^*_{\pi N\Delta}}{m_\pi M_\Delta}\epsilon^{\rho\alpha\beta\gamma}k_{\pi,\alpha}\gamma_\beta\gamma_5 k_{\Delta,\gamma}\ . \tag{3.36}$$

For free Δs, the unphysical spin-1/2 terms are removed by both the Pascalutsa (3.36) and the traditional (3.34) couplings. Therefore, calculating the free decay width from either Eq. (3.34) or (3.36) will lead to the same expression, implying $f^*_{\pi N\Delta} = f_{\pi N\Delta}$. In appendix B, it is shown in detail how the energy-dependent Δ-width formula is derived. The result is

$$\Gamma(W) = \frac{1}{12\pi}\frac{f^2_{\pi N\Delta}}{m^2_\pi W}|\vec{q}_{cm}|^3(m_N + E_N), \tag{3.37}$$

where $\vec{q}_{cm}$ is the pion momentum in the center-of-mass frame of the decay pion and nucleon,

$$|\vec{q}_{cm}| = \frac{\sqrt{(W^2 - m^2_\pi - m^2_N)^2 - 4m^2_\pi m^2_N}}{2W}. \tag{3.38}$$

Requiring that $\Gamma(W = M_\Delta)$ equals the experimentally determined value of 120 MeV, one obtains $f_{\pi N\Delta} = 2.21$.

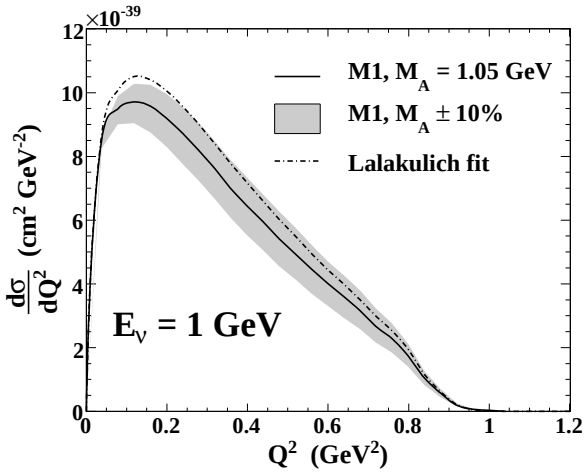

Figure 3.5: Q^2 evolution of the cross section for $\nu_\mu + p \overset{\Delta^{++}}{\rightarrow} \mu^- + p + \pi^+$ at an incoming neutrino energy of 1 GeV. The full (dash-dotted) line corresponds to the vector form-factor parameterization of Eqs. (3.18) and (3.19) (Eq. (3.20)). The shaded region indicates a 10% variation in the axial mass, using the same vector form factors as the full line.

3.1.7 Results and discussion

In this section, we present computations for the process

$$\nu_\mu + p \overset{\Delta^{++}}{\rightarrow} \mu^- + p + \pi^+. \tag{3.39}$$

For scattering off a free nucleon, the strength of the process in Eq. (3.39) can be straightforwardly related to the other channels listed in Eq. (3.2) by applying the isospin relations of Eq. (3.7). Unless otherwise stated, we use the vector form factors of Eqs. (3.18) and (3.19), the axial form factors of Eq. (3.21) with $M_A = 1.05$ GeV, and the $\Delta\pi N$ coupling defined in Eq. (3.33).

The discussion presented here is centered about the elementary Δ couplings and their impact on pion-production cross sections. Figure 3.5 assesses to what extent the extracted value for M_A is sensitive to the specific choice for the vector form factors. To this end, Fig. 3.5 compares the cross section computed with the Lalakulich fit of Eq. (3.20) and $M_A = 1.05$ GeV with the cross section computed with the M1-dominance form factors of Eqs. (3.18) and (3.19) and a 10% variation in the axial mass. In order to reach consistency between the two approaches, the axial mass used in the M1-dominance calculation needs to be 5-10% higher than the one that is used

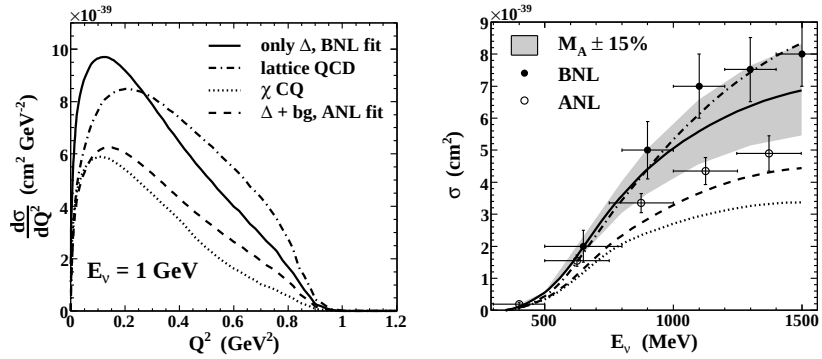

Figure 3.6: Cross sections for $\nu_\mu + p \overset{\Delta^{++}}{\rightarrow} \mu^- + p + \pi^+$ with the $C_5^A(Q^2)$ contained in Fig. 3.4. In the left panel, Q^2 distributions are shown for $E_\nu = 1$ GeV. The dashed line represents a calculation with $C_5^A(0) = 0.867$ and $M_A = 985$ MeV [151]. In the right panel, the shaded region corresponds to a 15% variation in the axial mass. The solid (open) circles show BNL [159] (ANL [165]) total cross-section data.

together with the Lalakulich fit. Consequently, analysing data with the assumption of M1 dominance will generally lead to a 5-10% higher M_A value, compared to an analysis using the Lalakulich fit. This discrepancy is significant, as the vector form factors are often regarded as well known when extracting the poorly-known axial form factors from neutrino scattering data. It also underlines the necessity of re-fitting the axial form factors, once a better parameterization for the vector ones has become available. Indeed, as pointed out in our review of $N - \Delta$ transition form factors, the current situation for the axial-vector form factors is somewhat more dramatic. Figure 3.6 appraises the sensitivity of the Δ-production cross section to different parameterizations for the most important axial transition form factor, $C_5^A(Q^2)$. In the left panel, we contrast computations using a phenomenological result for $C_5^A(Q^2)$ with computations that employ the theoretical calculations shown in Fig. 3.4. Next to the fit to BNL data given in Eq. (3.21), the former involve a fit to ANL data within a model that includes background contributions, in addition to the Δ-pole mechanism [151]. Adopting the same Q^2 dependence as in Eq. (3.21), this leads to $C_5^A(0) = 0.867$ and $M_A = 985$ MeV [151]. Clearly, the Q^2 evolution of the Δ-production cross section exhibits a strong sensitivity to the adopted $C_5^A(Q^2)$ parameterization. Near $Q^2 = 0$, cross sections using the χCQ, QCD and background-model results are about 40% lower than the calculation with the Δ-dominance fit. This is almost entirely due to the difference in $C_5^A(0)$ values, which yields a ratio of $(0.9)^2/(1.2)^2 \approx 0.56$ for the dominant cross-section contribution. The soft $C_5^A(Q^2)$ predicted by the χCQ model results in cross sections that are much lower over the whole Q^2 range. On the other

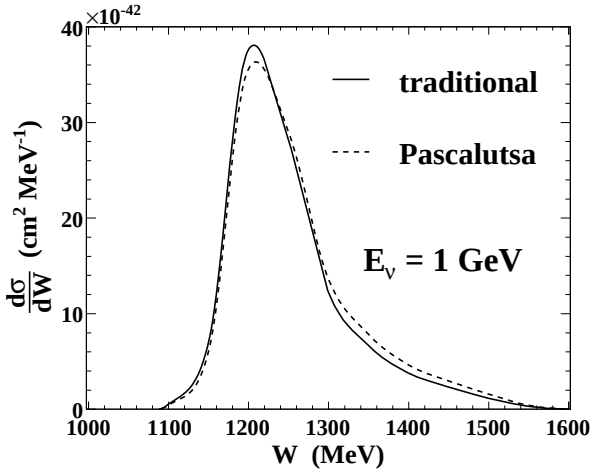

Figure 3.7: Invariant-mass dependence of the cross section for $\nu_\mu + p \overset{\Delta^{++}}{\rightarrow} \mu^- + p + \pi^+$ at an incoming neutrino energy of 1 GeV. The hadronic invariant mass is defined as $W = \sqrt{m_N^2 + 2\omega m_N - Q^2}$. The full (dashed) line uses the $\Delta\pi N$ coupling of Eq. (3.33) (Eq. (3.35)).

hand, the hard C_5^A form factor predicted by the QCD calculation leads to more strength towards higher Q^2 values. The ANL fit for C_5^A results in an integrated cross section that is about 30% lower than the calculation performed with the BNL fit. To put things in a more general perspective, the right panel of Fig. 3.6 makes a comparison between predictions based on different $C_5^A(Q^2)$ parameterizations and the available total cross-section data. The latter mainly come from two bubble-chamber experiments conducted at the Argonne (ANL) [165] and Brookhaven (BNL) [159] national laboratories. First of all, it should be noted that very large differences exist between the two data sets. For neutrino energies around 1 GeV, the BNL data exceed the ANL data by 30%. Within our Δ-dominance model and with the $C_5^A(Q^2)$ parameterization of Eq. (3.21), all data can be reasonably well covered if one admits a $\pm 15\%$ uncertainty on $M_A = 1.05$ GeV. Further, one can see that the lattice-QCD calculation for $C_5^A(Q^2)$ leads to a good description of the BNL cross-section data. On the other hand, the χCQ result underestimates both the BNL and ANL data. Finally, even though no background contributions are included here, the ANL fit for $C_5^A(Q^2)$ [151] only leads to a small underestimation of the ANL data by our Δ-dominance calculation, owing to the large error flags. Hence, we deem that the current status of neutrino-scattering data does not allow an extraction of the axial form-factor parameters to a level better than 20-30%. To investigate the impact of different Δ-decay couplings, we have

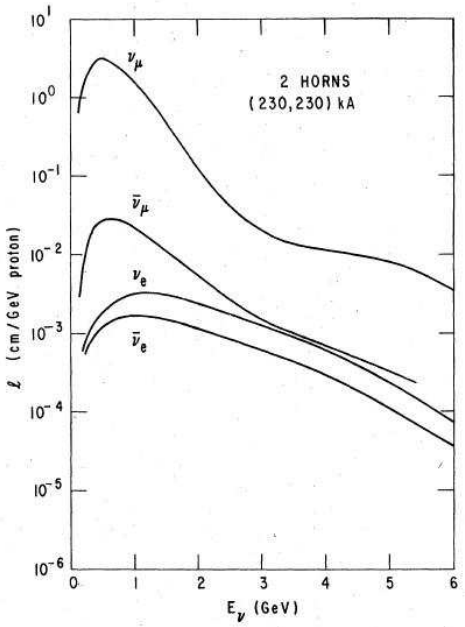

Figure 3.8: ν_μ flux for the ANL two-horn beam configuration, together with $\overline{\nu}_\mu$, ν_e and $\overline{\nu}_e$ backgrounds (graph taken from Ref. [173]). Units are *cm* of target material (H_2 or D_2) traversed by the neutrinos.

computed W-distributions using both the traditional coupling of Eq. (3.33) and the Pascalutsa coupling of Eq. (3.35). The results are shown in Fig. 3.7, where it can be seen that differences between the two approaches are small. Apparantly, the contribution of spurious spin-1/2 terms to Δ-production cross sections is minor. We infer an effect smaller than 2%.
In Fig. 3.9, we compare our calculations for a Q^2 distribution to ANL data. To this end, one must realize that the ANL neutrino beam is not mono-energetic, but rather has a specific energy distribution $\Phi(E_\nu)$ which is shown in Fig. 3.8. Correspondingly, instead of working with a fixed incoming neutrino energy, one should consider the different available energies in the neutrino beam by folding the Q^2 distribution over the neutrino flux like this

$$\langle \frac{d\sigma}{dQ^2} \rangle = \frac{\int_{E_{\nu,min}}^{E_{\nu,max}} \Phi(E_\nu) \frac{d\sigma}{dQ^2}(E_\nu) dE_\nu}{\int_{E_{\nu,min}}^{E_{\nu,max}} \Phi(E_\nu) dE_\nu}. \tag{3.40}$$

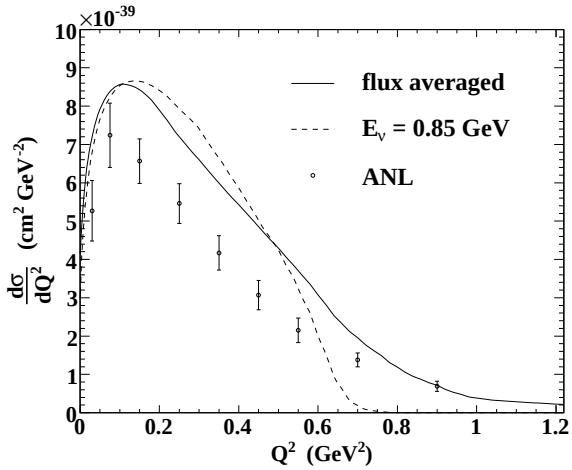

Figure 3.9: Flux-averaged Q^2 distribution $\langle \frac{d\sigma}{dQ^2} \rangle$ (full line) compared to ANL data [165] for the process $\nu_\mu + p \overset{\Delta^{++}}{\rightarrow} \mu^- + p + \pi^+$. A kinematical cut $W < 1.4$ GeV is applied. The dashed line corresponds to an average neutrino energy of $E_\nu = 0.85$ GeV.

This flux-averaged Q^2 distribution, computed with the values $E_{\nu,min} = 0.5$ GeV and $E_{\nu,max} = 6$ GeV, is presented in Fig. 3.9. For comparison, we have also plotted a Q^2 distribution for a fixed $E_\nu = 0.85$ GeV, taken as an estimate for the average neutrino energy in the ANL flux. As the form factors adopted in our model were fitted to BNL data, it is no surprise to see that the calculations overshoot the ANL data. Although the curve for a fixed, average neutrino energy gives a fairly good account of the flux-averaged result, it clearly lacks strength in the high-Q^2 region. Indeed, the wide-band ANL beam allows for a lot of high-energy scattering events, which are only properly included in the flux-averaged cross section of Eq. (3.40). Hence, the exercise sketched here highlights the importance of accurately knowing the incoming-energy distribution when analysing neutrino scattering data. Controlling the systematic uncertainties related to neutrino fluxes is indeed one of the top priorities of running and planned experiments, as it is a prerequisite for extracting any new information.

3.2 Pion production from nuclei

3.2.1 Cross section and super Rosenbluth formula

The extension of the free scattering processes in Eqs. (3.1)-(3.2) and (3.5) to reactions that involve nuclear targets can be written as

$$\nu_\mu + A \xrightarrow{\Delta} \nu_\mu/\mu^- + (A-1) + N + \pi. \tag{3.41}$$

Hereby, it is assumed that both the pion and the nucleon reach the detectors after the Δ has decayed. It should be stressed that very often this will not be the case. Indeed, a produced pion may be re-absorbed in the nuclear medium, or, the created Δ may undergo a pion-less decay triggered by collisions with surrounding nucleons. Clearly, the straightforward one-to-one relation between Δ and one-pion production is lost when considering neutrino-nucleus scattering. We will discuss the consequences of this fact in more detail when dealing with nuclear effects.
Following the same line of reasoning as in section 3.1.2, the lab-frame cross section corresponding to the process of Eq. (3.41) becomes

$$\begin{aligned}\frac{d^8\sigma}{dE_l d\Omega_l dE_\pi d\Omega_\pi d\Omega_N} =& \frac{m_\nu m_l |\vec{k}_l| m_N m_{A-1} |\vec{k}_\pi||\vec{k}_N|}{2(2\pi)^8 E_\nu |E_{A-1} + E_N + E_N \vec{k}_N \cdot (\vec{k}_\pi - \vec{q})/|\vec{k}_N|^2|} \\ & \times \overline{\sum}_{fi} \left| M_{fi}^{(bound)} \right|^2 .\end{aligned} \tag{3.42}$$

Just like for QE νA scattering, one can work out a Rosenbluth separation scheme for the considered $A(\nu, l\pi N)A-1$ process. Following the general method outlined by Donnelly [45], the hadronic tensor $H^{\mu\nu}_{(bound)}$ can be constructed from the following independent four-momenta

$$q^\mu, k_A^\mu, k_\pi^\mu \text{ and } k_N^\mu. \tag{3.43}$$

In the laboratory system, the response functions accompanying each term of the hadronic tensor then depend on only seven independent variables,

$$\omega, |\vec{q}|, E_\pi, \theta_\pi, E_N, \theta_N \text{ and } \Delta\phi, \tag{3.44}$$

where $\Delta\phi = \phi_\pi - \phi_N$ denotes the difference of the azimuthal angles ϕ_π and ϕ_N. Similarly, the average azimuthal angle is defined as

$$\phi = \frac{\phi_\pi + \phi_N}{2}. \tag{3.45}$$

Developing the contraction of the lepton tensor $L_{\mu\nu}$, given in Eq. (2.12), with the hadron tensor $H^{\mu\nu}_{(bound)}$, one arrives at a decomposition of the form

$$\begin{aligned}\overline{\sum_{fi}}\left|M^{(bound)}_{fi}\right|^2 \sim\ & L_{\mu\nu}H^{\mu\nu}_{(bound)} \\ =\ & v_L R_L \\ &+ v_T R_T + v_{TT}(R_{TT,a}\cos 2\phi + R_{TT,b}\sin 2\phi) \\ &+ v^{(1)}_{LT}(R^{(1)}_{LT,a}\cos\phi + R^{(1)}_{LT,b}\sin\phi) \\ &+ v^{(2)}_{LT}(R^{(2)}_{LT,a}\cos\phi + R^{(2)}_{LT,b}\sin\phi) \\ &+ v_{T'}R_{T'} \\ &+ v^{(1)}_{LT'}(R^{(1)}_{LT',a}\cos\phi + R^{(1)}_{LT',b}\sin\phi) \\ &+ v^{(2)}_{LT'}(R^{(2)}_{LT',a}\cos\phi + R^{(2)}_{LT',b}\sin\phi).\end{aligned} \tag{3.46}$$

The relations between the longitudinal (L), transverse (T, TT, T') and interference (LT, LT') nuclear responses in Eq. (3.46) and the components of the hadron tensor read

$$\begin{aligned} v_L R_L &= L_{00}H^{00}_{(bound)} + L_{0z}2\Re(H^{0z}_{(bound)}) + L_{zz}H^{zz}_{(bound)} \\ R_T &= H^{xx}_{(bound)} + W^{yy}_{(bound)} \\ R_{TT,a}\cos 2\phi + R_{TT,b}\sin 2\phi &= H^{xx}_{(bound)} - W^{yy}_{(bound)} \\ R^{(1)}_{LT,a}\cos\phi + R^{(1)}_{LT,b}\sin\phi &= 2\Re(H^{0x}_{(bound)}) \\ R^{(2)}_{LT,a}\cos\phi + R^{(2)}_{LT,b}\sin\phi &= 2\Re(H^{xz}_{(bound)}) \\ R_{T'} &= 2i\Im(H^{xy}_{(bound)}) \\ R^{(1)}_{LT',a}\cos\phi + R^{(1)}_{LT',b}\sin\phi &= 2i\Im(H^{0y}_{(bound)}) \\ R^{(2)}_{LT',a}\cos\phi + R^{(2)}_{LT',b}\sin\phi &= 2i\Im(H^{yz}_{(bound)}). \end{aligned} \tag{3.47}$$

The value of the super Rosenbluth expression (3.46) lies in the fact that all responses R depend on $\Delta\phi$, but not on ϕ. As pointed out in Ref. [45], this factorization of angular dependencies enables a separation of the individual terms figuring in Eq. (3.46). Disentangling different responses is indeed deemed desirable, since each of the contributions has different sensitivities to particular information of the pion-production process. Consequently, the Rosenbluth separation scheme has been aptly used in electron-scattering studies [174]. To the contrary, neutrino experiments do not have the discriminative power to map out the angular distributions. Nevertheless, the super Rosenbluth formula is also useful here, as it allows the integration over ϕ to be performed analytically. Eventually, this amounts to an inclusive cross section that is fully determined by R_L, R_T and $R_{T'}$.

3.2.2 RPWIA and closed cross-section formula

The invariant matrix element in Eq. (3.42) carries the tag *bound* and involves nuclear currents between initial and final nuclear wave functions. Just like in the QE case, however, one usually resorts to a number of assumptions that allow a reduction of the nuclear-current matrix elements to a form similar to Eq. (3.12). Here, we summarize the main approximations that enable this simplification and refer to section 2.2 for more detailed considerations. First, we only consider processes where the residual $(A-1)$ system is left with an excitation energy not exceeding a few tens of MeV. The major fraction of the transferred energy is carried by the outgoing pion and nucleon. Further, we adopt the impulse approximation: the nuclear many-body current is replaced by a sum of one-body current operators, exempt from medium effects. Assuming an independent-particle model for the nuclear wave functions, the hadronic current matrix elements can then be written in the form of Eq. (3.12), whereby the initial-nucleon free Dirac spinor is replaced by a bound-state spinor. Using the single-particle wave functions introduced in section 2.4.1, and writing $\mathscr{U}_{\alpha,m}(\vec{p})$ for the corresponding bound-state spinors, one has

$$\langle J^{\mu}_{(bound)} \rangle = \overline{u}(k_N, s_N) \mathscr{O}^{\mu} \mathscr{U}_{\alpha,m}(\vec{p}), \tag{3.48}$$

where $\mathscr{O}^{\mu} = \Gamma^{\rho}_{\Delta\pi N} S_{\Delta,\rho\sigma} \Gamma^{\sigma\mu}_{WN\Delta}$ is the one-body current operator for the elementary Δ-mediated one-pion production process. With Eq. (3.48), the nuclear hadron tensor is explicitly given by

$$\begin{aligned} H^{\mu\nu}_{(bound)} &= \frac{1}{2j+1} \sum_{m;s_N} \langle J^{\mu}_{(bound)} \rangle^{\dagger} \langle J^{\nu}_{(bound)} \rangle \\ &= \mathrm{Tr} \left(S_{\alpha}(\vec{p}) \widetilde{\mathscr{O}}^{\mu} \frac{(\not{k}_N + m_N)}{2m_N} \mathscr{O}^{\nu} \right), \end{aligned} \tag{3.49}$$

where $\widetilde{\mathscr{O}}^{\mu}$ is short for $\gamma_0 (\mathscr{O}^{\mu})^{\dagger} \gamma_0$. In Eq. (3.49), we introduced the bound-state propagator $S_{\alpha}(\vec{p})$, defined as

$$S_{\alpha}(\vec{p}) = \frac{1}{2j+1} \sum_{m} \mathscr{U}_{\alpha,m}(\vec{p}) \overline{\mathscr{U}}_{\alpha,m}(\vec{p}). \tag{3.50}$$

As pointed out in section 2.4.1, the bound-state propagator can be cast in a form similar to the Dirac projection operator (Eqs. (2.52) and (2.53)). In this manner, one can write down a closed form for the squared invariant matrix element related to Δ-mediated one-pion production from nuclei [175],

$$\overline{\sum_{fi}} \left| M^{(bound)}_{fi} \right|^2 = \frac{G_F^2 \cos^2\theta_c M_W^4}{2(M_W^2 + Q^2)^2} H^{\mu\nu}_{(bound)} L_{\mu\nu}. \tag{3.51}$$

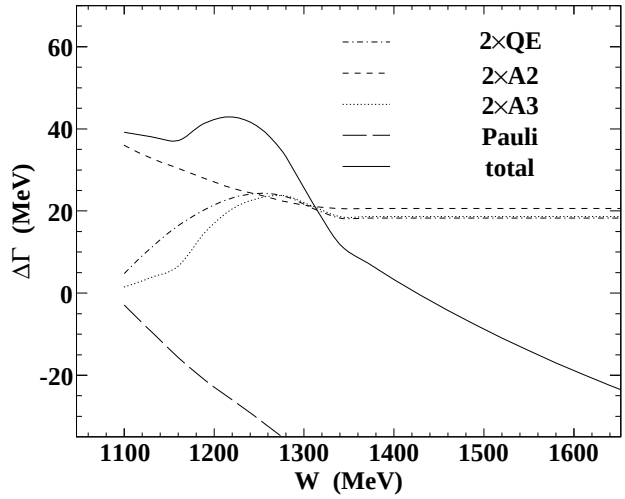

Figure 3.10: Overview of medium corrections to the free Δ width, using the parameterizations in Refs. [29, 176] for $\rho = 0.75\rho_0$.

Evidently, Eq. (3.51) holds for CC scattering. For NC reactions, the following substitutions are in order: $\cos^2\theta_c \to 1$ and $M_W^2 \to M_Z^2$. Furthermore, it is assumed that both the pion and the nucleon remain unaffected by the medium, implying that Eq. (3.51) refers to the relativistic plane-wave impulse approximation. Note that Eq. (3.51) is readily found from the free-nucleon expression in Eq. (3.13) by making the replacement

$$\frac{1}{2}\frac{(\not{k}_{N,i} + m_N)}{2m_N} \longrightarrow (2\pi)^3 S_\alpha(\vec{p}). \tag{3.52}$$

For neutrino-nucleus scattering, the substitution of Eq. (3.52) ensures the natural inclusion of Fermi-motion and nuclear-binding effects.

3.2.3 Medium modifications of Δ properties

In a nuclear environment, the Δ mass and width are modified with respect to their free values. These medium modifications can be estimated by calculating the in-medium Δ self-energy, as was e.g. done in Ref. [29]. The real part of the Δ self-energy causes a shift of the resonance position, whereas the imaginary part is related to the decay width. Medium modifications for the width result from the competition between a Pauli-blocking correction, reducing the free decay width, and a term proportional to the imaginary part of the Δ self-energy, including various meson and

baryon interaction mechanisms and, therefore, enhancing the free decay width. Writing $\widetilde{\Gamma}$ for the in-medium Δ width, one has

$$\widetilde{\Gamma} = \Gamma_{\text{Pauli}} - 2\,\Im(\Sigma_\Delta), \tag{3.53}$$

with Σ_Δ the Δ self-energy. In terms of the free decay width Γ, the width corrected for Pauli-blocking effects is given by

$$\Gamma_{\text{Pauli}} = \frac{I_1 + I_2}{2}\Gamma, \tag{3.54}$$

where an explicit expression for the integrals I_1 and I_2 is provided in Ref. [176]. A convenient parameterization of the imaginary part of Σ_Δ is given in Ref. [29], as a function of the nuclear density ρ,

$$-\Im(\Sigma_\Delta) = C_{QE}\left(\frac{\rho}{\rho_0}\right)^\alpha + C_{A2}\left(\frac{\rho}{\rho_0}\right)^\beta + C_{A3}\left(\frac{\rho}{\rho_0}\right)^\gamma, \tag{3.55}$$

where $\rho_0 = 0.17$ fm^{-3} is the saturation density in finite nuclei. The terms with the coefficients C_{QE}, C_{A2} and C_{A3} correspond to the processes $\Delta N \to \pi NN$, $\Delta N \to NN$ and $\Delta NN \to NNN$ respectively. Whereas C_{QE} enhances the number of Δ decays with a pion, the latter two contributions open up pion-less decay channels through two- and three-body absorption mechanisms. The values of C_{QE}, C_{A2}, C_{A3}, α, β and γ can be found in Refs. [29, 176], where they are given as a function of the energy E_π of a pion that would excite a Δ with $W^2 = m_\pi^2 + m_N^2 + 2E_\pi m_N$. Medium corrections to the Δ mass assume the form

$$\widetilde{M}_\Delta = M_\Delta + \Re(\Sigma_\Delta), \tag{3.56}$$

with [177]

$$\Re(\Sigma_\Delta) = 40 \text{ MeV}\,\frac{\rho}{\rho_0}. \tag{3.57}$$

The parameterizations in Eqs. (3.55) and (3.57) are particularly useful when used in conjunction with a local density approximation for the nucleus. In position space, the dependence of the width corrections on the nuclear density $\rho(\vec{r})$ can be accounted for by folding over the nuclear volume. On the other hand, for RPWIA calculations in momentum space, the integrations $\int d\vec{r}$ are converted to delta functions expressing momentum conservation, rendering the application of density-dependent Δ medium modifications impossible. Therefore, for our purposes, we shall adopt an *effective* nuclear density $\rho = 0.75\rho_0$. Figure 3.10 plots the different corrections to the free Δ decay width for this density value. The bumps at $W \sim 1150$ MeV arise from different parameterizations of the C_{A3} term for $T_\pi < 85$ MeV [176] and $T_\pi > 85$ MeV [29]. Beyond $T_\pi = 315$ MeV, we keep the medium corrections fixed at their value for

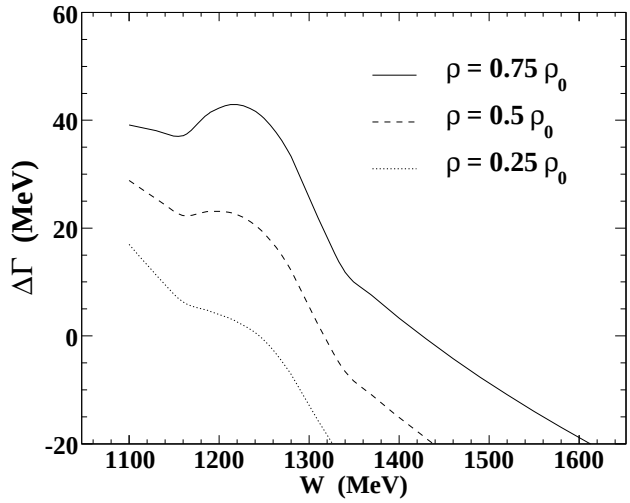

Figure 3.11: Total medium correction $\Delta\Gamma = \widetilde{\Gamma} - \Gamma$, using the parameterizations in Refs. [29, 176] at different nuclear densities.

$T_\pi = 315$ MeV. At the Δ peak, we infer the following shifts

$$\begin{aligned} M_\Delta &\longrightarrow M_\Delta + 30 \text{ MeV}, \\ \Gamma &\longrightarrow \Gamma + 40 \text{ MeV}. \end{aligned} \tag{3.58}$$

One could object that the scheme (3.58) for Δ medium modifications is guided by an unrealistically-high average value for the probed nuclear density, leading to a strong overestimation of the effect. There exists some evidence, though, to back up the values in Eq. (3.58). In Ref. [178], a similar recipe was used to accommodate medium modifications in the calculation of $^{12}\mathrm{C}(\gamma, pn)$ and $^{12}\mathrm{C}(\gamma, pp)$ cross sections. There, the computations proved to compare favorably with the data in an energy regime where the reaction is dominated by Δ creation. It is worth stressing that photo-induced two-nucleon knockout reactions receive very small contributions from background diagrams, who form an important source of uncertainties when extracting resonance information. Hence, we consider Eq. (3.58) to be a reliable estimate for Δ medium modifications. It is very instructive, however, to assess the density dependence of the medium corrections to the Δ width. In Fig. 3.11, we therefore show $\Delta\Gamma = \widetilde{\Gamma} - \Gamma$ at various values for the nuclear density ρ. As one can appreciate, density dependences are sizeable. At the Δ peak, we infer $\Delta\Gamma = 40, 20, 0$ MeV for $\rho = 0.75\rho_0$, $0.5\rho_0$, $0.25\rho_0$, respectively.

3.2.4 FSI effects

Computing FSI effects for pion-production processes presents itself as extremely challenging. Once a pion is produced, it will generally undergo a number of elastic or/and inelastic scatterings with the remaining nucleons in the rest nucleus. These rescatterings can lead to the absorption of the pion. Through charge exchanges, the pion may leave the nucleus in a different charge state. Or, in case it does manage to escape from the nucleus, the pion's energy and scattering angle may have changed. In an effort to estimate the effect of charge-exchange and absorption mechanisms, Paschos and collaborators [39, 179] have applied the Adler-Nussinov-Paschos pion multiple-scattering model [180] to compute *charge-exchange matrices*, which relate initial (π^+, π^0, π^-) distributions to final ones. Another model [40] employs a Monte-Carlo simulation method [181] to deal with the complex, multi-channel pion rescatterings. Recently, the Giessen group has applied its semi-classical, coupled-channel transport model to neutrino-induced pion production from nuclei [41, 149]. All the mentioned studies report very large FSI effects due to pion rescatterings inside nuclear targets.
In addition, it has become quite clear that a complete, quantum-mechanical description of the involved inelasticities is impossible to achieve. Along the same lines, the Glauber model introduced in the previous chapter to compute the *elastic* nucleon-knockout contribution to QE neutrino scattering can not give a full account of pion-rescattering mechanisms either. Instead, the RMSGA provides a quantum-mechanical framework in which the nuclear attenuation of a fast pion ($T_\pi \gtrsim 700$ MeV) can be computed. The procedure to do so is very similar to the one outlined in section 2.4.2. All detailed considerations can be found in Ref. [182]. Put simply, the Glauber approach allows to predict what fraction of the originally produced pions and nucleons (from the Δ decay) will effectively reach the detectors. Unlike the cascade models, however, the RMSGA does not keep track of the inelastic channels corresponding to the predicted loss of flux.

3.2.5 Results and discussion

In this section, we present computations for the process

$$\nu_\mu + A \overset{\Delta^{++}}{\rightarrow} \mu^- + (A-1) + p + \pi^+. \tag{3.59}$$

It is important to note that, in νA scattering, the isospin relations of Eq. (3.7) can no longer be applied to derive the strength of the isospin-related channels. Indeed, once pion rescatterings are considered, charge-exchange mechanisms can affect the ratios between the pionic final states [41].
We stick to the standard input values for the Δ couplings: the vector form factors of Eqs. (3.18) and (3.19), the axial form factors of Eq. (3.21) with $M_A = 1.05$ GeV, and

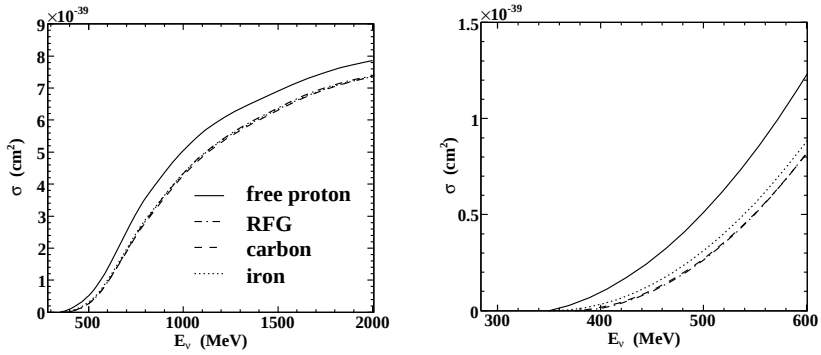

Figure 3.12: Total cross sections per proton for $\nu_\mu + p \overset{\Delta^{++}}{\rightarrow} \mu^- + p + \pi^+$. The full line represents the elementary process, for scattering from a free proton. The dash-dotted line stands for the RFG calculations, whereas the dashed (dotted) line corresponds to scattering from a carbon (iron) target nucleus. The right panel focusses on the threshold region.

the $\Delta\pi N$ coupling of Eq. (3.33). For a comparison of RPWIA and RFG calculations, we adopt $k_F = 225$ MeV and an average binding energy of $E_b = 20$ MeV. The latter value can be considered as a fair estimate for the weighted average of the centroids of the single-particle strength distributions in typical even-even nuclei near the closed shells [183].

Nuclear-model effects - RPWIA vs RFG

In this discussion, the results of section 3.1.7 will be put in a more general perspective. To this end, we will compare neutrino-nucleus with neutrino-nucleon cross sections. Figure 3.12 shows how the total $\nu_\mu + p \overset{\Delta^{++}}{\rightarrow} \mu^- + p + \pi^+$ strength varies with the incoming neutrino energy. With similar input, our results for the elementary process compare very well with the predictions published in Ref. [151]. The cross sections for target nuclei were computed along the lines of section 3.2.2, i.e. using the closed RPWIA cross-section formula without Δ medium modifications and FSI effects. Turning to Fig. 3.12, it is seen how the elementary cross section is halved near threshold. For higher incoming energies, the effect dwindles to 20% at $E_\nu = 800$ MeV and 8% at $E_\nu = 2$ GeV. The RFG calculations are in good to excellent agreement with both the carbon and iron RPWIA results. The only discernable feature of Fig. 3.12 is that the iron curve exceeds the carbon and RFG ones by roughly 15% just beyond threshold. This can be readily understood after recognizing that the nucleon separation energy is larger for carbon than for iron. Also, the adopted binding-energy value for the

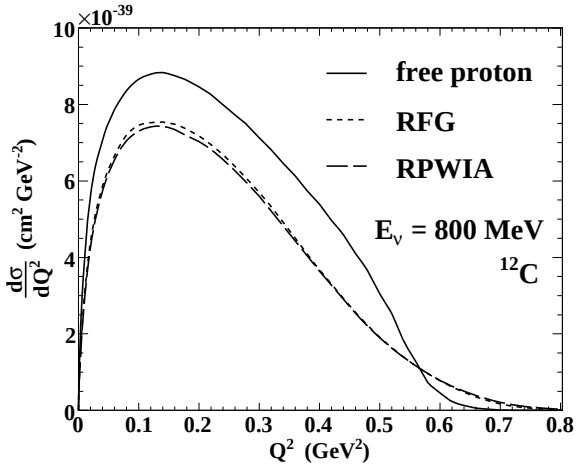

Figure 3.13: Cross section per proton for $\nu_\mu + p \overset{\Delta^{++}}{\rightarrow} \mu^- + p + \pi^+$ on carbon at an incoming neutrino energy of 800 MeV. The full line represents the elementary process, whereas the short-dashed (long-dashed) line stands for the RFG (RPWIA) calculation.

RFG calculations is close to the weighted binding energy per nucleon in a carbon nucleus, explaining the close agreement between these two cases. Clearly, the $\nu_\mu A$ cross sections are very sensitive to binding-energy differences at lower incoming energies. These effects, however, vanish at higher neutrino energies and are of the order of 1% at $E_\nu = 1$ GeV. As a matter of fact, at sufficiently high energies RFG calculations with a well-chosen binding-energy correction are almost indiscernible from the corresponding RPWIA results. These findings are more detailedly assessed in Figs. 3.13, 3.14 and 3.15. Figures 3.13 and 3.14 compare RFG and RPWIA computations. The former considers scattering from a carbon target at $E_\nu = 800$ MeV, which corresponds to the mean energy of the neutrino beam used by the MiniBooNE experiment. As can be appreciated from Fig. 3.13, the RFG and RPWIA models produce almost identical results. In Fig. 3.14, we present the ratio of RFG to carbon RPWIA results for the twofold cross section $d^2\sigma/dT_\pi d\cos\theta^*_\pi$, where T_π is the pion's kinetic energy and θ^*_π its direction relative to the neutrino-beam. In the threshold region, cross sections are extremely small and subject to large fluctuations. Beyond threshold, however, differences between the RFG and RPWIA result do not exceed the 5% level over the whole (T_π, θ^*_π) range. Consequently, upon integrating over T_π and θ^*_π, we find that the total RFG cross section exceeds the RPWIA one by about 2%. Figure 3.15 compares the cross section for a carbon nucleus with the one for an iron nucleus at $E_\nu = 1.5$ GeV. Although the total strength, integrated over the outgoing muon energy E_l, is the same

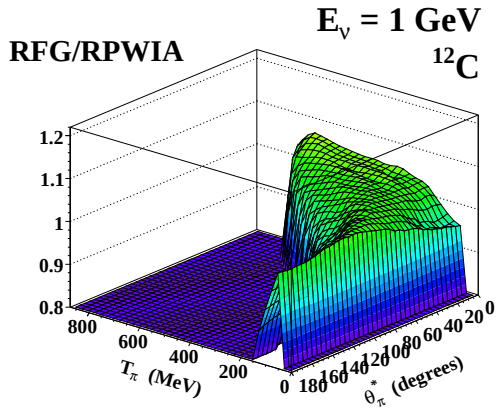

Figure 3.14: Ratio of RFG to RPWIA computations for the $d^2\sigma/dT_\pi d\cos\theta^*_\pi$ cross section of the process $\nu_\mu + p \overset{\Delta^{++}}{\rightarrow} \mu^- + p + \pi^+$. A carbon target and an incoming neutrino energy of 1 GeV are considered.

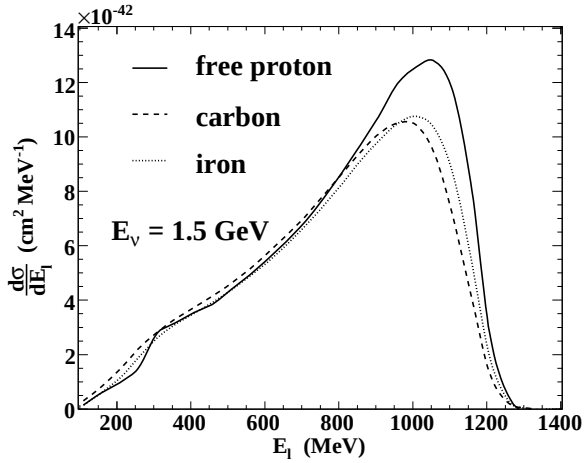

Figure 3.15: The $\nu_\mu + p \overset{\Delta^{++}}{\rightarrow} \mu^- + p + \pi^+$ cross section per proton as a function of the outgoing-lepton energy E_l for $E_\nu = 1.5$ GeV. The full line represents the elementary process, whereas the dashed (dotted) line refers to scattering from carbon (iron).

for both nuclei, it is interesting to note that the iron cross section is shifted with respect to the carbon one. Again, this reflects the fact that on average it requires more energy to knock a proton out of a carbon nucleus than out of an iron nucleus, leaving therefore less energy for the outgoing muon.

Primary pion production and inclusive observables

Like for QE scattering, we wish to test our model for Δ-mediated one-pion production against inclusive electron-nucleus scattering data. To this end, in Fig. 3.16, we compare RPWIA calculations for *primary* one-pion production to $^{16}\mathrm{O}(e,e')$ data from Ref. [110]. The term *primary* relates to pion production before rescatterings. As the intermediate Δ resonance is created inside an oxygen nucleus, we apply the medium modifications of Eq. (3.58) in the denominator of the Δ propagator. For comparison, we have included Δ-production calculations performed in the framework of Lalakulich et al. [184], using the same nuclear-physics input as the RPWIA calculations presented here. In the formalism of Ref. [184], the inclusive Δ-production cross section is proportional to the free width,

$$\frac{d^3\sigma}{dE_l d\Omega_l} \sim \frac{\Gamma}{(W^2 - M_\Delta^2)^2 + M_\Delta^2\Gamma^2} \tag{3.60}$$

Hence, when including medium effects, the one-pion contribution (*1-*π) can be separated from the full, inclusive cross section (*incl*) by adding only those corrections relating to the pion decay channel to the width in the numerator of Eq. (3.60) [40, 185, 186]. Using the parameterizations for the C_{QE} term and Pauli correction discussed in section 3.2.3, with $\rho = 0.75\rho_0$ and at the Δ peak, we find that the free decay width receives no appreciable medium corrections with respect to the one-pion decay channel. So, the full and one-pion computations in Fig. 3.16 are obtained by applying the medium modifications of Eq. (3.58) in the denominator and, at the same time, adding the values of 40 MeV (incl) and 0 MeV (1-π) to the width in the numerator of Eq. (3.60). Compared to the data, the peak of the computed cross sections is moved towards higher energy transfers. Moreover, the inclusive strength in the Δ region is underestimated. These observations may point to the importance of non-resonant background contributions [42], which are not taken into account here. Contrasting both of the Lalakulich calculations, it is seen that the one-pion contribution comprises about 75-80% of the full inclusive result. The remainder of the strength resides in pion-less decay modes, which have become available as additional decay channels due to two- and three-body absorption processes such as $\Delta N \to NN$ and $\Delta NN \to NNN$. On the other hand, the major difference between the one-pion calculation by Lalakulich and the ones presented in this thesis lies in the Δ propagator and the presence of a $\Delta\pi N$ decay vertex in our formalism. Using the free value $f_{\pi N\Delta} = 2.21$, it is observed that our result for primary one-pion production agrees

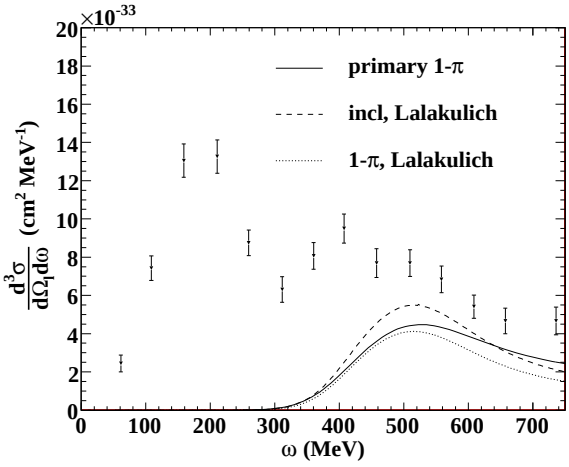

Figure 3.16: Comparison of cross-section calculations to inclusive electron-scattering data. Shown is $d^3\sigma/d\Omega_l d\omega$ against energy transfer ω, for scattering off ^{16}O at $E_e =$ 1080 MeV and $\theta_{e'} = 32$ degrees. The full line represents the primary Δ-mediated one-pion production strength, as computed in our RPWIA model with Δ medium modifications. The dashed (dotted) line denotes a calculation of Δ production (the one-pion part of Δ production) carried out in the framework of Ref. [184]. Data are from Ref. [110, 187].

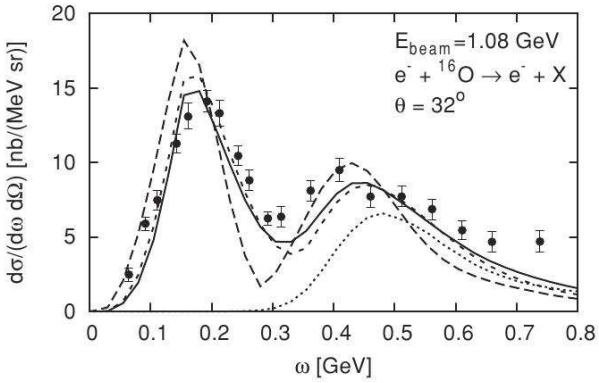

Figure 3.17: Inclusive electron-scattering calculations by Buss et al. (Ref. [42]). The dotted line represents the inclusive Δ-production strength. Figure taken from Ref. [42].

well with the Lalakulich one-pion result for energy transfers up to the Δ peak. For larger ω, however, both of the Lalakulich calculations are considerably smaller. There, the explicit inclusion of the $\Delta\pi N$ decay vertex and the detailed treatment of the Δ propagator (instead of the Breit-Wigner form used in Ref. [184]) seem to account for a better agreement with data. Although our calculation for primary one-pion production could never be measured as a separate contribution in the Δ region, it can be safely concluded that it gives a fair estimate of the Δ-mediated one-pion yield.

Other theoretical efforts on inclusive lepton scattering off nuclei include for example the work presented in Ref. [42]. There, the nucleus is described as a local Fermi gas of nucleons. The lepton-nucleus interaction is treated in the IA, and special attention is paid to including in-medium effects on the pion-production mechanisms. Figure 3.17 shows the total Δ-production contribution (dotted line) for electron scattering off an oxygen target at the same kinematics as in Fig. 3.16. Compared to the one-pion calculations presented here, one can see that the inclusion of pion-less decay modes shifts the peak of the Δ contribution to lower energy transfers. Indeed, since no pion needs to be created, the pion-less decay modes contribute strength in the low W ($\sim$ low ω) region.

In view of recent results presented by the MiniBooNE and K2K collaborations, we conclude this paragraph with some computations for the specific neutrino energies and target nuclei employed by these experiments. From an experimental viewpoint, the most accessible distributions are the ones with respect to outgoing-muon variables. Fig. 3.18 depicts an RPWIA calculation, including Δ medium modifications,

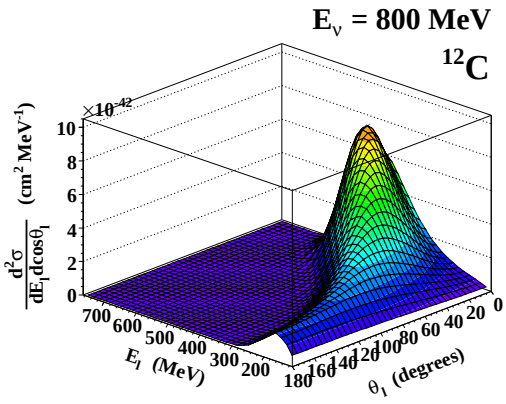

Figure 3.18: Cross section per proton for $\nu_\mu + p \overset{\Delta^{++}}{\rightarrow} \mu^- + p + \pi^+$ as a function of outgoing-muon energy and scattering angle. The incoming neutrino energy is 800 MeV, the target nucleus is carbon.

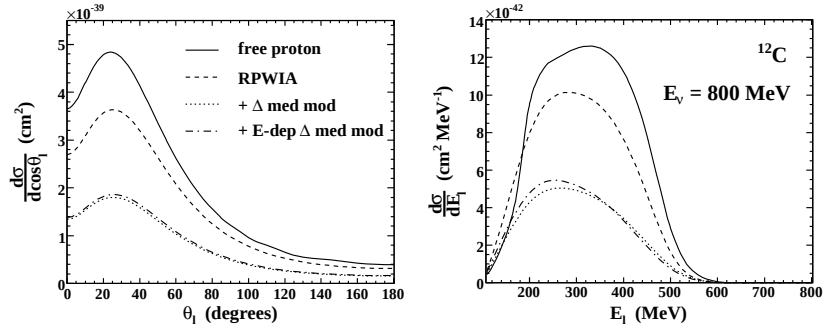

Figure 3.19: Cross sections per proton for $\nu_\mu + p \overset{\Delta^{++}}{\rightarrow} \mu^- + p + \pi^+$, for 800 MeV neutrinos scattering from a carbon target. The left (right) panel shows the cross section as a function of the outgoing-muon scattering angle (energy). Each of the panels contrasts the elementary cross section (full line) with RPWIA results, applying constant (dotted), energy-dependent (dash-dotted) or no (dashed) Δ medium modifications.

for a two-fold differential cross section against the outgoing-muon energy and scattering angle with respect to the neutrino beam. The incoming neutrino energy is fixed at 800 MeV, corresponding to MiniBooNE's mean beam energy. Since MiniBooNE has carbon as target material, this calculation was performed on a carbon nucleus. The result shown in Fig. 3.18 can be integrated over θ_l or E_l to yield the one-fold cross sections displayed in Fig. 3.19. For comparison, we have also computed the free cross section and the basic RPWIA one, for which no Δ medium modifications are included. Relative to the free cross section, the RPWIA angular distribution is reduced by about 20%. In general, the outgoing muon prefers a forward direction. A minor angular shift between the free and the bound case is observed. This effect relates to the change in the muon-energy distribution, depicted in the right-hand panel of Fig. 3.19. Indeed, for scattering off bound protons, one observes a shift of the E_l distribution towards lower values. Recognizing the correlation between high muon energies and forward scattering angles, as can be appreciated in Fig. 3.18, the bound case will correspondingly yield a larger number of events at slightly higher scattering angles. We also note that the RPWIA result fades out sooner than the elementary cross section, because a certain amount of energy is needed to knock the carbon proton out of its shell. Further, Fig. 3.19 shows that the inclusion of Δ medium modifications results in a 50% reduction of the basic RPWIA results. In addition, we have looked into the effect of energy-dependent medium modifications relatively to our standard scheme which involves adding a constant 40 MeV to the free decay width. To do so, we have used the energy-dependent parameterizations found in Refs. [29, 176]. As can be appreciated, the angular distribution in Fig. 3.19 is hardly affected by this more detailed treatment of Δ medium modifications. Likewise, the effect on the muon-energy cross section is mild and does not extend beyond the few-percent level. The muon-energy distribution is also observed to be shifted towards lower E_l, by an amount that corresponds to the mass shift in Eq. (3.58). In Ref. [185], a similar effect is observed in the case of electron-neutrinos scattering off oxygen. Figure 3.20 shows the calculations by Singh et al. [185]. It is seen that medium-modification effects lead to a $\sim 40\%$ reduction of Δ-mediated one-pion production. Furthermore, a distinction is made between the inclusive Δ-production cross section (full line) and the fraction of Δs that eventually produces pions (short-dashed line). From Fig. 3.20, one infers that only $\sim 80\%$ of the Δs, that are created inside an oxygen nucleus, produce pions. The rest is categorized as QE-like, because of the pion-less decay modes it corresponds to. From their results, it also follows that these QE-like events mainly contribute in the region of high outgoing-lepton energy. These findings corroborate our previous results for inclusive electron scattering.

Planned experiments like MINERνA are designed to achieve a good energy resolution for both the muon and the produced hadrons. The ability to detect the outgoing pion or nucleon or even both would allow a detailed study of different nuclear effects. In Figs. 3.21 and 3.22, we present cross sections versus the pion kinetic energy T_π and

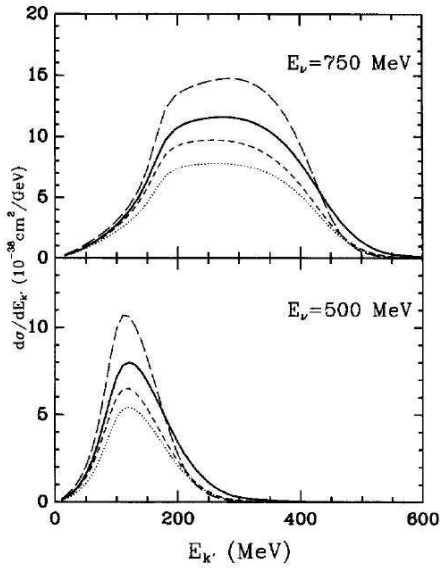

Figure 3.20: Δ-production cross sections against scattered-electron energy, as computed by Singh et al. (Ref. [185]) for CC ν_e scattering from ^{16}O. The long-dashed (full) curve corresponds to inclusive Δ production, without (with) medium modifications. The short-dashed curve represents the pion-production part of the full curve. Figure taken from Ref. [185].

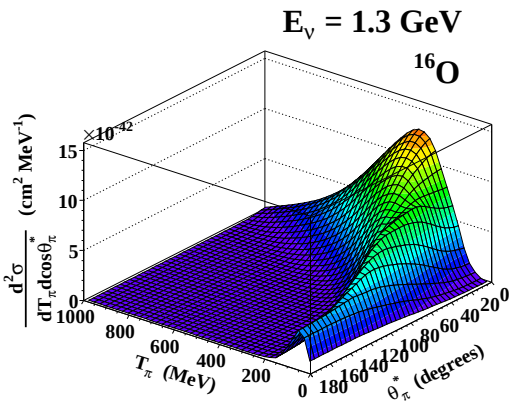

Figure 3.21: Cross section per proton for $\nu_\mu + p \overset{\Delta^{++}}{\rightarrow} \mu^- + p + \pi^+$ against outgoing-pion kinetic energy and scattering angle. The incoming neutrino energy is 1.3 GeV, the target nucleus is oxygen.

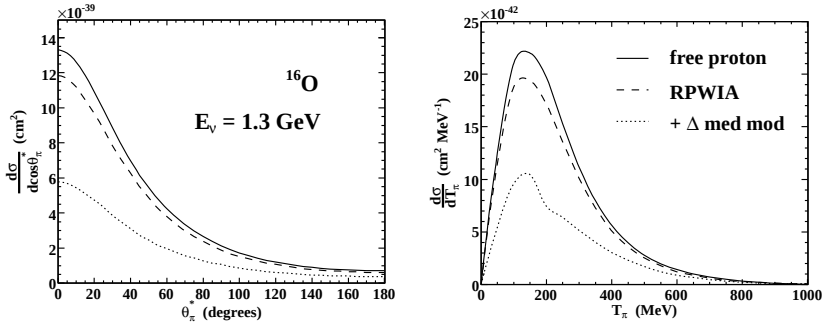

Figure 3.22: Cross sections per proton for $\nu_\mu + p \overset{\Delta^{++}}{\rightarrow} \mu^- + p + \pi^+$, for 1.3 GeV neutrinos scattering from an oxygen target. The left (right) panel shows the cross section as a function of the outgoing-pion scattering angle (kinetic energy). Each panel contrasts the elementary cross section (full line) with the RPWIA result, with (dotted) and without (dashed) Δ medium modifications.

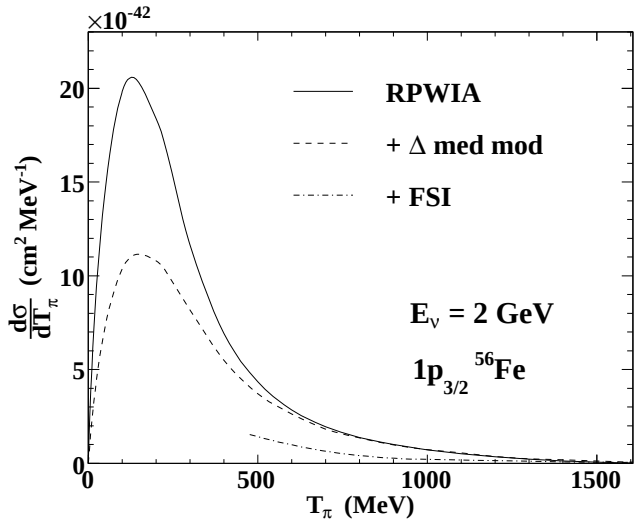

Figure 3.23: Study of nuclear effects on the pion kinetic-energy distribution describing the process $\nu_\mu + p \overset{\Delta^{++}}{\rightarrow} \mu^- + p + \pi^+$ for a $1p_{3/2}$ ^{56}Fe proton and an incoming neutrino energy of 2 GeV. The full line represents the basic RPWIA result, the dashed and dash-dotted curves additionally include the effect of Δ medium modifications and FSI mechanisms.

pion scattering angle relative to the beam direction θ^*_π. This time, we adopted K2K settings, namely an oxygen target hit by neutrinos with an energy of 1.3 GeV. From the left-hand panel of Fig. 3.22, one infers that, within the RPWIA model, the outgoing pion prefereably leaves the nucleus along the beam direction. As for the kinetic-energy distribution, we observe a comparable reduction and shift of the strength as in the muon-energy distribution.

FSI effects

At the end of this results section, in Fig. 3.23, we present a study of FSI effects for the production of a pion on a proton in the $1p_{3/2}$ shell of an iron nucleus. To estimate the effect of FSI mechanisms, we closely follow the lines of Ref. [182]. There, recognizing that negative-energy terms give very small contributions for $|\vec{p}_m| \leq 300$ MeV, a factorized approach is achieved by neglecting the lower components of the bound-state wave functions. Under these conditions, it is shown [182] how the RMSGA cross

section can be obtained by folding the RPWIA one over the transparency function

$$\mathcal{T}(\vec{p}_m) = \frac{\rho^{\alpha}_{RMSGA}(\vec{p}_m)}{\rho^{\alpha}(\vec{p}_m)}. \tag{3.61}$$

Thereby, the distorted momentum distribution ρ^{α}_{RMSGA} is defined as

$$\rho^{\alpha}_{RMSGA}(\vec{p}_m) = \sum_{m,m_s} \left| \overline{u}(\vec{p}_m, m_s) \mathcal{W}^{D}_{\alpha,m}(\vec{p}_m) \right|^2, \tag{3.62}$$

with the distorted momentum-space wave function given by

$$\mathcal{W}^{D}_{\alpha,m}(\vec{p}_m) = \frac{1}{(2\pi)^{3/2}} \int d\vec{r} e^{-i\vec{p}_m \cdot \vec{r}} \Psi_{\alpha,m}(\vec{r}) \mathcal{G}^{\dagger}(\vec{r}). \tag{3.63}$$

The denominator in Eq. (3.61) is given by the same formula as in Eq. (3.62), where the scalar Glauber phase is now put equal to 1. Similar to the nucleon-knockout discussion in section 2.4.2, the Glauber phase is written in terms of the profile functions $\Gamma_{\pi N}(\vec{b})$, whose energy-dependent parameters are fitted to the available πN scattering data [182].

The result of this Glauber approach is shown in Fig. 3.23. Below $T_\pi \sim 500$ MeV, some profile-function parameters can not be interpolated any more, resulting in no cross-section values there. Concentrating on the energy region where the RMSGA is expected to start giving valid results, i.e. from $T_\pi = 700$ MeV onwards, it is seen how only 25 to 30% of the produced pions are predicted to leave the iron nucleus undisturbed. The lost flux results from pions that have been subject to inelastic, secondary collisions inside the nucleus. Of course, most comments made in section 2.8 in relation to RMSGA computations of the elastic nucleon-knockout strength, are also in place here. More specifically, the Glauber calculations are known to provide rigorous estimates of FSI effects in situations where the residual nucleus is left with an excitation energy that does not exceed a few tens of MeV. Consequently, the RMSGA predictions shown in Fig. 3.23 lose some of their appeal when one considers that, at their present stage, most neutrino experiments cannot place the necessary cuts in missing energy to isolate these events. One approach that provides a more inclusive account of neutrino-induced pion production from nuclei is the Giessen coupled-channel transport model [41, 149]. Within their framework, dubbed the GiBUU model, a full record is kept of all inelasticities corresponding to charge-exchange reactions, pion absorptions and changes in energy and scattering angle of the produced pions. In the case of CC pion production, for example, it is inferred [41] that side-feeding from the dominant π^+ channel to the less-important π^0 one results in a larger reduction of the former with respect to the latter when FSI mechanisms are taken into account. Similarly, due to secondary collisions, a lot of high-energy pions *vanish*, only to reappear at the low-T_π side of the cross section. In this sense, one could say that the

GiBUU transport model is the preferred one in inclusive and semi-inclusive neutrino-scattering studies. On the other hand, the Glauber framework provides a viable alternative for the description of exclusive channels, which, through placing the necessary cuts in E_m, may provide information about genuine quantum-mechanical effects.

3.3 Coherent pion production

A process that has recently received a lot of attention is the *coherent* production of pions on nuclei,

$$\nu + A \longrightarrow l + A + \pi. \tag{3.64}$$

Here, the term coherent refers to νA scattering processes that leave the nuclear target intact by transferring only a small four-momentum squared $t = (q - k_\pi)^2$. A number of new experimental results motivates the surging interest in this type of processes. In particular, both the K2K [188] and SciBooNE [189] collaborations have found no evidence for CC coherent pion production. On the other hand, the MiniBooNE experiment has reported [190] NC events. At present, isolating the coherent events is a challenging task for most neutrino experiments, owing to difficulties in setting the necessary experimental triggers. Instead, coherent events are measured indirectly, by extracting them from the full data set while assuming some theoretical model for the incoherent pion-production strength. It is therefore quite clear that the aforementioned experimental results await further confirmation.
In the meantime, our theoretical understanding of the process has been gradually increasing. Generally speaking, there exist two distinct lines of research for the description of coherent pion production. A first method makes use of the PCAC principle to relate neutrino-induced coherent pion production to elastic pion-nucleus scattering amplitudes at low Q^2 [191, 192]. A second group of theoretical efforts adopts a more microscopic point of view and starts from a nuclear description identical to the one used for the incoherent pion-production process. Medium effects are included in the Δ propagator and the nuclear attenuation of the outgoing pion is taken into account. Some recent studies along this line can be found in Refs. [193–196]. In this section, we will conduct a study of coherent pion production along the latter lines.

3.3.1 Cross section

The lab-system cross section for $\nu + A \longrightarrow l + A + \pi$ assumes the following general form

$$\frac{d^5\sigma}{dE_l d\Omega_l d\Omega_\pi} = \frac{1}{2(2\pi)^5} \frac{m_\nu m_l k_l k_\pi}{E_\nu} \overline{\sum}_{fi} \left| M_{fi}^{(coh)} \right|^2. \tag{3.65}$$

Neglecting the recoil of the final nucleus, all of the transferred energy is directed to the produced pion, $\omega = E_\pi$. The invariant matrix element related to coherent pion

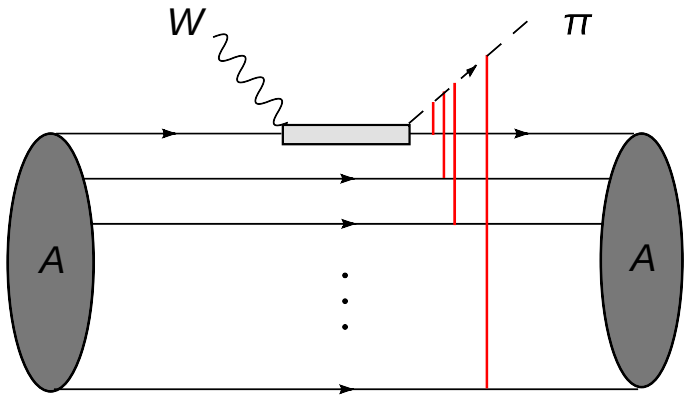

Figure 3.24: Schematic overview of the coherent reaction $\nu + A \to l + A + \pi$. The vertical lines stand for FSI effects on the outgoing pion, which are neglected in the RPWIA.

production can be decomposed in the standard fashion as $M_{fi}^{(coh)} \sim \langle J_{lep}^{\mu} \rangle \langle J_{nucl,\mu}^{(coh)} \rangle$, where the lepton current is identical to the one encountered in the QE and incoherent pion-production processes, see Eq. (2.11). Assuming that the s-channel diagram of Fig. 3.3 dominates the coherent pion-production process, and representing the outgoing pion by a plane wave, the nuclear current is given in momentum space by

$$\langle J_{nucl}^{(coh),\mu} \rangle = \sum_{\alpha} C_I \int d^3\vec{p}_m \, \overline{\mathcal{U}}_{\alpha}(\vec{p}_m + \vec{q} - \vec{k}_{\pi}) \mathcal{O}^{\mu} \mathcal{U}_{\alpha}(\vec{p}_m), \tag{3.66}$$

where $\mathcal{O}^{\mu} = \Gamma^{\rho}_{\Delta\pi N} S_{\Delta,\rho\sigma} \Gamma^{\sigma\mu}_{WN\Delta}$. Let us examine the above equation more closely. The scattering off the entire nucleus has been imposed by constructing the nuclear current as a coherent sum of single-nucleon currents, letting the summation index α run over all occupied nucleon states in the target nucleus. Figure 3.24 presents a schematic picture of the adopted reaction mechanisms. One-body mechanisms are considered to dominate the reaction dynamics, meaning that the impinging neutrino is presumed to interact with a single bound nucleon. In deriving Eq. (3.66), we have therefore adopted the IA. Constructing the nuclear wave function in an IPM as a fully anti-symmetrized form of the product of single-nucleon wave functions, the one-body currents found in the right-hand side of Eq. (3.66) evaluate the free operator $\mathcal{O}^{\mu}$ between final and initial bound-state spinors of the same single-particle state. Thereby, the momentum $\vec{p}_m$ of the struck nucleon is not defined sharply, but rather should be folded over in the full evaluation of the nuclear current matrix element. Owing to momentum conservation, the final bound-state spinor's momentum is given by $\vec{p}_m + \vec{q} - \vec{k}_{\pi}$. The constant C_I in Eq. (3.66) guarantees the inclusion of the correct

isospin coefficient in the Δ couplings. Put all together, Eq. (3.66) provides the most general way to deal with coherent pion production in the RPWIA framework.

3.3.2 Local approximation

Most articles dedicated to neutrino-induced coherent pion production, however, make use of an approximate form for the current (3.66). Indeed, in the so-called *local* approximation, the momentum of the incoming nucleon is kept fixed in the evaluation of the operator $\mathcal{O}^\mu$. A widely-used scheme [194, 195] consists of sharing the momentum transferred to the nucleus, $\vec{Q} = \vec{q} - \vec{k}_\pi$, between the initial and final nucleon, yielding

$$\vec{p}_m = -\frac{\vec{Q}}{2}. \tag{3.67}$$

Apart from guaranteeing energy-momentum conservation,

$$q^\mu + k_i^\mu = k_\pi^\mu + k_f^\mu; \quad k_i^\mu = (E, \vec{p}_m), \quad k_f^\mu = (E, -\vec{p}_m), \tag{3.68}$$

the main physical motivation for the on-shell prescription (3.67) stems from the fact that, with Gaussian nuclear wave functions, it leads to an exact treatment of the terms linear in $\vec{p}_m/2m_N$ in the elementary amplitude [197, 198]. On the other hand, there seems to be some arbitrariness in the choice of an appropriate, average nucleon momentum in local-approximation studies [199]. As a matter of fact, in pion photoproduction work [200–202], some alternatives to Eq. (3.67) have been studied, including the frozen nucleon approximation ($\vec{p}_m = \vec{0}$) and

$$\vec{p}_m = -\frac{A-1}{2A}\vec{Q}. \tag{3.69}$$

It is found [200, 201] that the prescription (3.69) yields results that compare well to the exact calculations, which involve a proper averaging over the nucleon momentum distribution. Moreover, both of the schemes (3.67) and (3.69) provide a fair description of pion photo- and electroproduction data. Using either prescription, the Δ four-momentum no longer depends on $\vec{p}_m$ and the nuclear current can be reformulated as

$$\langle J_{nucl}^{(coh),\mu} \rangle = \left[\int d^3\vec{p}_m \left(\sum_\alpha \mathcal{U}_\alpha(\vec{p}_m) \overline{\mathcal{U}}_\alpha(\vec{p}_m + \vec{q} - \vec{k}_\pi) \right) \right]_{AB} C_I \, \left(\mathcal{O}^\mu(q, k_\pi) \right)_{BA}. \tag{3.70}$$

In Eq. (3.70), the indices A and B refer to the components of the corresponding 4×4 complex matrices. The pion-production operator is now independent of $\vec{p}_m$ and may be brought outside the integral and the sum expression. The isospin factor C_I needs to be modified according to the nature of the incoming nucleon.
Hence, the local approximation accomplishes a factorization of the nuclear-current

matrix element into a part that contains the elementary pion-production operator and a nuclear form factor [203]

$$\rho_A(\vec{q}-\vec{k}_\pi)=\int d^3\vec{p}_m\left(\sum_\alpha \mathcal{U}_\alpha(\vec{p}_m)\overline{\mathcal{U}}_\alpha(\vec{p}_m+\vec{q}-\vec{k}_\pi)\right), \tag{3.71}$$

that reflects the ground-state properties of the nucleus. Transforming Eq. (3.71) in coordinate space, it is seen how the nuclear form factor emerges as the Fourier transform of the local nuclear density matrix $\rho_A(\vec{r},\vec{r})$

$$\begin{aligned}\rho_A(\vec{q}-\vec{k}_\pi)&=\int d^3\vec{r}e^{i(\vec{q}-\vec{k}_\pi)\cdot\vec{r}}\sum_\alpha \Psi_\alpha(\vec{r})\overline{\Psi}_\alpha(\vec{r}),\\&=\int d^3\vec{r}e^{i(\vec{q}-\vec{k}_\pi)\cdot\vec{r}}\rho_A(\vec{r},\vec{r}).\end{aligned} \tag{3.72}$$

From a numerical perspective, the separation of the involved complex-matrix expressions $\mathcal{O}^\mu$ means an important reduction of computing time. Whereas the full expression in Eq. (3.66) requires re-evaluating $\mathcal{O}^\mu$ for each point in the $\vec{p}_m$ integral, in the local approximation, a single calculation at a fixed $\vec{p}_m$ value is sufficient.

3.3.3 Medium effects

The formalism outlined above provides a general account of all ingredients necessary to perform RPWIA calculations of neutrino-induced coherent pion production. To describe the nuclear ground-state, we will employ the bound-state wave functions introduced earlier in section 2.4.1. In addition, one needs to consider the influence of the medium on the produced Δ and the outgoing pion. To account for medium modifications, we adopt the substitutions of Eq. (3.58) for the mass and width in the Δ propagator:

$$\begin{aligned}M_\Delta &\longrightarrow M_\Delta+30\text{ MeV},\\ \Gamma &\longrightarrow \Gamma+40\text{ MeV},\end{aligned} \tag{3.73}$$

Computing the nuclear attenuation on the ejected pion proves a more challenging task. Indeed, the approach applied in our discussion of incoherent pion production, where the RPWIA cross section was multiplied by a transparency factor $\mathcal{T}(\vec{p}_m)$ to estimate FSI effects, does not seem adequate for coherent scattering. As pointed out in section 3.3.1, the kinematic variables determining the fivefold coherent cross section of Eq. (3.65) do not fix the incoming-nucleon's momentum. Instead, the nuclear-current matrix element involves a folding over the nucleon momentum distributions. As a consequence, in coherent pion production, one has to resort to an unfactorized treatment of FSI effects.

Since the pion's wave function is no longer represented by a plane wave, FSI calculations are most naturally described in coordinate space. Combining Eqs. (3.70) and (3.72), in the local approximation, the RPWIA nuclear-current matrix element is given by

$$\langle J^{(coh),\mu}_{nucl}\rangle = C_I \mathcal{O}^{\mu}(q,k_\pi)\left[\int d^3\vec{r}\, e^{i(\vec{q}-\vec{k}_\pi)\cdot\vec{r}}\rho_A(\vec{r},\vec{r})\right]. \tag{3.74}$$

Correspondingly, FSI mechanisms can be accounted for by making the following replacements [195] in Eq. (3.74)

$$\begin{aligned} e^{-i\vec{k}_\pi\cdot\vec{r}} &\longrightarrow \phi^*_{k_\pi}(\vec{r}),\\ \vec{k}_\pi e^{-i\vec{k}_\pi\cdot\vec{r}} &\longrightarrow i\vec{\nabla}\phi^*_{k_\pi}(\vec{r}), \end{aligned} \tag{3.75}$$

where $\phi^*_{k_\pi}(\vec{r})$ stands for the distorted outgoing-pion wave function. Within the Glauber approach, all information regarding pion rescatterings with the residual nucleons is contained in the Glauber phase $\mathcal{G}(\vec{b},z)$, and the pion scattering wave function becomes

$$\phi_{k_\pi}(\vec{r}) = \mathcal{G}(\vec{b},z)e^{i\vec{k}_\pi\cdot\vec{r}}, \tag{3.76}$$

using the same notations as in section 2.4.2. Furthermore, it is important to note that the second line in Eq. (3.75) will introduce some non-local behavior in the amplitudes. By stating that the pion momentum is not strictly defined inside the nucleus, the operator $\mathcal{O}^{\mu}(q,k_\pi)$ - being proportional to k^{α}_{π} - is indeed pulled back into the integral. If the local approximation is not invoked, the nuclear-current expression becomes highly involved,

$$\langle J^{(coh),\mu}_{nucl}\rangle = \sum_{\alpha}\int d^3\vec{r}\, d^3\vec{r}\,'\overline{\Psi}_{\alpha}(\vec{r})\phi^*_{k_\pi}(\vec{r})\mathcal{O}^{\mu}(q;\vec{r},\vec{r}\,')e^{i\vec{q}\cdot\vec{r}\,'}\Psi_{\alpha}(\vec{r}\,'). \tag{3.77}$$

In coordinate space, the non-locality of the transition operator $\mathcal{O}^{\mu}$ is reflected by its dependence on two position vectors, $\vec{r}$ and $\vec{r}\,'$. The resulting 6-dimensional integral in the matrix element poses a non-trivial numerical problem, that may be tackled by considering a partial-wave expansion [203] for the integrandum in Eq. (3.77). For higher pion energies, however, it will become harder and harder to reach convergence in the expansion series. In that case, one might consider to exploit the smoothness of the integrandum by storing a grid of $\langle\mathcal{O}^{\mu}\rangle$ values and using interpolated values in the integration routine.

3.3.4 Results

Now, we will present calculations for neutrino-induced coherent pion production. Most of our results involve carbon nuclei, because they are frequently employed as

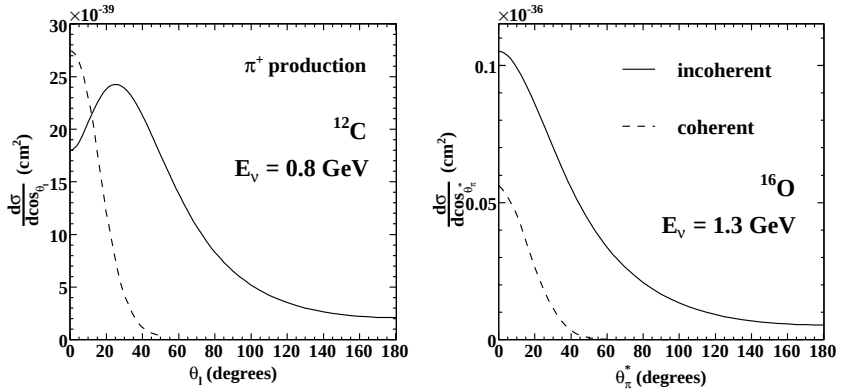

Figure 3.25: Comparison between incoherent (full) and coherent (dashed) CC π^+-production cross sections.

target material by neutrino-scattering experiments (among other in the SciBooNE and MINERνA setups). As a representative example, we adopt $E_\nu = 1$ GeV. The standard input values for the Δ couplings are adopted: the vector form factors of Eqs. (3.18) and (3.19), the axial form factors of Eq. (3.21) with $M_A = 1.05$ GeV and $C_5^A(0) = 1.2$, and the $\Delta\pi N$ coupling defined in Eq. (3.33), with $f_{\pi N\Delta} = 2.21$.

First, let us investigate some general characteristics of the coherent pion-production process. To this end, in Figs. 3.25 to 3.27, we present a number of RPWIA computations that have been performed in the local approximation with $\vec{p}_m = -\vec{Q}/2$. Figure 3.25 contrasts angular distributions for the incoherent and coherent production of π^+'s. Compared to the incoherent cross sections, the coherent ones are markedly more forward-peaked. Both the outgoing muon and pion are very likely to escape along the neutrino-beam direction in coherent processes. This is a typical signature of coherent processes, because they require very low momentum transfers to maintain the nuclear target in its ground state. In Fig. 3.26, we study the dependence of a CC coherent π^+-production cross section on the momentum transfers Q^2 and t. The peak in the $|t|$ distribution reflects the sharp fall-off of the nuclear form factor $\rho_A(\vec{q} - \vec{k}_\pi)$ which, as we saw in Eq. (3.70), largely determines the behavior of coherent processes. Moreover, at an incoming neutrino energy of 1 GeV, all strength is located at $Q^2 \lesssim 0.2$ GeV^2. As shown in Fig. 3.27, the axial form factors dominate the cross section. Putting all vector form factors to zero only leads to minor changes with respect to the situation where all form factors are taken into account. Consequently, the coherent cross section is extremely sensitive to the value of $C_5^A(0)$. Adopting a value of $C_5^A(0) = 0.9$, as favored by a recent analysis of ANL data [151], may lead to a 40-50% reduction with respect to $C_5^A(0) = 1.2$.

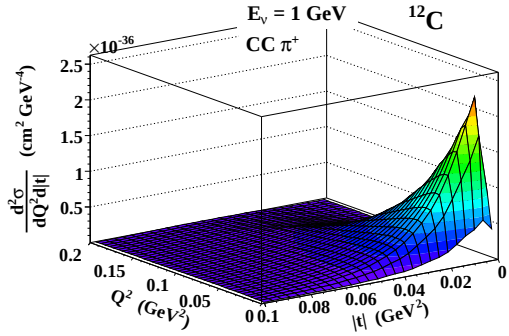

Figure 3.26: Dependence of the CC coherent π^+-production cross section on Q^2 and $|t| = (\vec{q} - \vec{k}_\pi)^2$.

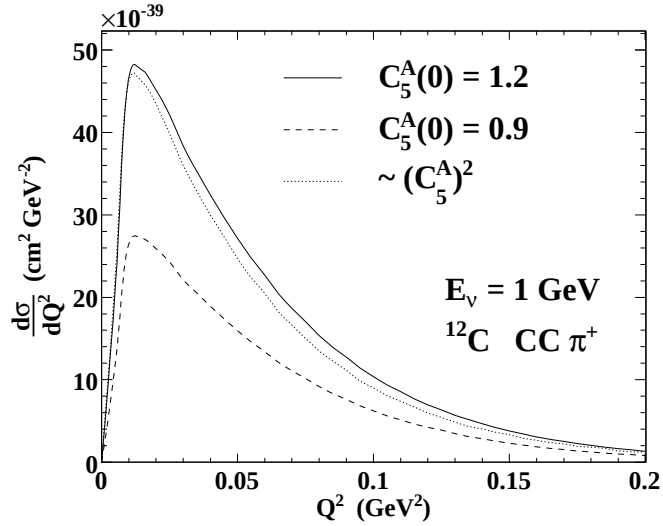

Figure 3.27: Variation of the CC coherent π^+-production cross section as a function of Q^2. The full (dashed) line displays the result for a $C_5^A(0)$ value of 1.2 (0.9). Retaining only contributions proportional to $(C_5^A)^2$ yields the dotted line.

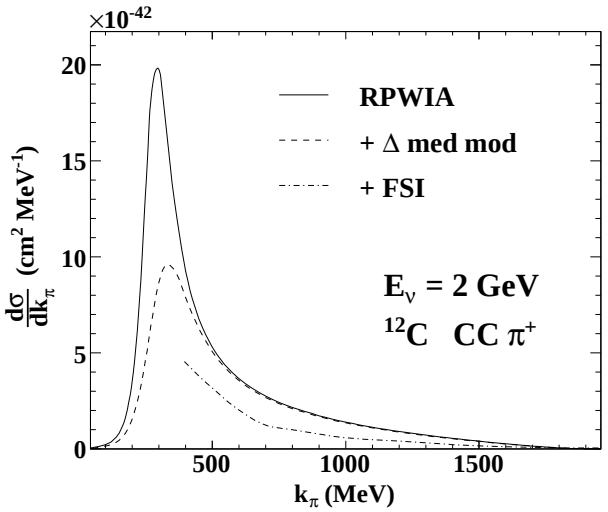

Figure 3.28: Study of nuclear effects on the pion-momentum distribution for CC coherent π^+-production from a carbon target. The full (dashed) curve shows the RPWIA calculation, without (with) medium modifications. The dash-dotted curve includes FSI effects within a Glauber approach.

Turning to the influence of nuclear effects, Fig. 3.28 shows how Δ medium modifications and the nuclear attenuation on the outgoing pion affect the RPWIA cross section. Clearly, the collisional broadening of the width produces a strong reduction of the coherent cross section. In the peak region, the effect amounts to 50%. In the tail, where $\Delta \to \pi N$ decays are absolutely dominant, medium modifications have little or no impact on the RPWIA cross section. These findings are in very good agreement with the results reported in Refs. [193–195]. It is worth mentioning that the latter studies use the full, density-dependent medium modifications of Eq. (3.55), lending additional confidence to the reliability of our efficient scheme, $\Gamma \to \Gamma + 40$ MeV. In Fig. 3.28, we also illustrate the effect of FSI mechanisms on the pion-momentum cross section. As explained in section 3.3.3, we replaced $e^{i\vec{k}_\pi \cdot \vec{r}}$ by $\mathcal{G}(\vec{b}, z) e^{i\vec{k}_\pi \cdot \vec{r}}$ in the nuclear current (3.74). To simplify the numerical calculations, the asymptotic (free) pion momentum $\vec{k}_\pi$ was used in the evaluation of $\mathcal{O}^\mu$. In the energy region where the Glauber approach is expected to be valid, i.e. for $k_\pi > 800$ MeV, we infer that $\sim 40\%$ of the produced pions reach the detectors. This FSI effect is larger than the one reported in Refs. [194, 195], where the pion wave function is obtained as a solution of the Klein-Gordon equation with a microscopic optical potential. To the contrary, the eikonal

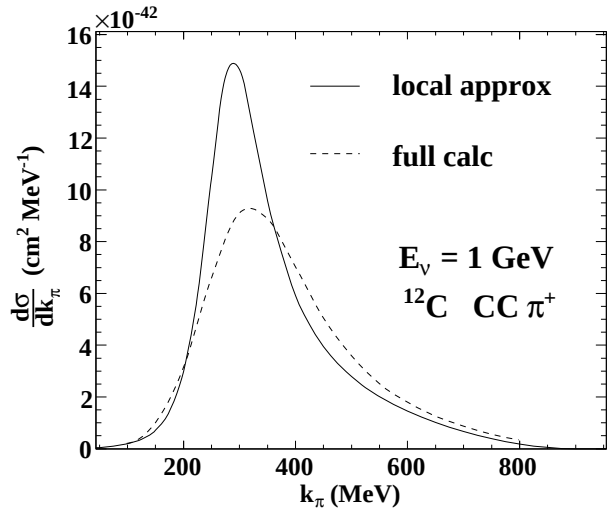

Figure 3.29: Comparison between full and local-approximation calculations for CC coherent π^+ production.

approximation used in Ref. [193] predicts an even larger reduction of the RPWIA cross section, finding that only 30% of the pions leave the nucleus undisturbed. Furthermore, from Fig. 3.28, it is obvious that the Glauber calculations cannot be trusted for low pion energies. In this respect, it would be very interesting to compare our result with a typical low-energy approach, for example an RDWIA calculation.

In section 3.3.2, it was explained how the local approximation is introduced for mostly technical reasons, offering a substantial numerical advantage. In addition, for some well-chosen $\vec{p}_m$ values, the local approximation has been relatively successful in describing coherent pion photo- and electroproduction data. It has been pointed out [199], however, that the usefulness of the local approximation depends very much on the nature of the transition operator $\mathcal{O}^\mu$. Hence, as the neutrino-induced process is dominated by axial transition currents, it is important to check whether the local approximation provides a valid framework in this case too. In Fig. 3.29, we compare a local calculation, using $\vec{p}_m = -\vec{Q}/2$, with a full calculation (3.66), which includes the proper averaging of $\langle\hat{\mathcal{O}}^\mu\rangle$ over the nucleon momentum distribution. As one can appreciate, the full calculation differs considerably from the local-approximation result, providing evidence that the latter may not be that suitable for the description of neutrino-induced coherent pion-production processes. This finding seems to corroborate the recent result by Leitner et al. [196], as can be appreciated by looking at Fig. 3.30. Work to include nuclear attenuation effects along the lines of Eq. (3.77) is

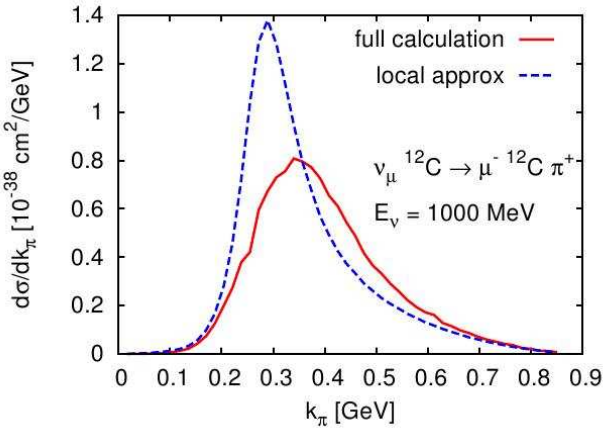

Figure 3.30: Comparison between full and local-approximation calculations by the Giessen group. Figure taken from Ref. [196].

currently in progress. In general, we again expect strong reductions of the full RPWIA cross section, due to medium modifications and pion distortion effects.

4
Conclusions

Motivated by neutrino experiments entering the precision phase, we conducted a study of quasi-free neutrino-nucleus interactions at typical accelerator-beam energies of 1 GeV. For medium momentum transfers ($Q^2 \lesssim 1$ GeV^2), the nuclear excitation spectrum reveals two broad peaks (Fig. 1.1), corresponding to QE nucleon knockout and Δ production. Dominated by one-body kinematics, a theoretical description of these processes is most commonly formulated in terms of hadronic degrees of freedom, adopting the IA to express the nuclear transition current as a sum of one-body hadron currents. Invoking, in addition, an IPM for the nuclear wave functions, all modeling efforts can be concentrated on the hadron-current matrix elements that contain all process-related dynamics. As a matter of fact, by virtue of the IA and IPM, modeling these quantities becomes a two-step process. First, one considers the elementary couplings of the free process. In this thesis, we adopt a phenomenological parameterization for the weak hadron currents, based on the introduction of running, Q^2-dependent coupling constants, dubbed form factors, to account for the finite extension of hadrons. Next, we focus on nuclear effects. Nuclear-structure wise, we adhere to a mean-field picture and obtain the corresponding single-nucleon wave functions in the Hartree approximation to the σ-ω Walecka model [24]. Furthermore, an essential ingredient in quasi-free scattering studies is the treatment of nuclear attenuation effects on the outgoing hadrons. To deal with FSI mechanisms, we turn to the Glauber approach developed in Ref. [37]. Postulating linear trajectories and frozen spectator nucleons, this multiple-scattering extension of the eikonal approximation predicts

what fraction of the hadrons will reach the detectors without undergoing any secondary interactions. The full model outlined here to describe neutrino-induced QE nucleon-knockout and Δ-mediated one-pion production reactions is coined RMSGA. More specifically, within the RMSGA model, we can compute neutrino-nucleus cross sections for direct knockout processes. From an experimental point of view, these reactions correspond to the windows $E_m \leq 80$ MeV and $|\vec{p}_m| \leq 300$ MeV. Hence, establishing the experimental triggers to select these events is an extremely challenging task in accelerator-based neutrino experiments because of the wide energy spread of the neutrino beam. Nevertheless, planned neutrino experiments with a dedicated cross-section physics program, such as MINERνA, aim at creating experimental conditions that have a large potential to conduct this type of studies.

QE nucleon knockout

In section 2.5, we started our discussion of QE cross sections with a comparison of RPWIA calculations to inclusive $A(e,e')$ data. To simplify the numerical calculations, we introduced the notion of a bound-state propagator and obtained a closed form for the RPWIA cross section in momentum space. For moderate Q^2, we find that both the RPWIA and RFG calculations provide a fair description of the QE peak region. Both models tend to overestimate the strength at the peak, while the RPWIA predictions give a better account of the tails in the ω distribution than the RFG ones. For $Q^2 \lesssim 0.1$ GeV^2, the description gets worse and we observe a break-down of the IA. There, multi-nucleon excitations become important, making the inclusion of long-range RPA correlations indispensable.

Turning to neutrino-nucleus cross sections, it is seen that the current 20%-level uncertainties on the value of M_A translate in cross-section variations of the same order. For estimating nuclear attenuation effects on the outgoing nucleon, we show that rescaling the RPWIA result with a factor extracted from $A(e,e'p)$ transparencies leads to a very good agreement with the full, unfactorized RMSGA calculations. In addition, RMSGA predictions prove to compare favorably with data in exclusive and semi-exclusive electron-scattering studies [38]. Hence, with the experimental windows $|\vec{p}_m| \leq 300$ MeV and $E_m \leq 80$ MeV, the elastic nucleon-knockout contribution to the inclusive νA cross section may serve as a lever for a precise determination of M_A.

In section 2.6, we studied the possibility of a low-Q^2 Weinberg-angle measurement through the QE Paschos-Wolfenstein relation. Though nuclear-model effects are extremely well controlled, the $\sin^2\theta_W$ sensitivity of this super-ratio of $\nu(\overline{\nu})A$ cross sections is still a great deal smaller than in parity-violating electron-scattering experiments. On the other hand, the proton-knockout part of the Paschos-Wolfenstein relation exhibits a rather strong dependence on g_A^s. With a reliable input for the vector strangeness parameters, this ratio may serve as a lever to extract new information

on the strangeness contribution to the nucleon spin. In section 2.7, we conducted a more systematic study of the strangeness sensitivity of QE $\nu(\overline{\nu})A$ cross-section ratios. Owing to its mild dependence on μ_s and r_s^2, the ratio $R_{p/n}^{\overline{\nu}}$ is one of the more viable candidates to extract a value for g_A^s.

Δ-mediated one-pion production

We adopted a Δ-dominance model to study neutrino-induced one-pion production. In section 3.1, we scrutinized the weak and strong Δ couplings that are involved in the free pion-production process. The lack of precision in neutrino bubble-chamber data produces 30%-level uncertainties on $C_5^A(Q^2)$ and the corresponding $N(\nu, l\pi)$ cross-section predictions. To the contrary, ambiguities in the $\Delta\pi N$ couplings related to unwanted spin-1/2 parts have little effect on the observables.
Moving on to nuclear reactions in section 3.2, we computed cross sections for primary, i.e. prior to knockout, pion production and compared them to inclusive electron-scattering data and other theoretical approaches. Including medium modifications of Δ properties by the substitutions $M_\Delta \rightarrow M_\Delta + 30$ MeV and $\Gamma \rightarrow \Gamma + 40$ MeV results in a fair estimate of the one-pion yield in the Δ region. Under quasi-free conditions, where the detected pion is the same as the one produced in the Δ decay, we infer large nuclear attenuation effects. In the case of an iron target, for example, only about one quarter of the pions leave the nucleus without any further interactions.
Finally, in section 3.3, we focus on coherent pion production from nuclei. Dominated by small momentum transfers, this reaction is extremely sensitive to the value of $C_5^A(0)$. In the local approximation, achieved by fixing the value of $\vec{p}_m$ in the nuclear current operator $\hat{\mathcal{O}}^\mu$, we show that nuclear effects decimate the $\nu + A \longrightarrow l + A + \pi$ cross sections. Just like for incoherent pion production, our scheme for Δ medium modifications leads to results that are similar to those obtained by more involving approaches reported in literature. Also, we find non-trivial differences between the ubiquitously-applied local approximation and a full calculation, including the proper averaging of $\langle \hat{\mathcal{O}}^\mu \rangle$ over the nucleon momentum distribution. Although it performs nicely in photo- and electroproduction studies, the local approximation seems questionable when used in the context of neutrino-induced coherent pion production.

Outlook

As already stated earlier, neutrino experiments often do not have the means to select samples of quasi-free events. Instead, when the residual nuclear system remains unobserved, one adopts a more *inclusive* notion of nucleon emission and pion production from nuclei. In this sense, arguably the most interesting improvement to the model presented here would be to extend it beyond the quasi-free regime.

For E_m values higher than the separation energies for the deepest shells, one could first study the importance of two-body mechanisms in inclusive neutrino-nucleus cross sections. In electron-scattering studies, a direct calculation of these contributions [48, 204] is known to explain, at least in part, the strength in the dip region [49]. Another, perhaps more practical, approach consists of replacing the bound-state propagator (2.52), encoding fully-occupied single-particle orbitals, by a spectral function $S(E_m, \vec{p}_m)$ [22]. Apart from the mean-field contribution, the latter additionally accounts for the effects from short-range nucleon-nucleon correlations.
For even higher missing energies, corresponding to nuclear break-up scenarios where a number of pions and/or nucleons come off the nucleus, the only viable way to provide an inclusive description of νA reactions is by adopting Monte-Carlo or transport-model techniques [41]. The RPWIA predictions presented in this thesis could hereby serve as input before the produced hadrons are propagated in the nuclear medium.
In addition, the current model for quasi-free reactions leaves room for a number of improvements. A study of non-resonant background contributions [151] in weak pion production off nuclei is one possibility. Next to Δ production, one could consider an extension towards the second resonance region, including the $P_{11}(1440)$, $D_{13}(1520)$ and $S_{11}(1535)$ resonances [160]. Beyond this region, however, the number of unconstrained (axial) $N - N^*$ couplings becomes unmanageable. Hence, in the transition region towards DIS, the inclusive νA strength is being actively investigated in quark-hadron duality studies [184]. Alternatively, to obtain predictions in the transition region, one might consider the possibility of using Regge-inspired models.

A

Notations and conventions

Natural units are assumed throughout this work, $\hbar = c = 1$. We use the Einstein summation convention, according to which repeated indices are summed over.

A.1 Four-vector notation

A general, contravariant four-vector x is written as

$$x^\mu = (x^0, x^1, x^2, x^3) = (x^0, \vec{x}). \tag{A.1}$$

Its covariant form is found by lowering the Lorentz index

$$x_\mu = g_{\mu\nu} x^\nu = (x^0, -\vec{x}), \tag{A.2}$$

with the metric given by

$$g_{\mu\nu} = g^{\mu\nu} = \begin{pmatrix} 1 & 0 & 0 & 0 \\ 0 & -1 & 0 & 0 \\ 0 & 0 & -1 & 0 \\ 0 & 0 & 0 & -1 \end{pmatrix}. \tag{A.3}$$

The inner product of two four-vectors is defined as follows

$$x \cdot y = x^\mu y_\mu = x^0 y^0 - \vec{x} \cdot \vec{y}. \tag{A.4}$$

A.2 Dirac matrices

For the γ matrices, we use the familiar representation

$$\gamma^0 = \begin{pmatrix} 1 & 0 \\ 0 & -1 \end{pmatrix}, \quad \vec{\gamma} = \begin{pmatrix} 0 & \vec{\sigma} \\ -\vec{\sigma} & 0 \end{pmatrix}, \tag{A.5}$$

where 0 and 1 are shorthand notations for the 2×2 zero and identity matrix respectively. The Pauli matrices are given by

$$\sigma^1 = \begin{pmatrix} 0 & 1 \\ 1 & 0 \end{pmatrix}, \quad \sigma^2 = \begin{pmatrix} 0 & -i \\ i & 0 \end{pmatrix}, \quad \sigma^3 = \begin{pmatrix} 1 & 0 \\ 0 & -1 \end{pmatrix}. \tag{A.6}$$

Important combinations of γ matrices are

$$\gamma^5 = i\gamma^0\gamma^1\gamma^2\gamma^3 = \gamma_5, \quad \sigma^{\mu\nu} = \frac{i}{2}\left[\gamma^\mu, \gamma^\nu\right] \tag{A.7}$$

With the definitions (A.5) and (A.6), one finds

$$\gamma^5 = \begin{pmatrix} 0 & 1 \\ 1 & 0 \end{pmatrix}. \tag{A.8}$$

The γ matrices satisfy the anticommutation relations

$$\{\gamma^\mu, \gamma^\nu\} = \gamma^\mu\gamma^\nu + \gamma^\nu\gamma^\mu = 2g^{\mu\nu}, \quad \{\gamma^\mu, \gamma^5\} = 0. \tag{A.9}$$

The totally antisymmetric tensor, or Levi-Civita symbol, is defined as

$$\epsilon_{\mu\nu\rho\sigma} = \begin{cases} +1 & \text{if } (\mu,\nu,\rho,\sigma) \text{ is an even permutation of } (0,1,2,3) \\ -1 & \text{if } (\mu,\nu,\rho,\sigma) \text{ is an odd permutation of } (0,1,2,3) \\ 0 & \text{if any index is repeated} \end{cases}. \tag{A.10}$$

In derivations of spin-summed tensor quantities, one is often confronted with traces of products of γ matrices. Some of the most occurring combinations are

$$\begin{aligned} \mathrm{Tr}(\text{odd number of } \gamma \text{ matrices}) &= 0 \\ \mathrm{Tr}(\gamma^5) &= 0 \\ \mathrm{Tr}(\gamma^\mu\gamma^\nu) &= 4g^{\mu\nu} \\ \mathrm{Tr}(\gamma^\mu\gamma^\nu\gamma^\rho\gamma^\sigma) &= 4(g^{\mu\nu}g^{\rho\sigma} - g^{\mu\rho}g^{\nu\sigma} + g^{\mu\sigma}g^{\nu\rho}) \\ \mathrm{Tr}(\gamma^5\gamma^\mu\gamma^\nu\gamma^\rho\gamma^\sigma) &= 4i\epsilon_{\mu\nu\rho\sigma} \end{aligned} \tag{A.11}$$

A.3 Spinors and normalizations

The Dirac spinor for a particle with four-momentum k and spin four-vector s is written as $u(k,s)$. Using the shorthand notation $\not{k} = \gamma_\mu k^\mu$, the spinor u satisfies the Dirac equation

$$(\not{k} - m)u(k,s) = 0. \tag{A.12}$$

The solutions for a free particle are given by

$$u(k,s) = \sqrt{\frac{E+m}{2m}} \begin{pmatrix} \chi_s \\ \frac{\vec{\sigma}\cdot\vec{k}}{E+m}\chi_s \end{pmatrix}, \tag{A.13}$$

where $E = +\sqrt{k^2+m^2}$ and χ_s denotes the two-component spin state,

$$\chi_{m_s=+1/2} = \begin{pmatrix} 1 \\ 0 \end{pmatrix}, \quad \chi_{m_s=-1/2} = \begin{pmatrix} 0 \\ 1 \end{pmatrix}. \tag{A.14}$$

Defining the conjugate $\overline{u} = u^\dagger \gamma^0$, these spinors are normalized as $\overline{u}(k,s)u(k,s) = 1$. The energy projection operators are then given by

$$\sum_{\pm s} u(k,s)\overline{u}(k,s) = \left(\frac{\not{k}+m}{2m}\right). \tag{A.15}$$

In accordance with this Dirac-spinor normalization, we have the factor $\sqrt{m/E}$ appearing in the phase-space volume of cross-section formulas. Assuming the positive-energy solutions of the Klein-Gordon equation to be

$$\phi(x) = e^{-ip\cdot x}\frac{1}{\sqrt{(2\pi)^3 2E}}, \tag{A.16}$$

for pions, the factor $\sqrt{m/E}$ needs to be replaced by $1/\sqrt{2E}$.

B
Δ width formula

In the πN center-of-mass (cm) frame, the differential decay rate of the Δ is given by [44]

$$d\Gamma = \frac{d^3\vec{k}_\pi}{2E_\pi(2\pi)^3}\frac{m_N}{E_N}\frac{d^3\vec{k}_N}{(2\pi)^3}(2\pi)^4\delta^{(4)}(k_\Delta - k_\pi - k_N)\overline{\sum}_{fi}\left|M_{fi}\right|^2. \tag{B.1}$$

Using the δ-function to integrate over $\vec{k}_N$, and integrating over $k_\pi = \left|\vec{k}_\pi\right|$ by employing the property

$$\delta(f(k_\pi)) = \frac{\delta(k_\pi - k_{\pi,0})}{|\partial f/\partial k_\pi|_{k_\pi = k_{\pi,0}}}, \quad f(k_{\pi,0}) = 0\,, \tag{B.2}$$

yields for the total decay width

$$\Gamma = \frac{m_N k_\pi}{2\pi M_\Delta}\overline{\sum}_{fi}\left|M_{fi}\right|^2. \tag{B.3}$$

In Eq. (B.3), the cm pion momentum can be written as

$$k_\pi \equiv |\vec{q}_{cm}| = \frac{\sqrt{(W^2 - m_\pi^2 - m_N^2)^2 - 4m_\pi^2 m_N^2}}{2W}. \tag{B.4}$$

The less tedious way to obtain an explicit expression for the squared invariant matrix element in Eq. (B.3) is to use the traditional $\Delta\pi N$ vertex function of Eq. (3.34). Then,

the invariant matrix element reads

$$M_{fi} = \frac{f_{\pi N\Delta}}{m_\pi}\overline{u}(k_N, s_N)k_{\pi,\mu}U^\mu_\Delta(k_\Delta, s_\Delta), \tag{B.5}$$

with U^μ_Δ the free Rarita-Schwinger spinor. This gives

$$\begin{aligned}\overline{\sum}_{fi}\left|M_{fi}\right|^2 &= \frac{1}{4}\sum_{s_\Delta; s_N} M^\dagger_{fi}M_{fi} \\ &= \frac{1}{4}\frac{f^2_{\pi N\Delta}}{m^2_\pi}\mathrm{Tr}\left(\mathscr{S}^{\nu\mu}_\Delta k_{\pi,\mu}\left(\frac{\not{k}_N + m_N}{2m_N}\right)k_{\pi,\nu}\right),\end{aligned} \tag{B.6}$$

where the Rarita-Schwinger projection operator is given by

$$\begin{aligned}\mathscr{S}_{\Delta,\mu\nu} &= \sum_{s_\Delta} U_{\Delta,\mu}\overline{U}_{\Delta,\nu} \\ &= -\left(\frac{\not{k}_\Delta + M_\Delta}{2M_\Delta}\right)\left(g_{\mu\nu} - \frac{\gamma_\mu\gamma_\nu}{3} - \frac{2k_{\Delta,\mu}k_{\Delta,\nu}}{3M^2_\Delta} - \frac{\gamma_\mu k_{\Delta,\nu} - \gamma_\nu k_{\Delta,\mu}}{3M_\Delta}\right).\end{aligned} \tag{B.7}$$

The factor $1/4$ in Eq. (B.6) stems from the averaging over Δ spin states. Using the trace identities in Eq. (A.11) to evaluate the trace expression in Eq. (B.6), one finds after some straightforward algebra

$$\overline{\sum}_{fi}\left|M_{fi}\right|^2 = \frac{f^2_{\pi N\Delta}}{6m^2_\pi m_N M_\Delta}\left[\left(k_\Delta\cdot k_N + M_\Delta m_N\right)\left(\frac{(k_\pi\cdot k_\Delta)^2}{M^2_\Delta} - m^2_\pi\right)\right]. \tag{B.8}$$

Combining Eqs. (B.8) and (B.3) then leads to the following formula for the Δ width in the cm frame

$$\Gamma = \frac{f^2_{\pi N\Delta}k^3_\pi}{12\pi m^2_\pi M_\Delta}(E_N + m_N), \tag{B.9}$$

where k_π is given in Eq. (B.4) and $E_N = \sqrt{k^2_\pi + m^2_N}$. Extending Eq. (B.9) off-shell, by replacing M_Δ with W, yields the energy-dependent Δ width of Eq. (3.37). To derive this formula, we could have equally well started from the consistent $\Delta\pi N$ coupling in Eq. (3.36). Although the corresponding calculation is much more cumbersome due to a more involved trace expression, one can check that the same expression for Γ emerges from it.

Bibliography

[1] S. L. Glashow, Nucl. Phys. **22**, 579 (1961).

[2] S. Weinberg, Phys. Rev. Lett. **19**, 1264 (1967).

[3] F. Englert and R. Brout, Phys. Rev. Lett. **13**, 321 (1964).

[4] P. W. Higgs, Phys. Rev. Lett. **13**, 508 (1964).

[5] K. Zuber, *Neutrino physics* (Institute of Physics, Bristol, 2004).

[6] E. A. Paschos, *Electroweak theory* (University Press, Cambridge, 2007).

[7] G. Bernardi et al. (Tevatron New Phenomena Higgs Working Group), arXiv:0808.0534 [hep-ex] (2008).

[8] G. Drexlin, J. Phys. Conf. Ser. **136**, 022031 (2008).

[9] E. Fiorini, Nucl. Phys. **A805**, 313c (2008).

[10] S. Hannestad, Phys. Rev. **D66**, 125011 (2002).

[11] E. A. Paschos, Nucl. Phys. Proc. Suppl. **112**, 36 (2002).

[12] M. Shaposhnikov, arXiv:0708.3550 [hep-th] (2007).

[13] A. A. Aguilar-Arevalo et al. (MiniBooNE), Phys. Rev. Lett. **98**, 231801 (2007).

[14] Proceedings of the 9th International Workshop on Neutrino Factories, Superbeams and Betabeams (NuFact07), Okayama, Japan, 6-11 Aug 2007, AIP Conf. Proc. 981 (2008).

[15] http://minerva.fnal.gov/.

[16] http://www-sciboone.fnal.gov/.

[17] C. J. Horowitz, H.-C. Kim, D. P. Murdock, and S. Pollock, Phys. Rev. **C48**, 3078 (1993).

[18] W. M. Alberico et al., Nucl. Phys. **A623**, 471 (1997).

[19] M. C. Martínez et al., Phys. Rev. **C73**, 024607 (2006).

[20] A. Meucci, C. Giusti, and F. D. Pacati, Nucl. Phys. **A739**, 277 (2004).

[21] B. Van Der Ventel and J. Piekarewicz, Phys. Rev. **C69**, 035501 (2004).

[22] O. Benhar and D. Meloni, Nucl. Phys. **A789**, 379 (2007).

[23] A. M. Ankowski and J. T. Sobczyk, Phys. Rev. **C77**, 044311 (2008).

[24] R. J. Furnstahl, B. D. Serot, and H.-B. Tang, Nucl. Phys. **A615**, 441 (1997).

[25] J. Nieves, M. Valverde, and M. J. Vicente Vacas, Phys. Rev. **C73**, 025504 (2006).

[26] S. K. Singh, N. C. Mukhopadhyay, and E. Oset, Phys. Rev. **C57**, 2687 (1998).

[27] N. Jachowicz, K. Heyde, J. Ryckebusch, and S. Rombouts, Phys. Rev. **C65**, 025501 (2002).

[28] J. Ryckebusch, K. Heyde, D. Van Neck, and M. Waroquier, Nucl. Phys. **A503**, 694 (1989).

[29] E. Oset and L. L. Salcedo, Nucl. Phys. **A468**, 631 (1987).

[30] I. J. D. MacGregor et al., Phys. Rev. Lett. **80**, 245 (1998).

[31] S. Boffi, C. Giusti, and F. D. Pacati, Phys. Rept. **226**, 1 (1993).

[32] J. Kelly, Adv. Nucl. Phys. **23**, 75 (1996).

[33] C. Maieron, M. C. Martínez, J. A. Caballero, and J. M. Udías, Phys. Rev. **C68**, 048501 (2003).

[34] A. Meucci, C. Giusti, and F. D. Pacati, Nucl. Phys. **A744**, 307 (2004).

[35] A. V. Butkevich and S. A. Kulagin, Phys. Rev. **C76**, 045502 (2007).

[36] R. J. Glauber and G. Matthiae, Nucl. Phys. **B21**, 135 (1970).

[37] J. Ryckebusch et al., Nucl. Phys. **A728**, 226 (2003).

[38] K. G. Fissum et al. (Jefferson Lab Hall A), Phys. Rev. **C70**, 034606 (2004).

[39] E. A. Paschos, L. Pasquali, and J. Y. Yu, Nucl. Phys. **B588**, 263 (2000).

[40] S. Ahmad, M. Sajjad Athar, and S. K. Singh, Phys. Rev. **D74**, 073008 (2006).

[41] T. Leitner, L. Alvarez-Ruso, and U. Mosel, Phys. Rev. **C73**, 065502 (2006).

[42] O. Buss, T. Leitner, U. Mosel, and L. Alvarez-Ruso, Phys. Rev. **C76**, 035502 (2007).

[43] A. A. Aguilar-Arevalo et al. (MiniBooNE), Phys. Rev. Lett. **100**, 032301 (2008).

[44] J. D. Bjorken and S. D. Drell, *Relativistic Quantum Mechanics* (McGraw-Hill, New York, 1964).

[45] T. W. Donnelly, Prog. Part. Nucl. Phys. **13**, 183 (1985).

[46] J. Ryckebusch, D. Debruyne, W. Van Nespen, and S. Janssen, Phys. Rev. **C60**, 034604 (1999).

[47] J. Ryckebusch, Phys. Rev. **C64**, 044606 (2001).

[48] V. Van der Sluys, J. Ryckebusch, and M. Waroquier, Phys. Rev. **C51**, 2664 (1995).

[49] M. Iodice et al., Phys. Lett. **B653**, 392 (2007).

[50] P. Lava, J. Ryckebusch, B. Van Overmeire, and S. Strauch, Phys. Rev. **C71**, 014605 (2005).

[51] R. Schiavilla, O. Benhar, A. Kievsky, L. E. Marcucci, and M. Viviani, Phys. Rev. Lett. **94**, 072303 (2005).

[52] M. Nowakowski, E. A. Paschos, and J. M. Rodriguez, Eur. J. Phys. **26**, 545 (2005).

[53] http://pdg.lbl.gov/.

[54] W. C. Haxton and E. M. Henley, *Symmetries and fundamental interactions in nuclei* (World Scientific, Singapore, 1995).

[55] T. De Forest, Nucl. Phys. **A392**, 232 (1983).

[56] H. W. L. Naus and J. H. Koch, Phys. Rev. **C36**, 2459 (1987).

[57] P. J. Mohr and B. N. Taylor, Rev. Mod. Phys. **72**, 351 (2000).

[58] S. Galster et al., Nucl. Phys. **B32**, 221 (1971).

[59] M. K. Jones et al., Phys. Rev. Lett. **84**, 1398 (2000).

[60] M. Vanderhaeghen, Few Body Syst. **41**, 103 (2007).

[61] H. Budd, A. Bodek, and J. Arrington, arXiv:0308005 [hep-ex] (2003).

[62] R. Bradford, A. Bodek, H. Budd, and J. Arrington, Nucl. Phys. Proc. Suppl. **159**, 127 (2006).

[63] A. Bodek, S. Avvakumov, R. Bradford, and H. Budd, Eur. Phys. J. **C53**, 349 (2008).

[64] J. J. Kelly, Phys. Rev. **C66**, 065203 (2002).

[65] J. J. Kelly, Phys. Rev. **C70**, 068202 (2004).

[66] H. Forkel, Phys. Rev. **C56**, 510 (1997).

[67] R. D. Mckeown, Phys. Lett. **B219**, 140 (1989).

[68] D. H. Beck, Phys. Rev. **D39**, 3248 (1989).

[69] J. Liu, R. D. McKeown, and M. J. Ramsey-Musolf, Phys. Rev. **C76**, 025202 (2007).

[70] S. F. Pate, D. W. McKee, and V. Papavassiliou, Phys. Rev. **C78**, 015207 (2008).

[71] N. Jachowicz, P. Vancraeyveld, P. Lava, C. Praet, and J. Ryckebusch, Phys. Rev. **C76**, 055501 (2007).

[72] K. A. Aniol et al. (HAPPEX), Phys. Lett. **B635**, 275 (2006).

[73] A. Acha et al. (HAPPEX), Phys. Rev. Lett. **98**, 032301 (2007).

[74] D. T. Spayde et al. (SAMPLE), Phys. Lett. **B583**, 79 (2004).

[75] F. E. Maas et al. (A4), Phys. Rev. Lett. **93**, 022002 (2004).

[76] F. E. Maas et al., Phys. Rev. Lett. **94**, 152001 (2005).

[77] D. S. Armstrong et al. (G0), Phys. Rev. Lett. **95**, 092001 (2005).

[78] T. M. Ito et al. (SAMPLE), Phys. Rev. Lett. **92**, 102003 (2004).

[79] H. Forkel, M. Nielsen, X. Jin, and T. D. Cohen, Phys. Rev. **C50**, 3108 (1994).

[80] P. Lava, Ph.D. thesis, Universiteit Gent (2005), URL `http://inwpent5.ugent.be/papers/phdpascal.pdf`.

[81] R. Jaffe, Phys. Lett. **B229**, 275 (1989).

[82] M. Ramsey-Musolf and M. Burkardt, Z Phys. C **61**, 433 (1994).

[83] H. Weigel, A. Abada, R. Alkofer, and H. Reinhardt, Phys. Lett. **B353**, 20 (1995).

[84] A. Silva, H.-C. Kim, and K. Goeke, Phys. Rev. **D65**, 014016 (2002).

[85] D. B. Leinweber et al., Phys. Rev. Lett. **94**, 212001 (2005).

[86] P. Wang, D. B. Leinweber, A. W. Thomas, and R. D. Young (2008).

[87] A. Bodek, S. Avvakumov, R. Bradford, and H. Budd, J. Phys. Conf. Ser. **110**, 082004 (2008).

[88] K. S. Kuzmin, V. V. Lyubushkin, and V. A. Naumov, Eur. Phys. J. **C54**, 517 (2008).

[89] R. Gran et al. (K2K), Phys. Rev. **D74**, 052002 (2006).

[90] S. F. Pate, Eur. Phys. J. **A24S2**, 67 (2005).

[91] A. Airapetian et al. (HERMES), Phys. Rev. Lett. **92**, 012005 (2004).

[92] A. Airapetian et al. (HERMES), Phys. Rev. **D75**, 012007 (2007).

[93] P. L. Anthony et al. (E155), Phys. Lett. **B493**, 19 (2000).

[94] B. Adeva et al. (Spin Muon (SMC)), Phys. Lett. **B412**, 414 (1997).

[95] D. Adams et al. (Spin Muon (SMC)), Phys. Rev. **D56**, 5330 (1997).

[96] B. W. Filippone and X.-D. Ji, Adv. Nucl. Phys. **26**, 1 (2001).

[97] J. R. Ellis and M. Karliner, Phys. Lett. **B341**, 397 (1995).

[98] L. A. Ahrens et al., Phys. Rev. **D35**, 785 (1987).

[99] G. T. Garvey, W. C. Louis, and D. H. White, Phys. Rev. **C48**, 761 (1993).

[100] S. F. Pate, Phys. Rev. Lett. **92**, 082002 (2004).

[101] W. M. Alberico et al., Nucl. Phys. **A651**, 277 (1999).

[102] K. Goeke, H.-C. Kim, A. Silva, and D. Urbano, Eur. Phys. J. **A32**, 393 (2007).

[103] A. Silva, H.-C. Kim, D. Urbano, and K. Goeke, Phys. Rev. **D74**, 054011 (2006).

[104] A. Silva, H.-C. Kim, D. Urbano, and K. Goeke, Phys. Rev. **D72**, 094011 (2005).

[105] J. D. Walecka, Ann. Phys. **83**, 491 (1974).

[106] B. D. Serot and J. D. Walecka, Adv. Nucl. Phys. **16**, 1 (1986).

[107] C. J. Horowitz and B. D. Serot, Nucl. Phys. **A368**, 503 (1981).

[108] S. Gardner and J. Piekarewicz, Phys. Rev. **C50**, 2822 (1994).

[109] S. Eidelman et al. (Particle Data Group), Phys. Lett. **B592**, 1 (2004).

[110] M. Anghinolfi et al., Nucl. Phys. **A602**, 405 (1996).

[111] C. Williamson et al., Phys. Rev. **C56**, 3152 (1997).

[112] A. Zghiche et al., Nucl. Phys. **A572**, 513 (1994).

[113] R. M. Sealock et al., Phys. Rev. Lett. **62**, 1350 (1989).

[114] O. Benhar, N. Farina, H. Nakamura, M. Sakuda, and R. Seki, Phys. Rev. **D72**, 053005 (2005).

[115] B. Szczerbinska, T. Sato, K. Kubodera, and T. S. H. Lee, Phys. Lett. **B649**, 132 (2007).

[116] P. Barreau et al., Nucl. Phys. **A402**, 515 (1983).

[117] P. Lava, M. C. Martinez, J. Ryckebusch, J. A. Caballero, and J. M. Udias, Phys. Lett. **B595**, 177 (2004).

[118] P. Huber, M. Mezzetto, and T. Schwetz, JHEP **03**, 021 (2008).

[119] G. P. Zeller et al. (NuTeV), Phys. Rev. Lett. **88**, 091802 (2002).

[120] J. M. Conrad, J. M. Link, and M. H. Shaevitz, Phys. Rev. **D71**, 073013 (2005).

[121] A. B. Balantekin, J. H. de Jesus, and C. Volpe, Phys. Lett. **B634**, 180 (2006).

[122] A. Czarnecki and W. J. Marciano, Phys. Rev. **D53**, 1066 (1996).

[123] J. Erler and M. J. Ramsey-Musolf, Phys. Rev. **D72**, 073003 (2005).

[124] K. Abe et al. (SLD), Phys. Rev. Lett. **86**, 1162 (2001).

[125] G. Abbiendi et al. (OPAL), Phys. Lett. **B546**, 29 (2002).

[126] A. Derevianko, Phys. Rev. Lett. **85**, 1618 (2000).

[127] P. L. Anthony et al. (SLAC E158), Phys. Rev. Lett. **95**, 081601 (2005).

[128] G. P. Zeller et al. (NuTeV), Phys. Rev. **D65**, 111103 (2002).

[129] K. P. O. Diener, S. Dittmaier, and W. Hollik, Phys. Rev. **D69**, 073005 (2004).

[130] S. A. Kulagin, Phys. Rev. **D67**, 091301 (2003).

[131] K. J. Eskola and H. Paukkunen, JHEP **06**, 008 (2006).

[132] S. Davidson, S. Forte, P. Gambino, N. Rius, and A. Strumia, JHEP **02**, 037 (2002).

[133] A. Kurylov, M. J. Ramsey-Musolf, and S. Su, Nucl. Phys. **B667**, 321 (2003).

[134] R. N. Mohapatra et al., Rept. Prog. Phys. **70**, 1757 (2007).

[135] E. A. Paschos and L. Wolfenstein, Phys. Rev. **D7**, 91 (1973).

[136] G. P. Zeller, Ph.D. thesis, Northwestern University (2002).

[137] C. Praet, N. Jachowicz, P. Lava, J. Ryckebusch, and K. Vantournhout, Phys. Rev. **C74**, 065501 (2006).

[138] T. W. Donnelly et al., Nucl. Phys. **A541**, 525 (1992).

[139] J. G. Morfin, Nucl. Phys. Proc. Suppl. **149**, 233 (2005).

[140] S. Boyd (MINERvA), Nucl. Phys. Proc. Suppl. **139**, 311 (2005).

[141] W. M. Alberico et al., Phys. Lett. **B438**, 9 (1998).

[142] D. S. Armstrong et al. (Qweak), AIP Conf. Proc. **698**, 172 (2004).

[143] http://www-finesse.fnal.gov/.

[144] P. Lava, N. Jachowicz, M. C. Martinez, and J. Ryckebusch, Phys. Rev. **C73**, 064605 (2006).

[145] G. Garvey, E. Kolbe, K. Langanke, and S. Krewald, Phys. Rev. **C48**, 1919 (1993).

[146] B. Van Der Ventel and J. Piekarewicz, Phys. Rev. **C73**, 025501 (2006).

[147] A. Meucci, C. Giusti, and F. D. Pacati, Nucl. Phys. **A773**, 250 (2006).

[148] K. S. Kim, M.-K. Cheoun, and B. G. Yu, Phys. Rev. **C77**, 054604 (2008).

[149] T. Leitner, L. Alvarez-Ruso, and U. Mosel, Phys. Rev. **C74**, 065502 (2006).

[150] T. Sato, D. Uno, and T. S. H. Lee, Phys. Rev. **C67**, 065201 (2003).

[151] E. Hernandez, J. Nieves, and M. Valverde, Phys. Rev. **D76**, 033005 (2007).

[152] T. Leitner, O. Buss, L. Alvarez-Ruso, and U. Mosel, arXiv:0812.0587 [nucl-th] (2008).

[153] C. H. Llewellyn Smith, Phys. Rept. **3**, 261 (1972).

[154] P. A. Schreiner and F. Von Hippel, Phys. Rev. Lett. **30**, 339 (1973).

[155] P. Stoler, Phys. Rept. **226**, 103 (1993).

[156] A. J. Dufner and Y.-S. Tsai, Phys. Rev. **168**, 1801 (1968).

[157] E. A. Paschos, J.-Y. Yu, and M. Sakuda, Phys. Rev. **D69**, 014013 (2004).

[158] O. Lalakulich and E. A. Paschos, Phys. Rev. **D71**, 074003 (2005).

[159] T. Kitagaki et al., Phys. Rev. **D34**, 2554 (1986).

[160] O. Lalakulich, E. A. Paschos, and G. Piranishvili, Phys. Rev. **D74**, 014009 (2006).

[161] C. Alexandrou, G. Koutsou, T. Leontiou, J. W. Negele, and A. Tsapalis, Phys. Rev. **D76**, 094511 (2007).

[162] D. Barquilla-Cano, A. J. Buchmann, and E. Hernandez, Phys. Rev. **C75**, 065203 (2007).

[163] S. L. Adler, Ann. Phys. **50**, 189 (1968).

[164] K. S. Kuzmin, V. V. Lyubushkin, and V. A. Naumov, Acta Phys. Polon. **B37**, 2337 (2006).

[165] G. M. Radecky et al., Phys. Rev. **D25**, 1161 (1982).

[166] C. Alexandrou, T. Leontiou, J. W. Negele, and A. Tsapalis, Phys. Rev. Lett. **98**, 052003 (2007).

[167] L. S. Geng, J. M. Camalich, L. Alvarez-Ruso, and M. J. Vicente Vacas, Phys. Rev. **D78**, 014011 (2008).

[168] L. S. Geng, J. Martin Camalich, L. Alvarez-Ruso, and M. J. Vicente Vacas, Mod. Phys. Lett. **A23**, 2246 (2008).

[169] M. Procura, arXiv:0803.4291 [hep-ph] (2008).

[170] W. Rarita and J. S. Schwinger, Phys. Rev. **60**, 61 (1941).

[171] J. Weda, Ph.D. thesis, Universiteit Groningen (1999).

[172] V. Pascalutsa and R. Timmermans, Phys. Rev. **C60**, 042201 (1999).

[173] S. J. Barish et al., Phys. Rev. **D16**, 3103 (1977).

[174] F. X. Lee, L. E. Wright, and C. Bennhold, Phys. Rev. **C55**, 318 (1997).

[175] C. Praet, O. Lalakulich, N. Jachowicz, and J. Ryckebusch, arXiv:0804.2750 [nucl-th] and Phys. Rev. C, in press (2009).

[176] J. Nieves, E. Oset, and C. Garcia-Recio, Nucl. Phys. **A554**, 554 (1993).

[177] C. Garcia-Recio, E. Oset, L. L. Salcedo, D. Strottman, and M. J. Lopez, Nucl. Phys. **A526**, 685 (1991).

[178] I. J. D. MacGregor, T. T.-H. Yau, J. Ahrens, J. R. M. Annand, R. Beck, D. Branford, P. Grabmayr, S. J. Hall, P. D. Harty, T. Hehl, et al., Phys. Rev. Lett. **80**, 245 (1998).

[179] E. A. Paschos, I. Schienbein, and J. Y. Yu, arXiv:0704.1991 [hep-ph] (2007).

[180] S. L. Adler, S. Nussinov, and E. A. Paschos, Phys. Rev. **D9**, 2125 (1974).

[181] M. J. Vicente Vacas, M. K. Khankhasaev, and S. G. Mashnik, nucl-th/9412023 (1994).

[182] W. Cosyn, M. C. Martínez, and J. Ryckebusch, Phys. Rev. **C77**, 034602 (2008).

[183] K. L. G. Heyde, *The nuclear shell model* (Springer-Verlag, Berlin, 1994).

[184] O. Lalakulich, N. Jachowicz, C. Praet, and J. Ryckebusch, Phys. Rev. **C79**, 015206 (2009).

[185] S. K. Singh, M. J. Vicente-Vacas, and E. Oset, Phys. Lett. **B416**, 23 (1998).

[186] M. S. Athar, S. Ahmad, and S. K. Singh, Phys. Rev. **D75**, 093003 (2007).

[187] O. Benhar, D. Day, and I. Sick, nucl-ex/0603032 (2006).

[188] M. Hasegawa et al. (K2K), Phys. Rev. Lett. **95**, 252301 (2005).

[189] K. Hiraide et al. (SciBooNE), Phys. Rev. **D78**, 112004 (2008).

[190] A. A. Aguilar-Arevalo et al. (MiniBooNE), Phys. Lett. **B664**, 41 (2008).

[191] E. A. Paschos, A. Kartavtsev, and G. J. Gounaris, Phys. Rev. **D74**, 054007 (2006).

[192] C. Berger and L. M. Sehgal, arXiv:0812.2653 [hep-ph] (2008).

[193] S. K. Singh, M. Sajjad Athar, and S. Ahmad, Phys. Rev. Lett. **96**, 241801 (2006).

[194] L. Alvarez-Ruso, L. S. Geng, S. Hirenzaki, and M. J. Vicente Vacas, Phys. Rev. **C75**, 055501 (2007).

[195] J. E. Amaro, E. Hernandez, J. Nieves, and M. Valverde, Phys. Rev. **D79**, 013002 (2009).

[196] T. Leitner, U. Mosel, and S. Winkelmann, arXiv:0901.2837 [nucl-th] (2009).

[197] R. C. Carrasco, J. Nieves, and E. Oset, Nucl. Phys. **A565**, 797 (1993).

[198] D. Drechsel, L. Tiator, S. S. Kamalov, and S. N. Yang, Nucl. Phys. **A660**, 423 (1999).

[199] W. Peters, Ph.D. thesis, Giessen University (1998).

[200] L. Tiator, A. K. Rej, and D. Drechsel, Nucl. Phys. **A333**, 343 (1980).

[201] L. Tiator and L. E. Wright, Phys. Rev. **C30**, 989 (1984).

[202] W. M. Macdonald, E. T. Dressler, and J. S. O'Connell, Phys. Rev. **C19**, 455 (1979).

[203] W. Peters, H. Lenske, and U. Mosel, Nucl. Phys. **A640**, 89 (1998).

[204] S. Janssen, J. Ryckebusch, W. Van Nespen, and D. Debruyne, Nucl. Phys. **A672**, 285 (2000).

Samenvatting

Inleiding

In de zoektocht naar een allesbehelzende natuurkundige theorie vormt het *standaardmodel der elementaire deeltjes* het meest recente orgelpunt. Als overkoepelende beschrijving van de sterke en elektrozwakke wisselwerking is het standaardmodel uiterst succesvol, in die zin dat alle experimentele resultaten tot nu toe steeds een interpretatie hebben gekregen binnen dit raamwerk. Echter, ook het standaardmodel is volgens velen niet het eindpunt van ons streven naar een verdere unificatie in de beschrijving van fysische processen. Om deze bewering kracht bij te zetten, verwijst men vaak naar het ontbreken van voorspellingen voor de waarden van verschillende parameters. Zo voorzag het standaardmodel oorspronkelijk enkel in het bestaan van neutrino's als massaloze, linkshandige deeltjes. De ontdekking van neutrino-oscillaties toont overduidelijk aan dat dit beeld niet klopt, aangezien neutrino's enkel van smaaktoestand kunnen veranderen wanneer ze een massa hebben. Er dringt zich bijgevolg een uitbreiding van het standaardmodel op, waarin de zwakke eigentoestanden $|\nu_e\rangle$, $|\nu_\mu\rangle$ en $|\nu_\tau\rangle$ beschreven worden als kwantummechanische superposities van de massa-eigentoestanden $|\nu_1\rangle$, $|\nu_2\rangle$ en $|\nu_3\rangle$. Net als in de quarksector ontstaat er een opmengingsmatrix die een verband legt tussen de zwakke- en massa-eigentoestanden van de neutrino's. Experimenten die neutrino-oscillaties onderzoeken, stellen zich dan tot doel om deze matrix zo nauwkeurig mogelijk te bepalen.

Neutrino-experimenten

Lopende en geplande generaties van neutrino-experimenten creëren ongeziene opportuniteiten voor het onderzoek in zwakke hadronen- en kernfysica. Neutrino's interageren namelijk enkel via de zwakke interactie. Bovendien schenden ze pariteit op maximale wijze, hetgeen aanleiding geeft tot de karakteristieke V−A structuur van de zwakke lepton- en quarkstromen. Experimenten met neutrino's lenen zich dus perfect tot een studie van de axiale sector in zwakke interacties.
Uiteraard verlopen deze experimenten niet aan vrije quarks. Quarks zitten opgesloten ("confined") in nucleonen, welke dan weer gebonden zijn in de atoomkernen die het trefmateriaal uitmaken van neutrinodetectoren. Aangezien neutrino-interacties

zich slechts zeer sporadisch voordoen, maken experimenten vaak gebruik van enorme hoeveelheden trefmateriaal, in de vorm van meterslange stalen platen of vaten gevuld met een kiloton baby-olie.
Een belangrijke categorie van neutrino-experimenten, "long-baseline" experimenten genaamd, onderzoekt smaakoscillaties door te kijken naar ν_μ-interacties in een detector dichtbij de bron en in een detector verder weg, op een afstand L van de eerste detector. Opdat een dergelijke opstelling gevoelig zou zijn aan neutrino-oscillaties, moet voldaan zijn aan $L[\mathrm{km}]/E_\nu[\mathrm{GeV}] \gtrsim 1/\Delta m^2[\mathrm{eV}^2]$, waarbij $\Delta m^2 \sim 3 \times 10^{-3}\mathrm{eV}^2$. Voor een typische afstand van $L \sim 100$ km betekent dit concreet dat de versnellers in deze faciliteiten muon-neutrino's met een energie van ongeveer 1 GeV moeten leveren.
Samenvattend leert dit ons dat een goed begrip van neutrino-atoomkern interacties bij 1-GeV energieën een wezenlijk onderdeel zal vormen in de analyse van long-baseline experimenten. Vooral in de zogenaamde "Superbeam" experimenten, waar hoge-intensiteitsbundels statistische fluctuaties ondergeschikt maken aan systematische onzekerheden, wordt een realistische beschrijving van alle relevante processen in dit energiegebied noodzakelijk om, onder meer, achtergronden te berekenen, verschillende soorten reacties te onderscheiden en de neutrino-energie te reconstrueren. Naast experimenten die zich concentreren op een bepaling van de oscillatie-parameters, zijn er ook waarvoor een verbeterde kennis van neutrino-atoomkern werkzame doorsnedes een doel op zich is. Met name de SciBooNE en MINERνA collaboraties plannen een doorgedreven studie van neutrino-interacties met atoomkernen. Het SciBooNE experiment gebruikt hierbij een 1-GeV neutrinobundel voor de studie van neutrino- en antineutrino-koolstof interacties. MINERνA beoogt een veel breder energie-interval te onderzoeken, tot neutrino-energieën van een paar tientallen GeV. Echter, ook zij zullen de nodige aandacht besteden aan o.a. de rol van kerneffecten in neutrino-interacties van enkele GeV aan atoomkernen gaande van helium tot lood.

Neutrino-atoomkern interacties by intermediaire energieën

Het nucleair excitatiespectrum voor niet al te hoge waarden van het gekwadrateerde impuls-viermomentum, $Q^2 < 1$ GeV^2, en energietransfers ω kleiner dan 1 GeV, wordt gedomineerd door twee brede pieken. De eerste piek ligt voorbij de drempelenergie voor nucleon-emissie, rond de waarde $\omega \sim |\vec{q}|^2/2M$, met $\vec{q}$ de impulstransfer en M de nucleonmassa. In dit gebied is het overgrote deel van de sterkte te wijten aan quasi-elastische (QE) nucleon-uitstoot reacties. Zowat 300 MeV verderop ligt de tweede piek, waar de extra energietransfer het mogelijk maakt om een nucleon tot een Δ te exciteren. Om die reden wordt de tweede bult meestal de Δ piek genoemd. Tussen beide structuren in ligt een dalgebied, waarnaar in de literatuur verwezen wordt als de "dip". In deze thesis spitsen we onze aandacht toe op het QE- en het Δ-gebied. We ontwikkelen meer bepaald een theoretisch raamwerk voor de berekening

van neutrino-atoomkern werkzame doorsnedes die de dominante processen in beide gebieden beschrijven.

Theoretisch raamwerk

Kenmerkend voor de reacties in het QE- en Δ-gebied is dat ze hoofdzakelijk bepaald worden door eendeeltjes-mechanismen. Anders gezegd, het leeuwendeel van hun sterkte daar is afkomstig van processen waarbij één enkel gebonden nucleon het totale viermomentum q^μ van het zwakke ijkboson absorbeert. Een benadering die onder deze omstandigheden vaak wordt aangewend, is de zogenaamde impulsbenadering (IA) ("impulse approximation"). De IA bestaat er namelijk uit dat de veeldeeltjes-operator tussen de initiële en finale toestand van het A-nucleonen systeem vervangen wordt door een som van eendeeltjes-operatoren. Van de aldus bekomen hadronstromen wordt verondersteld dat ze vrij zijn van medium-effecten, en dus dezelfde structuur hebben als de overeenkomstige vrije ("on-shell") koppelingen. Op die manier valt het modelleren van neutrino-atoomkern interacties uiteen in twee hoofdproblemen:

- Hoe kan het zwak eendeeltjes-proces beschreven worden?
- Hoe brengt men kerneffecten in rekening?

Fenomenologische aanpak met vormfactoren

Bij energietransfers $\omega \leq 1$ GeV vormt een beschrijving van het vrije eendeeltjes-proces aan de hand van hadronische vrijheidsgraden het meest natuurlijke uitgangspunt. In een laagste-orde behandeling is het invariant matrixelement voor een semileptonisch, zwak proces dan evenredig met de contractie van de lepton- en de hadronstroom, $M_{fi} \sim l_\alpha h^\alpha$. Hoewel met de V$-$A natuur van de zwakke interactie de structuur van de leptonstroom volledig bepaald is, neemt de hadronstroom in het algemeen een meer complexe vorm aan. De verklaring hiervoor ligt in de eindige dimensie van de betrokken hadronen, waardoor zij niet eenvoudigweg als puntdeeltjes kunnen beschouwd worden. Om deze hadronkoppelingen dan wel te bepalen, kan men een beroep doen op ab initio berekeningen uitgevoerd in een of ander quarkmodel. Als alternatief hiervoor wordt echter vaak gekozen voor een meer fenomenologische aanpak door een set van vector en axiale vormfactoren in te voeren. De vormfactoren spelen dan als het ware de rol van lopende ("running") koppelingsconstanten, die variëren al naargelang de resolutie waarmee de bewuste hadronen worden *bekeken*. Op die manier worden vormfactoren vaak geparametriseerd als dipoolfuncties van Q^2, welke nader bepaald kunnen worden met behulp van theoretische wetten en experimentele gegevens. De zwakke vector vormfactoren, bijvoorbeeld, kunnen via de CVC-hypothese

aan de goed gekende elektromagnetische vormfactoren gerelateerd worden. Aangezien de informatie over axiale vormfactoren enkel van neutrino-experimenten kan komen, is onze kennis van die sector nog steeds heel beperkt. Een nauwkeurige meting van de axiale vormfactoren is dan ook een hoofddoel van experimenten als SciBooNE en MINERνA. Hiertoe is het echter noodzakelijk om een goed beeld te hebben van de manier waarop kerneffecten de gewenste informatie kunnen beïnvloeden.

Kerneffecten

Bij neutrino-atoomkern verstrooiing interageert het inkomend neutrino niet langer met een vrij nucleon, maar met een gebonden nucleon dat rondbeweegt in de trefkern. Om de effecten van Fermi-beweging, het uitsluitingsprincipe van Pauli en nucleaire binding in rekening te brengen, beroept men zich traditioneel op een relativistisch Fermi-gas (RFG) model. In zo'n RFG model wordt de atoomkern opgevat als een collectie nucleonen, welke de Fermi-zee opvullen tot aan het Fermi-niveau k_F. De energie van een nucleon is dan gegeven door $E = (k^2 + M^2)^{1/2} - E_b$, met $k < k_F$ en E_b een bindingsenergie. Naast dit relatief eenvoudige model bestaan er echter ook meer realistische beschrijvingen van de kernstructuur, zoals een gemiddeld-veld model of een benadering met spectraalfuncties. In deze thesis beschrijven we de schillenstructuur van de atoomkern aan de hand van een gemiddeld-veld model: de nucleonen in de kern bewegen onafhankelijk in een gemiddeld-veld potentiaal ontstaan door de interacties met de omringende nucleonen. De golffuncties van de initiële en finale A-nucleonen toestand ontstaan hierbij als een volledig geantisymmetriseerde vorm van het product van de relativistische gebonden-toestand eendeeltjesgolffuncties. Deze laatste bepalen we uit een Hartreebenadering van het σ-ω model ontwikkeld door Walecka. In tegenstelling tot een spectraalfunctie-benadering, waar in rekening wordt gebracht dat korte-dracht nucleon-nucleon correlaties een deel van de gemiddeld-veld sterkte verplaatsen naar een hoger $(E_m, \vec{p}_m)$ gebied, nemen wij aan dat de eendeeltjesorbitalen volledig bezet zijn. Zoals hierboven reeds gesteld, met de invoering van de IA, beschouwen we geen processen waarbij meerdere nucleonen in de trefkern betrokken zijn. Uiteraard wordt deze benadering minder accuraat wanneer de trefkern met een lagere ruimtelijke resolutie, m.a.w. bij kleine Q^2, *gescand* wordt. Op dat moment kunnen multi-nucleon mechanismen een rol beginnen spelen, en moeten lange-dracht correlaties in rekening gebracht worden met behulp van "(continuum) random-phase approximation" ((C)RPA) berekeningen.
Naast de beschrijving van de kernstructuur vormt de behandeling van finale toestandsinteracties (FSI) een essentieel ingrediënt in elke studie van neutrino-atoomkern interacties. Eens geproduceerd in de primaire zwakke interactie, zullen de hadronen met de achterblijvende nucleonen in de trefkern interageren op hun weg naar buiten. In het geval van Δ-productie kan men stellen dat het effect tweeledig is. Ten eerste zullen de massa en de vervalbreedte van de Δ in een nucleair medium verschillen van

hun vrije waarden. Verder, nadat de Δ is vervallen, zullen de vervalproducten (meestal een pion en een nucleon, soms enkel een nucleon) onderhevig zijn aan FSI effecten. Mediummodificaties van Δ eigenschappen werden reeds onderzocht binnen het raamwerk van een microscopisch Δ-gat model. Uit de berekening van de Δ zelfenergie in het nucleair medium leidt men een verschuiving van de resonantiepositie en een vergroting van de vervalbreedte af. Voor onze toepassingen gebruiken we de eenvoudige substitutie: $M_\Delta \rightarrow M_\Delta + 30$ MeV en $\Gamma \rightarrow \Gamma + 40$ MeV, omdat het een succesvol recept is gebleken in studies van foto-geïnduceerde twee-nucleon-uitstoot reacties.
De manier waarop FSI effecten in rekening gebracht worden, hangt sterk samen met het type reactie onder beschouwing. In deze thesis bestuderen we reacties in het *quasi-vrije* regime, gekenmerkt door de *directe* uitstoot van pionen en/of nucleonen waarbij de restkern achterblijft met een excitatie-energie van maximaal enkele tientallen MeV. Onder die omstandigheden wordt de nucleaire attenuatie van het ejectiel berekend in de relativistische verstoorde-golf impulsbenadering (RDWIA) met behulp van pion/nucleon-kern optische potentialen, of in Glaubermodellen, welke veeldeeltjesveralgemeningen zijn van de eikonale benadering. Voor de berekening van directe-uitstoot werkzame doorsnedes, bogen we hier op een relativistische uitbreiding van de Glauber veelvuldige-verstrooiingstheorie (RMSGA), zoals ontwikkeld binnen onze onderzoeksgroep. In het kinematisch gebied waar de eendeeltjessterkte overheerst, $|\vec{p}_m| \leq 300$ MeV en $E_m \leq 80$ MeV, leiden de RMSGA voorspellingen namelijk tot een behoorlijke beschrijving van nucleon-uitstoot data in exclusieve en semi-exclusieve electron-verstrooiingsprocessen.
Een andere, meer *inclusieve* aanpak van uitstootreacties bestaat eruit om de eis van quasi-vrije verstrooiing te laten varen en alle mogelijke nucleaire configuraties in de eindtoestand in beschouwing te nemen. In dit geval grijpt men vaak naar Monte-Carlo methodes of semi-klassieke transportmodellen om pionen en nucleonen door de kern te *propageren*. Alhoewel een kwantummechanische beschrijving van het probleem dan niet meer mogelijk is, bieden deze technieken het voordeel dat ook inelasticiteiten en gekoppelde-kanaaleffecten in rekening kunnen gebracht worden. Inderdaad, terwijl Glaubermodellen enkel een verlies van flux voorspellen met betrekking tot de *elastische* uitstootsterkte, zijn transportmodellen in staat om aan te duiden in welke inelastische kanalen die sterkte precies verdwenen is.

Resultaten

Quasi-elastische nucleon-uitstoot reacties

Als eerste test voor ons model starten we in hoofdstuk 2 de studie van QE werkzame doorsnedes met een vergelijking tussen berekeningen in de vlakke-golflimiet (RPWIA) en inclusieve $A(e,e')$ data. Om de numerieke berekeningen te verlichten, voeren we het begrip van *gebonden-toestand propagator* in. Dankzij deze analytische

vereenvoudiging is het mogelijk om een gesloten gedaante op te stellen voor de RPWIA werkzame doorsnedes in de momentumruimte.
We vinden dat, voor gematigde Q^2 waarden, zowel de RPWIA als de RFG berekeningen een goede beschrijving geven van het gebied rond de QE piek. Beide modellen vertonen de neiging om de piekwaarden licht te overschatten. De RPWIA voorspellingen geven dan weer een betere beschrijving van de staarten in de ω-distributie dan die van het RFG model. Naar $Q^2 = 0.1$ GeV^2 toe, stellen we vast dat ons model het steeds slechter doet. Het is de IA zelf die bij dergelijk lage Q^2, en dus bij een kleinere ruimtelijke resolutie, geen realistisch uitgangspunt meer vormt. Processen waarin meerdere nucleonen betrokken zijn, beginnen een belangrijke rol te spelen, zodat een benadering met RPA correlaties daar noodzakelijk wordt.
Kijken we naar neutrino-atoomkern interacties, dan zien we dat de huidige onzekerheden op de axiale massa M_A, welke van de orde van 20% zijn, aanleiding geven tot even grote fluctuaties in de werkzame doorsnedes. Met betrekking tot FSI mechanismen tonen we aan dat een herschaling van RPWIA berekeningen met een factor ontleend aan de experimenteel bepaalde $A(e,e'p)$ transparantie nagenoeg hetzelfde resultaat oplevert als de ongefactoriseerde RMSGA berekeningen. Aangezien het RMSGA model met aanzienlijk succes getest werd tegen $A(e,e'p)$ data, besluiten we hieruit dat RMSGA predicties een realistisch beeld geven van de elastische nucleonuitstoot bijdrage tot de inclusieve νA werkzame doorsnede. Met andere woorden, een nauwkeurige meting van dit kanaal bij de kinematische *cuts* $|\vec{p}_m| \leq 300$ MeV and $E_m \leq 80$ MeV zou kunnen leiden tot nieuwe informatie over M_A.
Als toepassing op QE νA verstrooiing bestuderen we de mogelijkheid voor een meting van de Weinberghoek bij lage Q^2 door middel van de Paschos-Wolfenstein relatie. We tonen aan dat de theoretische onzekerheden op deze super-ratio van $\nu(\overline{\nu})A$ werkzame doorsnedes zeer goed onder controle zijn. Echter, een meting van de asymmetrie A_{PV} in pariteitsschendende electron-verstrooiingsexperimenten laat een bepaling van $\sin^2\theta_W$ toe die tot 10 keer zo nauwkeurig is als bij een meting van de Paschos-Wolfenstein relatie met dezelfde precisie. Indien we enkel het proton-uitstoot deel van de Paschos-Wolfenstein relatie beschouwen, dan blijkt hieruit een sterke g_A^s afhankelijkheid. Op voorwaarde dat de vectoriële vreemdheidsparameters voldoende goed gekend zijn, is deze relatie dan ook bijzonder aantrekkelijk om nieuwe informatie over de bijdrage van vreemde quarks tot de nucleonspin te onttrekken. Tot slot bekijken we de vreemdheidsgevoeligheid van verscheidene QE $\nu(\overline{\nu})A$ ratios op een meer systematische manier. Wegens de milde afhankelijkheid van de parameters μ_s and r_s^2 besluiten we dat de verhouding $R^{\overline{\nu}}_{p/n}$ een van de meer geschikte kandidaten is voor de bepaling van g_A^s.

Pionproductie na Δ-excitatie

In hoofdstuk 3 nemen we het proces van neutrino-geïnduceerde pionproductie onder de loep. Hierbij wordt aangenomen dat elk geproduceerd pion afkomstig is van een Δ, geëxciteerd aan een nucleon. Na een gedetailleerde studie van de relevante zwakke en sterke Δ-koppelingen focussen we eerst op het elementaire proces: verstrooiing aan een vrij nucleon. We stellen vast dat de huidige, grote onzekerheden op neutrinodata aanleiding geven tot onzekerheden van de orde van 30% op zowel de axiale vormfactor $C_5^A(Q^2)$ als de overeenkomstige $N(\nu, l\pi)$ predicties. Ambiguïteiten in de $\Delta\pi N$ koppelingen, gerelateerd aan ongewilde spin-1/2 delen van de Δ propagator, hebben daarentegen maar een klein effect op observabelen.
Voor de reactie met kernen berekenen we werkzame doorsnedes voor *primaire* pionproductie, vooraleer het pion de kern verlaat. Er wordt een vergelijking gemaakt met inclusieve electrondata en berekeningen afkomstig van andere theoretische modellen. Mits de regels $M_\Delta \rightarrow M_\Delta + 30$ MeV, $\Gamma \rightarrow \Gamma + 40$ MeV voor mediummodificaties van de massa en vervalbreedte van de Δ vinden we dat onze RPWIA berekeningen een goede schatting van de 1-π sterkte in het Δ gebied geven. Onder quasi-vrije omstandigheden, waarbij het geproduceerde en gedetecteerde pion een en hetzelfde deeltje zijn, is het effect van FSI mechanismen bijzonder groot. Voor een ijzerkern, bijvoorbeeld, komt slechts 25% van de pionen onverstoord uit de trefkern.
Tot slot bestuderen we de neutrino-geïnduceerde coherente productie van pionen aan kernen. Aangezien de trefkern intact blijft, wordt dit proces gedomineerd door kleine momentumtransfers en voorwaartse verstrooiingshoeken. Bovendien is de sterkte van de overeenkomstige werkzame doorsnedes bijna uitsluitend te wijten aan de axiale vormfactoren, zodat deze reactie bijzonder gevoelig is aan de waarde $C_5^A(0)$. De invloed van kerneffecten wordt onderzocht aan de hand van RMSGA berekeningen in de *lokale* benadering, welke erop neerkomt dat een constante waarde voor $\vec{p}_m$ wordt gekozen bij de evaluatie van de transitie-operator $\hat{\mathcal{O}}^\mu$. We vinden dat Δ-mediummodificaties en FSI de werkzame doorsnedes voor $\nu + A \longrightarrow l + A + \pi$ decimeren. Interessant om vast te stellen is dat, net als bij incoherente pionproductie, ons eenvoudig schema voor Δ-mediummodificaties tot resultaten leidt die zeer vergelijkbaar zijn met meer ingewikkelde benaderingen in de literatuur. Er blijken ook belangrijke verschillen te bestaan tussen de pion-momentum distributies verkregen met de lokale benadering en deze waarbij $\langle\hat{\mathcal{O}}^\mu\rangle$ op de gepaste wijze werd geïntegreerd over $\vec{p}_m$. Hoewel de lokale benadering tot accurate resultaten leidt in coherente fotoproductie processen, heeft ze bij neutrino reacties de neiging om de werkelijke sterkte te overschatten. We besluiten bijgevolg dat het gebruik van de lokale benadering in coherente pionproductie aan kernen door neutrino's niet gerechtvaardigd is.

Vooruitblik

Omwille van de strikte cuts $E_m \leq 80$ MeV en $|\vec{p}_m| \leq 300$ MeV is het voor de huidige generatie van neutrino-experimenten allerminst vanzelfsprekend om quasi-vrije neutrino-atoomkern interacties te isoleren. In het algemeen zal het finale nucleaire systeem ongedetecteerd blijven, zodat een meer inclusieve aanpak van nucleonuitstoot en pionproductie noodzakelijk wordt. Een bijzonder interessante uitbreiding van het huidige formalisme bestaat er dan ook uit om de processen corresponderend met grotere E_m te gaan beschrijven.
In de eerste plaats denken we hierbij aan tweedeeltjesmechanismen. Zo weet men uit electron-verstrooiingsstudies dat een rechtstreekse berekening van tweedeeltjesmesonuitwisselingsstromen ten dele de sterkte in de dip verklaart. Een meer praktische manier om tweedeeltjesbijdragen te onderzoeken bestaat eruit om de gebondentoestand propagator, met volledig bezette eendeeltjesorbitalen, te vervangen door een spectraalfunctie $S(E_m, \vec{p}_m)$ die een deel (typisch $\sim 20\%$) van de gemiddeld-veldsterkte herschikt naar bijdragen van korte-dracht nucleon-nucleon correlaties.
Voor de beschrijving van processen waarbij de trefkern opbreekt in verschillende stukken, en meerdere pionen en/of nucleonen uitgestuurd worden, moeten we onze toevlucht nemen tot Monte-Carlo-simulaties of transportmodeltechnieken. De RPWIA resultaten in dit werk zouden hierbij als input kunnen aangewend worden, vooraleer de geproduceerde hadronen uit de trefkern gepropageerd worden.
Binnen het gepresenteerde raamwerk voor quasi-vrije neutrino-reacties zijn ook nog enkele uitbreidingen mogelijk. Naast het dominante Δ-kanaal kan bijvoorbeeld een studie van niet-resonante *achtergrond*contributies tot de 1-π-sterkte aangevat worden. We kunnen het formalisme eveneens toepassen op de resonanties in het tweede resonantiegebied, namelijk de $P_{11}(1440)$, $D_{13}(1520)$ en $S_{11}(1535)$. Voorbij dit gebied, echter, loopt het aantal onbekende axiale $N - N^*$ koppelingen drastisch op, zodat een beschrijving van de inclusieve νA werkzame doorsnedes daar beter steunt op quark-hadron-dualiteitsstudies of Regge-gebaseerde modellen.